1 **Human Skeletal Muscle Fiber Heterogeneity Beyond Myosin Heavy Chains**

2

3 Roger Moreno-Justicia[1]*, Thibaux Van der Stede[2,3]*, Ben Stocks[1,4]*, Jenni Laitila[5], Robert A
4 Seaborne[5,6], Alexia Van de Loock[2], Eline Lievens[2], Diana Samodova[1], Leyre Marín-Arraiza[7],
5 Oksana Dmytriyeva[1], Robin Browaeys[8,9], Kim Van Vossel[2], Lukas Moesgaard[3], Nurten Yigit[10],
6 Jasper Anckaert[10], Anneleen Weyns[2], Ruud Van Thienen[2], Ronni E Sahl[5], Edmar Zanoteli[11],
7 Michael W Lawlor[12,13], Michael Wierer[14], Pieter Mestdagh[10], Jo Vandesompele[10], Julien
8 Ochala[5], Morten Hostrup[3], Wim Derave[2#], & Atul S Deshmukh[1#]

9 *Joint first-authors

10 [#]Co-corresponding authors (Atul S Deshmukh: atul.deshmukh@sund.ku.dk; Wim Derave:
11 wim.derave@ugent.be)

12

13 [1]Novo Nordisk Foundation Center for Basic Metabolic Research, Faculty of Health and Medical
14 Sciences, University of Copenhagen, Copenhagen, Denmark

15 [2]Department of Movement and Sports Sciences, Faculty of Medicine and Health Sciences,
16 Ghent University, Ghent, Belgium

17 [3]The August Krogh Section for Human Physiology, Department of Nutrition, Exercise and
18 Sports, University of Copenhagen, Copenhagen, Denmark

19 [4]Department of Molecular Medicine and Surgery, Integrative Physiology, Karolinska
20 Institutet, Stockholm, Sweden

21 [5]Department of Biomedical Sciences, Faculty of Health and Medical Sciences, University of
22 Copenhagen, Copenhagen, Denmark

[6]Centre for Human and Applied Physiological Sciences, King's College London, London, United Kingdom (present address)

[7]Novo Nordisk Foundation Center for Protein Research, Faculty of Health and Medical Sciences, University of Copenhagen, Copenhagen, Denmark

[8]Bioinformatics Expertise Unit, VIB Center for Inflammation Research, Ghent, Belgium

[9]Department of Applied Mathematics, Computer Science and Statistics, Ghent University, Ghent, Belgium

[10]Department of Biomolecular Medicine, Faculty of Medicine and Health Sciences, Ghent University, Ghent, Belgium

[11]Department of Neurology, Faculdade de Medicina (FMUSP), Universidade de São Paulo, São Paulo, Brazil

[12]Department of Pathology, Medical College of Wisconsin, Milwaukee, WI, USA

[13]Diverge Translational Science Laboratory, Milwaukee, WI, USA

[14]Proteomics Research Infrastructure, Faculty of Health and Medical Sciences, University of Copenhagen, Copenhagen, Denmark

Abstract

Skeletal muscle is an inherently heterogenous tissue comprised primarily of myofibers, which are historically classified into three distinct fiber types in humans: one “slow” (type 1) and two “fast” (type 2A and type 2X), delineated by the expression of myosin heavy chain isoforms (MYHs). However, heterogeneity between and within traditional fiber types remains underexplored. Indeed, whether MYHs are the main classifiers of skeletal muscle fibers has not been examined in an unbiased manner. Through the development and application of novel transcriptomic and proteomic workflows, applied to 1050 and 1038 single muscle fibers from human *vastus lateralis*, respectively, we show that MYHs are not the only principal drivers of skeletal muscle fiber heterogeneity. Instead, metabolic, ribosomal, and cell junction proteins are a source of multi-dimensional variation between skeletal muscle fibers. Furthermore, whilst slow and fast fiber clusters can be identified, described by their contractile and metabolic profiles, our data suggests that type 2X fibers are not phenotypically distinct to other fast fibers at an omics level. Moreover, MYH-based classifications do not adequately describe the phenotype of skeletal muscle fibers in one of the most common genetic muscle diseases, nemaline myopathy, with fibers shifting towards a non-oxidative phenotype independently of MYH-based fiber type. We also characterize novel transcriptomic and proteomic features of slow and fast skeletal muscle fibers, including identifying several muscle fiber type-specific polypeptides, termed microproteins, encoded by transcripts annotated as non-coding RNA. Overall, our data indicates that skeletal muscle fiber heterogeneity is multi-dimensional with sources of variation beyond myosin heavy chain isoforms.

61 **Introduction**

62 Cellular heterogeneity is an inherent feature of all biological systems, allowing for cellular
63 specialization to meet the diverse demands imposed upon tissues and cells[1]. The classic view
64 of skeletal muscle fiber heterogeneity is that motoneurons define the typology of the fibers
65 within a motor unit, with fiber types (i.e. type 1, type 2A, and type 2X in humans) being
66 defined by myosin heavy chain isoform (MYH) characteristics[2]. This was first based on its
67 ATPase pH lability[3,4] and later by its molecular MYH expression[5]. However, skeletal muscle
68 fibers are increasingly being viewed along a continuum, as opposed to discrete fiber types[6],
69 fueled by the identification and subsequent acceptance of the existence of "hybrid" fibers that
70 express varying proportions of multiple MYHs simultaneously. Nonetheless, the field still relies
71 heavily on MYHs as primary classifiers of muscle fibers, a perspective that might be limited
72 and heavily biased by early studies in rodents, displaying a different MYH expression profile
73 and thus fiber type range than humans[2]. The picture is further complicated by different
74 skeletal muscles displaying specialized fiber type profiles within humans[7]. The *vastus lateralis*
75 is a mixed muscle type with average (and therefore representative) MYH expression profiles[7].
76 Together with this, its accessibility for sampling makes it the most commonly studied muscle
77 in humans.

78

79 An unbiased exploration of skeletal muscle fiber diversity with powerful omics tools is thus
80 heavily warranted, but challenging, in part owing to the multinucleated nature of skeletal
81 muscle fibers. Nonetheless, both transcriptomics[8,9] and proteomics[10] technologies have
82 recently experienced a sensitivity revolution due to various technological advances, making
83 profiling of skeletal muscle at a single fiber resolution now possible. As a result, notable
84 progress has already been made in describing the single muscle fiber diversity and responses

85 to atrophic stimuli and aging[11-18]. Importantly, these technological advances lend themselves
86 to being advantageous in the clinical setting, helping to describe in greater detail and precision
87 the dysregulation associated with disease. For example, the underlying pathophysiology of
88 nemaline myopathy, one of the most prevalent genetic muscle disorders (MIM 605355 and
89 MIM 161800), is complex and convoluted[19,20], thus a deeper characterization of skeletal
90 muscle fiber dysregulation may spur significant developments in our understanding of the
91 disease.
92
93 Our methodological development of transcriptome and proteome profiling of single skeletal
94 muscle fibers manually isolated from human biopsy specimens, and their application to over
95 a thousand fibers each, enabled us to investigate the cellular heterogeneity of human skeletal
96 muscle fibers. In doing so, we demonstrate the power of muscle fiber phenotyping at the
97 transcriptomic and proteomic level, identifying that metabolic, ribosomal, and cell junction
98 proteins are important sources of variation among muscle fibers. Furthermore, with our
99 proteomics workflow we characterize the clinical implications of nemaline myopathies within
100 single skeletal muscle fibers, revealing a coordinated shift towards non-oxidative fibers
101 independently of MYH-based fiber type.
102
103 **Results**
104
105 *Development of high-sensitivity and high-throughput single muscle fiber transcriptomic and*
106 *proteomic pipelines*
107

108 To investigate the heterogeneity of human skeletal muscle fibers, we developed two novel
109 workflows to enable transcriptome and proteome profiling of single skeletal muscle fibers (**Fig**
110 **1A and 1 S1A**). Several methodological steps were developed and optimized, from sample
111 storage and preservation of RNA and protein integrity to optimizing the throughput of each
112 method. This was achieved for transcriptome analysis by inserting sample-specific molecular
113 barcodes during the initial reverse transcription step, enabling pooling of 96 fibers for further
114 efficient downstream processing. Rich transcriptome data was further obtained by deeper
115 sequencing (± 1M reads per fiber) compared to conventional single cell methods[21]. For
116 proteomics, the combination of a short chromatographic gradient (21 minutes) and timsTOF
117 DIA-PASEF-based mass spectrometry was used to optimize proteome depth, whilst
118 maintaining a high-throughput[22,23]. To investigate skeletal muscle fiber heterogeneity in the
119 healthy state, the transcriptome was determined for 1050 individual fibers from 14 healthy
120 adult donors, whilst the proteome was determined for 1038 fibers from 5 healthy adult donors
121 (**Table S1)**. These datasets will be referred to as the 1000 fiber transcriptome and proteome
122 datasets, respectively, throughout this manuscript. Our approach detected a total of 27237
123 transcripts and 2983 proteins in the 1000 fiber transcriptomics and proteomics studies (**Fig**
124 **1A, Table S2-3**). After filtering for >1000 detected genes and for 50% valid values within each
125 fiber in both transcriptomics and proteomics datasets, respectively, downstream
126 bioinformatic analyses were performed on 925 and 974 fibers in the transcriptome and
127 proteome, respectively. On average 4257 ± 1557 genes and 2015 ± 234 proteins (mean ± SD)
128 were detected per fiber after filtering, with limited inter-individual variation (**Fig 1 S1B-C,**
129 **Table S4-5**). The intra-individual variation within a participant was more substantial however,
130 most likely due to differences in RNA/protein yield among fibers of different length and cross-
131 sectional area. For the majority of proteins (>2000), the coefficient of variation was below 20%

132 (**Fig 1 S1D**). Both methodologies captured a wide dynamic range of transcripts and proteins,
133 with features known to be important for muscle contraction being highly expressed (e.g.
134 ACTA1, MYH2, MYH7, TNNT1, TNNT3) (**Fig 1 S1E-F**). A large part of the detected features were
135 shared between the transcriptome and proteome datasets (**Fig 1 S1G**), alongside a reasonable
136 correlation (r = 0.52) in average UMI counts/LFQ intensities for these features (**Fig 1 S1H**).
137
138 *Type 2X is not a distinct fiber type*
139
140 We initially set out to define the MYH-based fiber type of each fiber using an optimized
141 methodology, leveraging the high sensitivity and dynamic range of MYH expression in the
142 omics datasets. Previous studies have used arbitrary cut-offs to assign a fiber as pure type 1,
143 type 2A, type 2X, or hybrid, based on a fixed percentage of expression for the different
144 MYHs[11,14,24]. We employed a different approach, in which we ranked the expression of each
145 fiber by the MYHs used for fiber typing: MYH7, MYH2 and MYH1, corresponding to type 1,
146 type 2A and type 2X fibers, respectively. We then mathematically calculated the bottom knee
147 for each of the resulting curves and used it as a threshold to assign a fiber as being positive
148 (above threshold) or negative (below threshold) for each MYH (**Fig 1B-D**). These data show
149 that MYH7 (**Fig 1B**) and MYH2 (**Fig 1C**) have a more pronounced on/off expression profile on
150 the RNA level, compared to the protein level. Indeed, at the protein level, very few fibers did
151 not express MYH7 and no fibers had 100% MYH2 expression. Next, we used the determined
152 expression thresholds to assign MYH-based fiber types for all fibers in each dataset. For
153 example, a $MYH7^{+}/MYH2^{-}/MYH1^{-}$ was assigned as type 1, and a $MYH7^{-}/MYH2^{+}/MYH1^{+}$ was
154 assigned as a hybrid type 2A/2X fiber (see **Table S6** for full description). When combining all
155 fibers, a very similar MYH-based fiber type distribution was observed at the RNA (**Fig 1E**) and

156 protein (**Fig 1F**) levels, with an expected inter-individual variation in relative MYH-based fiber
157 type composition (**Fig 1 S2A**). Most fibers were considered pure type 1 (34-35%) or type 2A
158 (36-38%), although a substantial number of hybrid 2A/2X fibers (16-19%) were also detected.
159 A striking discrepancy was that pure type 2X fibers could only be detected at the RNA but not
160 at the protein level, indicating that fast MYH expression is, at least in part, post-
161 transcriptionally regulated.
162
163 We validated the MYH-based fiber typing from the proteomics data against an antibody-based
164 dot blot technique, in which both methodologies were in 100% agreement on the
165 identification of both pure type 1 and type 2A fibers (**Fig 1 S2B**). However, the increased
166 sensitivity of the proteomics-based approach was superior in identifying hybrid fibers and in
167 quantifying the proportion of each MYH within each fiber. These data demonstrate the
168 efficacy of using an unbiased high-sensitivity omics-based approach for the characterization
169 of skeletal muscle fiber types.
170
171 We then utilized the full depth of information that transcriptomics and proteomics provide to
172 classify fibers in an unbiased manner based on their whole transcriptome or proteome. Using
173 uniform manifold approximation and projection (UMAP) for dimension reduction of 6
174 principal components (**Fig 1 S3 A-B**), we were able to visualize the variation in fibers in the
175 transcriptome (**Fig 1G**) and proteome (**Fig 1H**). Interestingly, fibers did not cluster by
176 participant in either the transcriptomics or proteomics datasets (**Fig 1 S3C-D**), nor by test day
177 (**Fig 1 S3E**), indicating that intra-individual variance in skeletal muscle fibers outweighs inter-
178 individual variance. Two distinct clusters were apparent in the UMAP plots, which represented
179 "fast" and "slow" fibers (**Fig 1G-H**). MYH7^{+} (slow) fibers clustered to the positive side of

180 UMAP1, and MYH2$^+$ and MYH1$^+$ (fast) fibers clustered to the negative side of UMAP1 (**Fig 1I-**
181 **J**). No distinction between the various fast MYH-based fiber types (i.e. type 2A, type 2X, or
182 hybrid 2A/2X) could be identified, however, suggesting that when the whole transcriptome or
183 proteome is taken into account, the expression of MYH1 (**Fig 1 I-J**), or other classical markers
184 of type 2X fibers like ACTN3 or MYLK2 (**Fig 1 S4A-B**), does not discriminate between distinct
185 fiber types. Furthermore, in contrast to MYH2 and MYH7, few transcripts or proteins positively
186 correlate with MYH1 (**Fig 1 S4C-H**), suggesting that MYH1 abundance does not adequately
187 reflect the muscle fiber transcriptome/proteome. Similar conclusions can be drawn when
188 assessing the blended expression of the three MYH isoforms on a UMAP level (**Fig 1 S4I-J**).
189 Thus, whilst type 2X fibers can be identified at the transcriptional level based solely on the
190 quantification of MYHs, MYH1$^+$ fibers are not distinct from other fast fibers when the whole
191 transcriptome or proteome is considered.
192
193 *Considerable skeletal muscle fiber heterogeneity beyond myosin heavy chain isoforms*
194
195 As an initial exploration of fiber heterogeneity beyond MYHs, we assessed four established
196 slow fiber type-specific proteins: TPM3, TNNT1, MYL3, and ATP2A2[2]. In both transcriptomics
197 (**Fig 2 S1A**) and proteomics (**Fig 2 S1B**) approaches, the slow isoforms exhibited a high,
198 although not perfect, Pearson correlation coefficient with MYH7. Approximately 25 and 33%
199 of the fibers in the transcriptomics (**Fig 2 S1C**) and proteomics (**Fig 2 S1D**) approaches,
200 respectively, were not classified as pure slow fibers by all gene/protein isoforms. Thus, fiber
201 typing based on multiple gene/protein isoforms introduces additional complexity, even with
202 well-known proteins that are assumed to be fiber type-specific. This suggests that fiber typing

203 based on isoforms of a single family of genes/proteins is likely inadequate to capture the true
204 heterogeneity of skeletal muscle fibers.
205
206 To further investigate the omics-wide phenotypical variability between human skeletal muscle
207 fibers, we applied unbiased dimensionality reduction by principal component analysis (PCA)
208 to our data (**Fig 2A**). Similarly to the UMAP plot, neither participant nor test day influenced
209 the clustering of fibers at the PCA level (**Fig 2 S2A-C**). MYH-based fiber type was explained by
210 PC2 in both datasets, displaying clusters for slow type 1 fibers and a second cluster containing
211 the fast type 2A, type 2X and hybrid type 2A/2X fibers (**Fig 2A**). These two clusters were
212 bridged in both datasets by a small number of hybrid type 1/2A fibers. As expected, over-
213 representation analysis of the top PC drivers confirmed that PC2 is driven by contractile and
214 metabolic features (**Fig 2B & 2 S2D-E, Table S7-9**). In general, the MYH-based fiber types
215 adequately explain the continual variance along PC2, except for the so-called type 2X fibers,
216 which were spread across the entirety of the transcriptomic fast cluster.
217
218 Unexpectedly, MYH-based fiber type explained only the second greatest degree of variability
219 (PC2), indicating that other biological factors (PC1) independent of MYH-based fiber type,
220 have a substantial role in regulating skeletal muscle fiber heterogeneity. Over-representation
221 analysis of the top drivers in PC1 indicated that variance within PC1 was determined primarily
222 by cell-cell adhesion and ribosomal content in the transcriptome, and costamere and
223 ribosomal proteins in the proteome (**Fig 2B & 2 S2D-E, Table S9**). In skeletal muscle, the
224 costamere connects the Z-disk to the sarcolemma and participates in force transmission and
225 signaling[25]. Annotating PCA plots with cell-cell adhesion (transcriptome, **Fig 2C**) and

226 costamere (proteome, **Fig 2D**) features showed a strong shift to the left side of PC1, suggesting
227 an enrichment for these features in some fibers.
228
229 Closer inspection of fiber clustering at the UMAP level showed a MYH-based fiber type-
230 independent gradient of expression for most features, rather than distinct subclusters of
231 muscle fibers. This continuum holds true for several genes related to pathological conditions
232 (**Fig 2E**), such as *CHCHD10* (neuromuscular disorders)[26], *SLIT3* (muscle loss)[27] and *CTDNEP1*
233 (muscle disease)[28]. This same continuum was observed in the proteome, with proteins related
234 to neurological diseases (UGDH)[29], insulin signaling (PHIP)[30] and transcription (HIST1H2AB)
235 (**Fig 2F**). These data collectively show that slow/fast fiber type independent heterogeneity
236 across fibers is of a continual nature.
237
238 *Fiber heterogeneity is post-transcriptionally regulated by ribosomal heterogeneity*
239
240 Interestingly, drivers of PC2 showed a good correlation (r = 0.663) between the transcriptome
241 and proteome (**Fig 2G**), indicating that the slow and fast fiber types, particularly the contractile
242 and the metabolic profile of skeletal muscle fibers, are transcriptionally regulated. However,
243 there was no correlation between the drivers of PC1 in the transcriptome and the proteome
244 (r = -0.027) (**Fig 2H**). This suggests that slow/fast fiber type-independent variance is for a large
245 part post-transcriptionally regulated. Since PC1 variance was largely explained by ribosomal
246 gene ontology terms and given that ribosomes play a profound and specialized role in the cell
247 by actively participating and influencing protein translation[31], we next set out to explore this
248 unexpected ribosomal heterogeneity.
249

250 We first colored the proteomics PCA plot based on the relative abundance of the proteins
251 within the "cytosolic ribosome" GOCC term (**Fig 3A**). Although the term was enriched on the
252 positive side of PC1, and a slight gradient could be observed accordingly, ribosomal proteins
253 were driving separation in both directions of PC1 (**Fig 3A**). Amongst the ribosomal proteins
254 enriched in the negative direction of PC1 were RPL18, RPS18 and RPS13 (**Fig 3B**), whilst RPL31,
255 RPL35 and RPL38 (**Fig 3C**) were major drivers in the positive direction of PC1. Interestingly,
256 RPL38 and RPS13 are highly expressed in skeletal muscle when compared to other tissues (**Fig**
257 **3 S1A**). These distinct ribosomal signatures across PC1 could not be observed in the
258 transcriptome (**Fig 3 S1B**), indicating that this phenomenon is post-transcriptionally regulated.
259
260 The concept of ribosomal heterogeneity and specialization was previously introduced, where
261 the presence of distinct subpopulations of ribosomes (ribosomal heterogeneity) can directly
262 influence protein translation in different tissues[32] and cells[33] by selectively translating specific
263 mRNA transcript pools[34] (ribosomal specialization). To identify sub-sets of ribosomal proteins
264 that are co-expressed within skeletal muscle fibers, we performed an unsupervised
265 hierarchical clustering analysis of ribosomal proteins within the proteome (**Fig 3D, Table S10**).
266 As expected, ribosomal proteins did not cluster by MYH-based fiber type. However, we
267 identified three distinct clusters of ribosomal proteins; the first of which (ribosomal_cluster_1)
268 was coregulated alongside RPL38, therefore elevated in fibers in the positive direction of PC1.
269 The second cluster (ribosomal_cluster_2) was coregulated alongside RPS13 and was elevated
270 in fibers in the negative direction of PC1. A third cluster (ribosomal_cluster_3) displayed no
271 coordinated differential expression within skeletal muscle fibers and could therefore be
272 considered "core" ribosomal proteins within skeletal muscle. Both ribosomal_cluster_1 and
273 ribosomal_cluster_2 contain ribosomal proteins previously demonstrated to regulate

274 selective translation (e.g. RPL10A, RPL38, RPS19 and RPS25) and functionally influence
275 development (e.g. RPL10A, RPL38)[34-38]. In line with the results from the PCA analysis, the
276 observed heterogeneous abundance of these ribosomal proteins across fibers was also of a
277 continual nature (**Fig 3 S1C**).
278
279 To visualize the position of the ribosomal proteins that display heterogeneity within the
280 ribosome, we utilized a structural model of the human 80S ribosome (Protein Data Bank:
281 4V6X)[39] (**Fig 3E**). Upon highlighting the ribosomal proteins that belong to the different
282 ribosomal clusters, they were not located in close proximity, showing that our approach did
283 not enrich for a particular area/section of the ribosome. Yet interestingly, ribosomal_cluster_2
284 contained a lower proportion of large ribosomal subunit proteins than ribosomal_cluster_1
285 and ribosomal_cluster_3 (**Fig 3 S1D**). We observed that the majority of the proteins that
286 display variable stoichiometry within skeletal muscle fibers are located on the surface of the
287 ribosome (**Fig 3E**), which is consistent with an ability to interact with internal ribosome entry
288 site (IRES) elements within distinct mRNA populations to coordinate selective translation[40,41].
289 Furthermore, numerous proteins that display variable stoichiometry within skeletal muscle
290 fibers are located close to functional regions, such as the mRNA exit tunnel (**Fig 3F**), which can
291 selectively regulate translation elongation and arrest of specific nascent peptides[42]. Overall,
292 our data identifies that skeletal muscle ribosomal protein stoichiometry displays
293 heterogeneity, driving variance between skeletal muscle fibers.
294
295 *Slow and fast fiber signatures and their transcriptional regulators*
296

297 We next set out to identify novel features of fast and slow skeletal muscle fibers and how
298 these are transcriptionally regulated. Comparing the fast and slow clusters defined in the
299 UMAPs of both datasets (**Fig 1G-H & inlays Fig 4A-B**), transcriptome and proteome analysis
300 yielded 1366 and 804 differentially abundant features, respectively (**Fig 4A-B, Table S11-14**).
301 Expected differences in sarcomeric (e.g. tropomyosin and troponin), excitation-contraction
302 coupling (SERCA isoforms) and energy metabolism-related (e.g. ALDOA and CKB) features
303 were observed. In addition, transcripts and proteins regulating protein ubiquitination
304 displayed differences between fast and slow fibers (e.g. *USP54, SH3RF2,* USP28 and USP48)
305 (**Fig 4A-B**). Furthermore, the microprotein-encoding gene *RP11-451G4.2 (DWORF)*, which has
306 previously been shown to be differentially expressed between lamb muscle fiber types[43] and
307 to enhance SERCA activity in cardiac muscle[44], was significantly up-regulated in slow skeletal
308 muscle fibers (**Fig 4A**). Also at the single fiber level, clear differences could be observed for
309 known features such as the metabolism-related isoforms of lactate dehydrogenase (LDHA and
310 LDHB, **Fig 4C** and **Fig 4 S1A**)[45,46], as well as previously unknown fiber type-specific features
311 (e.g. *IRX3*, *USP54*, USP28, and DPYSL3) (**Fig 4C**). There was a reasonable overlap of
312 differentially expressed features (**Fig 4 S1B**) and correlation of fold changes between the
313 transcriptomic and proteomic datasets, primarily driven by the large expression differences in
314 sarcomeric features (**Fig 4 S1C**). Notably, some features (e.g. USP28, USP48, GOLGA4, AKAP13)
315 showed strong post-transcriptional regulation with slow/fast fiber type-specific expression
316 profiles only at the proteome level (**Fig 4 S1C**).
317
318 We next performed over-representation analysis on the differentially abundant genes and
319 proteins (**Fig 4D, Table S15**). Enriched pathways of features that were differential in both
320 datasets showed expected differences such as fatty acid beta-oxidation and ketone metabolic

321 process (slow fibers), myofilament/muscle contraction (fast and slow fibers, respectively) and
322 carbohydrate catabolic process (fast fibers). Serine/Threonine protein phosphatase activity
323 was also enriched in fast fibers, driven by features such as phosphatase regulatory and
324 catalytic subunits (PPP3CB, PPP1R3D, and PPP1R3A), known to regulate glycogen
325 metabolism[47] (**Fig 4 S1D-E**). Other enriched pathways in fast fibers were Processing (P-) bodies
326 (YTHDF3, TRIM21, LSM2) in the proteome (**Fig 4 S1F**), possibly related to post-transcriptional
327 regulation[48], and transcription factor activity (*SREBF1*, *RXRG*, *RORA*) in the transcriptome (**Fig**
328 **4 S1G**). Slow fibers showed enrichment for oxidoreductase activity (*BDH1*, *DCXR*, *TXN2*) (**Fig 4**
329 **S1H**), amide binding (*CPTP*, *PFDN2*, *CRYAB*) (**Fig 4 S1I**), extracellular matrix (*CTSD*, *ADAMTSL4*,
330 *LAMC1*) (**Fig 4 S1J**) and receptor-ligand activity (*FNDC5*, *SPX*, *NENF*) (**Fig 4 S1K**).
331
332 To get more insights into the transcriptional regulation of slow/fast fiber type signatures, we
333 performed transcription factor enrichment analysis using SCENIC[49] (**Table S16**). Many
334 transcription factors were significantly enriched between fast and slow fibers (**Fig 4E**). This
335 included transcription factors such as *MAFA*, previously linked to the development of fast
336 fibers[50], but also multiple novel transcription factors potentially involved in the fiber type
337 specific gene program. These included *PITX1*, *EGR1* and *MYF6* as the most enriched
338 transcription factors within fast fibers (**Fig 4E**). Conversely, *ZSCAN30* and *EPAS1* (also known
339 as *HIF2A*) were the most enriched transcription factors within slow fibers (**Fig 4E**). In line with
340 this, *MAFA* expression levels were higher in the UMAP area corresponding to fast muscle
341 fibers, whereas an opposite expression pattern was observed for *EPAS1* (**Fig 4F**).
342
343 *Non-coding RNA and associated microproteins in human skeletal muscle fibers*
344

345 Alongside known protein-coding genes, there exists a multitude of non-coding RNA biotypes,
346 potentially involved in the regulation of human development and disease[51,52]. Several non-
347 coding RNAs displayed fiber type specificity in the transcriptomics dataset (**Fig 5A & Table**
348 **S17**), including *LINC01405*, which is very specific to slow fibers and is reported to be
349 downregulated in muscle of mitochondrial myopathy patients[53]. Conversely, *RP11-255P5.3,*
350 corresponding to the *lnc-ERCC5-5* gene (https://lncipedia.org/db/transcript/lnc-ERCC5-5:2)[54]
351 displayed fast fiber type-specificity. Both *LINC01405* (https://tinyurl.com/x5k9wj3h) and
352 *RP11-255P5.3* (https://tinyurl.com/29jmzder) display specificity to skeletal muscle (**Fig 5 S1A-**
353 **B**) and have very few or no known contractile genes within a 1Mb genomic neighborhood,
354 suggesting a specialized role in fiber type regulation rather than a regulatory role for a
355 neighboring contractile gene. The slow/fast fiber type-specific specific expression profiles of
356 *LINC01405* and *RP11-255P5.3* were independently validated using RNAscope (**Fig 5B-C)**.
357
358 Recently, it has become apparent that numerous assumed non-coding transcripts code for
359 transcribed microproteins, some of which regulate muscle function[44,55]. To identify novel
360 microproteins with potential fiber-type specificity, we searched our 1000 fiber proteomic
361 dataset using a custom FASTA file containing sequences from the detected non-coding
362 transcripts (n = 305) from the 1000 fiber transcriptome dataset (**Fig 5D**). This resulted in the
363 identification of 197 novel microproteins arising from 22 distinct transcripts, of which 71
364 microproteins display differential regulation between slow and fast skeletal muscle fibers (**Fig**
365 **5 S1C and Table S18**). Three microprotein products were identified for *LINC01405*, of which
366 one displays a slow-fiber type specificity similar to its transcript (**Fig 5E and 5 S1D**). Thus, we
367 identify *LINC01405* as a microprotein-encoding gene, which displays specificity for slow
368 skeletal muscle fibers.

369

370 *Nemaline myopathies induce a shift towards faster, less oxidative skeletal muscle fibers*

371

372 Having developed a comprehensive workflow to characterize the proteome of single muscle
373 fibers at scale and discovered novel regulators of fiber heterogeneity in the healthy state, we
374 applied this pipeline to understand how nemaline myopathy impacts skeletal muscle fiber
375 heterogeneity. Nemaline myopathy is a genetic muscular disorder that causes muscle
376 weakness, resulting in a range of complications for the affected children including respiratory
377 difficulties, scoliosis, and physical immobility[19,20]. Typically, in nemaline myopathy, pathogenic
378 variants in genes such as actin alpha 1 (*ACTA1*) drive the fiber type composition towards slow
379 fiber predominance, although this effect is heterogenous. The only clear exception is the
380 troponin T1 (*TNNT1*) nemaline myopathy, in which a fast fiber predominance is seen. Thus, a
381 deeper characterization of the heterogeneity behind the skeletal muscle fiber dysregulation
382 observed in nemaline myopathies may help untangle the complex relationship between these
383 diseases and muscle fiber types.

384

385 Muscle fibers isolated from patients with *ACTA1*- and *TNNT1*-mutation derived nemaline
386 myopathies display substantial myofiber atrophy or hypotrophy, compared to healthy controls
387 (n = 3 per group) (**Fig 6A, Table S19**), which provides considerable technical challenge arising
388 from the limited material for proteomic analysis. Nonetheless, we were able to detect 2485
389 proteins from 272 skeletal muscle fibers. After filtering for a minimum of 1000 quantified
390 proteins per fiber, downstream bioinformatic analyses were performed on 250 fibers. On
391 average of 1573 ± 359 proteins were quantified per fiber after filtering (**Fig 6 S1A, Table S20-**
392 **21**). Importantly, only a modest reduction in proteome depth was apparent in samples from

393 patients with nemaline myopathy, despite the markedly reduced fiber size. Furthermore,
394 processing of this data with our custom FASTA file (including non-coding transcripts) identified
395 five microproteins within the skeletal muscle fibers from nemaline myopathy patients (**Table**
396 **S22**). A wide dynamic range was apparent in the proteome, whilst the shared proteins in the
397 control participants correlated well with those in the previous analysis of the 1000 fiber
398 proteome study (**Fig 6 S1B-C**).
399
400 As nemaline myopathies influence the MYH-based fiber type proportions within skeletal
401 muscle[19,20], we first investigated the MYH-based fiber type of our nemaline myopathy patients
402 and controls. Fiber type was determined using the unbiased approach described previously
403 for the 1000 fiber studies (**Fig 6 S1D-E**) and once again pure type 2X fibers could not be
404 identified (**Fig 6B**). We observed a heterogeneous effect of nemaline myopathies on fiber type,
405 as two patients with *ACTA1* mutations displaying an increased proportion of type 1 fibers,
406 whilst two patients with *TNNT1*-nemaline myopathy displayed a reduced proportion of type
407 1 fibers (**Fig 6B**). Indeed, MYH2 and the fast troponin isoforms were downregulated in *ACTA1*-
408 nemaline myopathy (TNNC2, TNNI2, and TNNT3), whilst MYH7 was downregulated in *TNNT1*-
409 nemaline myopathy (**Fig 6 S2A**). This is in line with previous reports of heterogeneous fiber
410 type switching in nemaline myopathies[19,20]. We validated these findings using
411 immunohistochemistry, finding type 1 fiber predominance in *ACTA1*-nemaline myopathy
412 patients, while the opposite was observed in *TNNT1-nemaline myopathy* patients (**Fig 6A**).
413
414 At the single-fiber proteome level, skeletal muscle fibers from *ACTA1*- and *TNNT1*-nemaline
415 myopathy patients clustered away from the majority of control fibers, with TNNT1- nemaline
416 myopathy fibers tending to be the most severely affected (**Fig 6C**). This was particularly

417 apparent when we produced a PCA plot of pseudo-bulked fibers for each patient, with *TNNT1*-
418 nemaline myopathy patients 2 & 3 lying furthest from the control samples (**Fig 6 S2B, Table**
419 **S23**). To further understand how fibers from myopathy patients compare to the healthy
420 condition, we capitalized on the depth of information provided by our analysis in 1000 fiber
421 proteome study from healthy adult participants. We projected the fibers from our myopathy
422 data set (both *ACTA1*- and *TNNT1*-nemaline myopathy patients and controls) onto the PCA
423 determined from the 1000 fiber proteome study (**Fig 6D**). Control fibers displayed a similar
424 distribution of MYH-based fiber type along PC2 as the 1000 fiber proteome study. However,
425 the majority of fibers from nemaline myopathy patients shifted downwards along PC2,
426 overlapping with the healthy fast fibers, irrespective of their own MYH-based fiber type. Thus,
427 despite evidence for a fiber-type shift towards type 1 fibers in *ACTA1*-nemaline myopathy
428 patients when quantified using MYH-based approaches, both *ACTA1*- and *TNNT1*-nemaline
429 myopathies shift the skeletal muscle fiber proteome to resemble fast fibers.
430
431 We next directly compared each patient group with the samples from healthy controls,
432 resulting in 256 and 552 differentially abundant proteins in *ACTA1*- and *TNNT1*-nemaline
433 myopathies, respectively (**Fig 6E-G & Fig 6 S2C, Table S24**). Gene set enrichment analysis
434 identified the coordinated reduction of mitochondrial proteins (**Fig 6H-I, Table S25**).
435 Surprisingly, this was completely independent of MYH-based fiber type (**Fig 6H & Fig 6 S2D-I,**
436 **Table S26**), despite the divergent fiber type predominance between *ACTA1*- and *TNNT1*-
437 nemaline myopathies. Three microproteins were also regulated by either *ACTA1*- or *TNNT1*-
438 nemaline myopathies. Two of those microproteins, ENSG00000215483_TR14_ORF67 (also
439 known as *LINC00598* or *Lnc-FOXO1*) and ENSG00000229425_TR25_ORF40 (*lnc-NRIP1-2*)
440 displayed differential abundance only within type 1 fibers, with

441 ENSG00000215483_TR14_ORF67 having previously reported to play a role in cell cycle
442 regulation[56]. On the other hand, ENSG00000232046_TR1_ORF437 (corresponding to
443 *LINC01798*) was upregulated in both type 1 and type 2 fibers from *ACTA1*-nemaline myopathy
444 when compared to healthy controls (**Fig 6 S3A, Table S27**). Conversely, ribosomal proteins
445 were largely unaffected by nemaline myopathies, although RPS17 was downregulated in
446 *ACTA1*-nemaline myopathy (**Fig 6E**).
447
448 Enrichment analysis also identified the up-regulation of immune system process in both
449 *ACTA1*- and *TNNT1*-nemaline myopathies, as well as cell adhesion in *TNNT1*-nemaline
450 myopathy (**Fig 6H**). The enrichment of these extracellular terms, was reflected by extracellular
451 matrix proteins driving the PCA in the negative direction in both PC1 and PC2, i.e. towards the
452 most affected fibers (**Fig 6J**). Both patient groups overexpressed extracellular proteins
453 involved in immune response and the sarcolemma repair machinery, such as annexins
454 (ANXA1, ANXA2, ANXA5)[57,58] and their interactor S100A11[59] (**Fig 6 S3B-C**). This process has
455 been previously reported to be upregulated in muscle dystrophies[60], yet to our knowledge it
456 has not been associated with nemaline myopathies before. A normal function of this
457 molecular machinery is required for both sarcolemma membrane repair upon injury and for
458 the fusion of new myoblasts to muscle fibers[58,61]. Therefore, an up-regulation of this process
459 in both patient groups suggests a reparative response to damage caused by myofibril
460 instability.
461
462 The effects of each nemaline myopathy were well correlated (r = 0.736) and displayed
463 reasonable overlap (**Fig 6 S2A-B**), indicating that *ACTA1*- and *TNNT1*-nemaline myopathies
464 induce similar effects on the proteome. Nonetheless, a number of proteins displayed

465 regulation in only *ACTA1*- or *TNNT1*-nemaline myopathies (**Fig 6 S2A & S2C**). MFAP4, a pro-
466 fibrotic protein, was one of the most up-regulated proteins in *TNNT1*-nemaline myopathy
467 whilst unchanged in *ACTA1*-nemaline myopathy. SKIC8, a component of the PAF1C complex,
468 which regulates the transcription of *HOX* genes[62], was down-regulated in *TNNT1*-nemaline
469 myopathy but was unaffected in *ACTA1*-nemaline myopathy (**Fig 6 S2A**). Direct comparisons
470 between *ACTA1*- and *TNNT1*-nemaline myopathies identify a greater effect of *TNNT1*-
471 nemaline myopathies on the reduction of mitochondrial proteins and the increase of immune
472 system proteins (**Fig 6G-H & Fig 6 S2C & S2H-I**). These data are consistent with the greater
473 degree of atrophy/hypotrophy apparent in *TNNT1*- compared to *ACTA1*-nemaline myopathies
474 (**Fig 6A**), indicating that *TNNT1*-nemaline myopathy is the more severe form of the disease.
475
476 In order to assess whether the observed effects of nemaline myopathy were also present at
477 the whole muscle-level, we conducted a bulk proteome analysis on muscle biopsies from the
478 same *TNNT1*-nemaline myopathy patients and compared them against control individuals (n
479 = 3 per group) **(Fig 6 S4A, Table S28)**. As expected, upon PCA, control individuals tightly
480 clustered together whereas, similarly to the single fiber analysis, and *TNNT1*-nemaline
481 myopathy patients displayed a higher inter-sample variance **(Fig 6 S4B)**. The bulk analysis was
482 able to recapitulate the differentially expressed proteins **(Fig 6 S4C, Table S29)** and biological
483 processes **(Fig 6 S4D, Table S30)** highlighted in the single fiber comparison, although lost the
484 potential to discriminate between fiber types, and did not account for the heterogeneous
485 effect of the disease across different fibers.
486
487 Together, these data demonstrate that single muscle fiber proteomics can illuminate clinical
488 biology that is unapparent using targeted approaches such as immunoblotting. Furthermore,

489 these data highlight the limitations of solely relying upon MYH-based fiber typing to describe
490 phenotypic adaptations. Indeed, despite divergent MYH-based fiber type switching in actin
491 and troponin nemaline myopathies, both nemaline myopathies uncouple the MYH-based
492 fiber type from skeletal muscle fiber metabolism, shifting towards a faster, less oxidative
493 muscle proteome.
494
495 **Discussion**
496 Cellular heterogeneity is important to enable tissues to meet a wide range of demands. In
497 skeletal muscle, this has classically been described by fiber types characterized by varying
498 degrees of force production and fatigability. It is apparent, however, that this explains just a
499 fraction of the variation in skeletal muscle fibers, with far greater variability, complexity and
500 nuance residing in skeletal muscle fibers than previously believed. With the advent and
501 development in technologies, these elements that regulate skeletal muscle fibers are now
502 able to be elucidated. Indeed, our data indicates that type 2X fibers may not be a distinct sub-
503 classification of skeletal muscle fibers. Furthermore, we identify metabolic, ribosomal, and cell
504 junction proteins as major determinants of skeletal muscle fiber heterogeneity. By applying
505 our proteomics workflow to samples from nemaline myopathy patients, we further evidence
506 that MYH-based fiber typing does not capture the complete heterogeneity of skeletal muscle,
507 particularly when the system is perturbed. Indeed, nemaline myopathies induce a shift
508 towards faster less oxidative fibers regardless of their MYH-based fiber type.
509
510 Skeletal muscle fibers have been classified since the 19th century[2,63]. Recent omics-based
511 analyses have enabled us to start understanding expression profiles and responses to various
512 stimuli specific to distinct MYH-based fiber types[11-16,24,46,64,65]. As demonstrated herein, omics

513 approaches also have the advantage of increased sensitivity in the quantification of fiber-type
514 markers over traditional antibody-based approaches, whilst also not relying on the
515 quantification of a single (or few) markers for determining skeletal muscle fiber type. We
516 leveraged complementary transcriptomics and proteomics workflows, and integrated the
517 results, to explore the transcriptional and post-transcriptional regulation of human skeletal
518 muscle fiber heterogeneity. This pipeline resulted in the observation that pure type 2X fibers
519 could not be identified at the protein level in *vastus lateralis* skeletal muscle of our cohort of
520 young healthy males. This is in line with previous single-fiber studies identifying <1% pure type
521 2x fibers in healthy *vastus lateralis*[66], although this should be confirmed in other muscles in
522 the future. The discrepancy between the identification of near pure type 2X fibers at the
523 mRNA level but only hybrid type 2A/2X fibers at the protein level is puzzling. mRNA expression
524 of MYH isoforms is not circadian[67], indicating that it is unlikely that we have simply "missed"
525 the on-signal of MYH2 in the apparently pure type 2X fibers at the RNA level. One possible
526 explanation may be differences in the protein and/or mRNA stability of MYH isoforms, though
527 this is purely hypothetical. Indeed, no fast fiber was 100% pure for any MYH isoform, though
528 whether levels of MYH1 mRNA expression in the range of 70-90% could result in similar MYH1
529 and MYH2 abundance at the protein level is unclear. Nonetheless, when the whole
530 transcriptome or proteome is considered, clustering-based analyses could only confidently
531 identify two distinct clusters, which represented slow and fast skeletal muscle fibers regardless
532 of their exact MYH composition. This is consistent with analyses using single nuclei
533 transcriptomics approaches which commonly identify only two distinct clusters of
534 myonuclei[68-70]. Furthermore, whilst previous proteomics-based studies have identified type
535 2X fibers, these fibers did not cluster away from the rest of the fast fibers and only displayed
536 a handful of differentially abundant proteins compared to other MYH-based fiber types[14].

537 These findings indicate that we should revert to the view of muscle fiber classification from
538 the early twentieth century and classify human skeletal muscle fibers not into three distinct
539 classifications based on MYHs, but instead into just two clusters based on their metabolic and
540 contractile properties[63].
541
542 Better still, we should consider muscle fiber heterogeneity in multiple dimensions. Previous
543 omics studies already pointed in this direction, by showing that skeletal muscle fibers do not
544 form discrete clusters, yet fall along a continuum[11,13,14,64,71]. Here, we found that over and
545 above the variance within the contractile and metabolic signatures of skeletal muscle, fibers
546 could also be separated by features related to the cell junction and translation machinery.
547 Indeed, we identified ribosomal heterogeneity across skeletal muscle fibers that drives a
548 slow/fast-fiber type independent heterogeneity. The underlying reason for such vast
549 slow/fast-fiber type independent heterogeneity amongst fibers is not immediately obvious,
550 though this could allude to a specialized spatial organization within a muscle fascicle to enable
551 an optimal response to specific forces and loads[72], specialized cellular or organ
552 communication with other cell types within the muscle microenvironment[73-75], or differential
553 ribosomal activity in individual fibers. Indeed, ribosomal heterogeneity, via paralog
554 substitution of RPL3 and RPL3L or at an rRNA 2'O-methyl level, has been implicated in skeletal
555 muscle hypertrophy[76,77]. Multi-omics and spatial applications in concert with functional
556 characteristics of single muscle fibers will further advance our understanding of muscle
557 biology on a multi-omics level[78].
558
559 In analyzing the proteome of single muscle fibers from patients with nemaline myopathies,
560 we also demonstrate the utility, power, and applicability of single muscle fiber proteomics in

561 uncovering clinical pathophysiology in skeletal muscle. Furthermore, by comparing our
562 workflow against a bulk proteome analysis, we were able to demonstrate that single muscle
563 fiber proteomics is able to capture the same depth of information than bulk tissue omics and
564 expand on it by including inter-fiber heterogeneity and muscle fiber type into consideration.
565 In addition to observing expected, albeit divergent, differences in fiber-type proportions in
566 *ACTA1*- and *TNNT1*-nemaline myopathies compared to healthy controls[19], we also identified
567 oxidative and extracellular remodeling, which is uncoupled from this MYH-based fiber type
568 switch. Fibrosis has previously been reported for *TNNT1* nemaline myopathy[19]. However, our
569 analysis builds upon this to also identify the up-regulation of stress-related secreted proteins
570 within the extracellular space, such as annexins, involved in the sarcolemma repair
571 machinery[57-59] in fibers from both *ACTA1*- and *TNNT1*-nemaline myopathy patients. Overall,
572 the upregulation of annexins in muscle fibers from nemaline myopathy patients may
573 represent a cellular response to rescue severely atrophying fibers.
574
575 Whilst this study represents the largest omic analysis of intact human single muscle fibers to
576 date, it is not without limitations. We isolated skeletal muscle fibers from a relatively small
577 and homogenous sample of participants and from a single muscle (*vastus lateralis*). In this
578 respect, it is impossible to rule out the existence of specific fiber populations in different
579 muscle types and at the extremes of muscle physiology. For example, we cannot rule out that
580 a sub type of ultra-fast fibers (e.g. pure type 2X fibers) may become apparent in highly trained
581 sprint and/or power athletes[79] or during muscle disuse[66,80]. Furthermore, our limited
582 participant pool did not allow us to investigate sex differences in fiber heterogeneity, in which
583 there are known differences in fiber type proportions between males and females.
584 Furthermore, we were unable to perform transcriptomics and proteomics on the same muscle

585 fibers or in samples from the same participants. As we and others continue to optimize single-
586 cell and single muscle fiber omics-analyses towards ultra-low sample input (as demonstrated
587 here with the analysis of fibers from nemaline myopathy patients), the possibility of
588 combining multi-omics (and functional) approaches in a single muscle fiber is tantalizingly
589 close.
590
591 Collectively, our data identifies and explains transcriptional and post-transcriptional drivers of
592 heterogeneity within skeletal muscle. In particular, we provide data to question long-standing
593 dogmas within skeletal muscle physiology related to the classical definitions of MYH-based
594 fiber-types. In doing so we hope to reignite the debate and ultimately redefine our
595 understanding of skeletal muscle fiber classifications and heterogeneity.
596
597 **Methods**
598 **1000 fiber transcriptomics**
599 **Participant information.** Fourteen participants (12 males / 2 females) volunteered to take part
600 in this study, which was approved by the Ethical Committee of Ghent University Hospital (BC-
601 10237), in agreement with the 2013 Declaration of Helsinki and registered on ClinicalTrials.gov
602 (NCT05131555). General characteristics of the participants can be found in **Table S1**. After oral
603 and written informed consent, participants were medically screened before final inclusion.
604 Participants were young (22-42 years old), healthy (no diseases and non-smoking) and
605 moderately physically active. Maximal oxygen uptake was determined as marker of physical
606 fitness during a graded incremental cycling test, as previously described[81].
607

608 **Muscle biopsy collection.** Muscle biopsies were collected in the rested and fasted state, on
609 three different days, separated by 14 days. As these samples were collected as part of a larger
610 study, on each of these days participants ingested a placebo (lactose), an H1-receptor
611 antagonist (540 mg fexofenadine) or an H2-receptor antagonist (40 mg famotidine) 40
612 minutes before muscle biopsy collection. We have previously shown that these histamine
613 receptor antagonists do not affect the resting skeletal muscle state[81], and no clustering was
614 apparent based on condition in our quality control plots (**Fig 1 S3E & Fig 2 S2B**). Dietary intake
615 was standardized 48 hours before each experimental day (41.4 kcal/kg body weight, 5.1 g/kg
616 body weight carbohydrates, 1.4 g/kg body weight protein and 1.6 g/kg body weight fat per
617 day), followed by a standardized breakfast on the morning of the experimental day (1.5 g/kg
618 bodyweight carbohydrates). Muscle biopsies of the *m. vastus lateralis* were then collected
619 after local anaesthesia (0.5 mL of 1% Xylocaïne without epinephrine) using the percutaneous
620 Bergström technique with suction[82]. The muscle samples were immediately submerged in
621 RNA*later* and stored at 4 °C until manual fiber dissection (max. 3 days).
622
623 **Single fiber isolation.** Freshly excised muscle fiber bundles were transferred to fresh RNA*later*
624 in a petri dish. Individual muscle fibers were then manually dissected using a
625 stereomicroscope and fine forceps. Twenty-five fibers were dissected per biopsy, with special
626 care to select fibers from different sections of the biopsy. After dissection, each fiber was
627 carefully submerged in 3 µL of lysis buffer (SingleShot Cell Lysis kit, Bio-rad), containing
628 proteinase K and DNase enzymes to remove unwanted proteins and DNA. Next, cell lysis and
629 protein/DNA removal was initiated by short vortexing, spinning liquid down in a
630 microcentrifuge and incubation at room temperature (10 min). Lysates were then incubated

631 for 5 min at 37 °C and 5 min at 75 °C in a thermocycler (T100, Bio-Rad), immediately followed
632 by storage at -80 °C until further processing.
633
634 **Sequencing library preparation.** Illumina-compatible libraries from polyadenylated RNA were
635 prepared from 2 µL of the muscle fiber lysates using the QuantSeq-Pool 3' mRNA-Seq library
636 prep kit (Lexogen). Detailed methodology can be found in the manufacturer guidelines. The
637 process was initiated by reverse transcription for first strand cDNA synthesis, during which
638 Unique Molecular Identifiers (UMIs) and sample-specific i1 barcodes were introduced
639 enabling sample pooling and reducing technical variability in the downstream process. Next,
640 cDNA from 96 fibers was pooled and purified using magnetic beads, followed by RNA removal
641 and second strand synthesis by random priming. Libraries were purified using magnetic beads,
642 followed by addition of pool-specific i5/i7 indices and PCR amplification. A last purification
643 step was performed, finalizing the Illumina-compatible libraries. A high sensitivity small DNA
644 Fragment Analysis kit (Agilent Technologies, DNF-477-0500) was used to assess the quality of
645 each library pool.
646
647 **Illumina sequencing.** The individual pools were further equimolarly (2 nM) pooled, based on
648 Qubit-quantified concentrations. The final pool was subsequently sequenced with a NovaSeq
649 S2 kit (1 x 100 nucleotides) with a loading of 2 nM (4% PhiX) in standard mode on a NovaSeq
650 6000 instrument.
651
652 **Primary data processing.** Our pipeline was based on the QuantSeq Pool data analysis pipeline
653 from Lexogen (https://github.com/Lexogen-Tools/quantseqpool_analysis). First, the data was
654 demultiplexed based on the i7/i5 indices with bcl2fastq2 (v2.20.0). The next demultiplexing

655 step was performed via idemux (v0.1.6) according to the i1 sample-specific barcodes in read
656 2, followed by extraction of UMI sequences with umi_tools (v1.0.1). Trimming of the reads
657 was then performed in multiple rounds with cutadapt (v3.4), with removal of too short reads
658 (length < 20) or reads consisting entirely of adapter sequences. Reads were then aligned to
659 the human genome with STAR (v2.6.0c), followed by BAM file indexing with SAMtools (v1.11).
660 Duplicates of reads were removed with umi_tools (v1.0.1). Finally, counting of the alignments
661 was performed with featureCounts from Subread (v2.0.3). At several intermediate steps
662 during the pipeline, quality control with performed with FastQC (v0.11.9).
663
664 **Initial Seurat processing.** All further bioinformatics processing and visualization was
665 performed in R (v4.2.3), primarily with the Seurat v4 workflow[83]. The individual UMI counts
666 and metadata matrices were thus transformed into a Seurat object. Genes with expression in
667 less than 30% of all fibers were removed. Low-quality samples were then removed based on
668 a minimum threshold of 1000 UMI counts and 1000 detected genes. This resulted in a total of
669 925 fibers that passed all quality control filtering steps. Normalization of UMI counts was
670 performed using the SCTransform v2 Seurat method[84], including all 7418 detected features
671 and regressing out participant variation. All relevant metadata can be found in **Table S31**.
672
673 **Proteomics**
674 **Sample collection - 1000 fiber proteome**
675 **Participant information**. Stored biobank muscle specimens were used for the purpose of the
676 present study (Clinicaltrials.gov identifier: NCT04048993). The specimens were collected from
677 five active and healthy male volunteers (aged 21-35 years) who gave their written and oral
678 informed consent with approval from the Science Ethics Committee of the Capital Region in

679 Denmark (H-1-2012-090) and complied with the guidelines of the 2013 Declaration of
680 Helsinki. General characteristics of the participants can be found in **Table S1.** Participants were
681 young, healthy (no diseases and non-smoking) and moderately physically active.
682
683 **Muscle biopsy collection.** Participants arrived in the morning after an overnight fast and
684 rested in the supine position for 1 hour. Then, local anesthesia (2-3 mL Xylocaine 2%; lidocaine
685 without epinephrine, AstraZeneca, Denmark) was applied under the skin above the fascia at
686 the belly of the *m. vastus lateralis* muscle. A muscle biopsy was sampled through a small 3-4
687 mm incision using a Bergström needle with suction. The muscle biopsy specimen was snap-
688 frozen in liquid nitrogen and stored at −80°C until analysis.
689
690 **Single muscle fiber isolation.** Muscle fibers were isolated from freeze-dried specimens as
691 previously described[24]. In brief, muscle biopsies were freeze-dried for 48 hours. Subsequently,
692 fibers were isolated in a humidity- and temperature-controlled room (humidity of 25%) using
693 fine forceps under a stereomicroscope. Approximately 200 single muscle fibers were isolated
694 for each biopsy, resulting in a total of 1038. To ensure the fibers settled at the bottom of the
695 tube, each fiber-containing tube underwent centrifugation at 20,000 g using a small
696 centrifuge. Next, fibers were resuspended in 15 µL of lysis buffer (1% sodium dodecyl sulfate
697 (SDC), 40 mM chloroacetamide (CAA), 10 mM dithiothreitol (DTT) in 50 mM Tris pH 8.5).
698
699 **Sample collection – myopathy**
700 **Participant information.** Six patients with severe nemaline myopathy were selected from our
701 nemaline myopathy study cohort. Three patients had pathogenic variants in *ACTA1*,
702 representing the conventional severe form, and three patients had pathogenic variants in

703 *TNNT1*, resulting in a rare, progressive form of nemaline myopathy. Three healthy individuals
704 with no history of neuromuscular disease were used as controls (**Table S19**).
705
706 **Muscle biopsy collection.** Healthy control participant biopsies (n = 3) were used from an
707 original study[85], and were therefore collected, snap frozen in liquid nitrogen and stored in -
708 80℃ as per that originally described. For the present study, a fragment of this stored biopsy
709 was dissected under sterile, frozen conditions before being prepared for single myofiber
710 isolation (detailed below). Acquisition of biopsies of healthy control patients was approved by
711 local ethics committee (Copenhagen and Frederiksberg) in Denmark (hs:h-15002266). Those
712 of myopathy patients were consented, stored, and used in accordance with the Human Tissue
713 Act under local ethical approval in United Kingdom (REC 13/NE/0373). All procedures were
714 carried out in accordance to the Declaration of Helsinki.
715
716 **Single fiber isolation.** Dissected fragments of muscle biopsy were placed in ice-cold, 22 micron
717 filtered relaxing solution (4 mM Mg-ATP, 1 mM free Mg^{2+}, $10^{-6.00}$ mM free Ca^{2+}, 20 mM
718 imidazole, 7 mM EGTA, 14.5 mM creatine phosphate, KCl to an iconic strength of 180 mM and
719 pH to 7.0)[86] for ~3 minutes before being immersed in fresh relaxing solution on a sterile petri
720 dish and mounted on ice under a dissection microscope for single fiber isolation. Fibers were
721 cleaved from the tissue/biopsy ensuring a variety of sample/biopsy locations were used and
722 that only single fibers were selected. Following isolation, fibers were manually moved to a
723 sterile 96-well plate containing 15 µL of lysis buffer (identical to that detailed above) where
724 the tweezers containing the fiber were submerged, spun and agitated in lysis buffer to ensure
725 the fibers dissociated from the tweezers. To ensure fibers were settled to the bottom of the
726 well, the 96-well plate was subjected to gentle vortexing and centrifugation (1,000 g).

727

728 **Proteomics analysis**

729 **Sample preparation.** Samples from both proteomics studies followed the same sample
730 preparation workflow. In order to extract the proteins, samples were boiled at 95°C in a
731 thermomixer with gentle shaking (800 rpm) and sonicated in a bioruptor instrument with 30
732 seconds on/off cycles for 15 minutes. A small 5 µL fraction of lysate from each sample was
733 saved for antibody-based fiber typing of the 1000 fiber samples. Next, samples were
734 processed following a modified version of the in-solution digestion sample preparation
735 protocol. In brief, total volume was adjusted to 50 µl by addition of digestion buffer, containing
736 50 mM Tris PH 8.5 buffer, an enzyme to protein ratio of 1:500 LysC (Wako) and a 1:100 enzyme
737 to protein ratio of trypsin (Promega). SMF lysates were digested overnight in a thermomixer
738 set to 37° C and 800 rpm. The next day, protein digestion was quenched by addition of 50 µl
739 of 2% trifluoroacetic acid (TFA) in isopropanol. Peptides were desalted using in-house
740 prepared single-use reverse-phase StageTips containing styrenedivinylbenzene reverse-phase
741 sulfonate (SDB-RPS) disks. Then, desalted peptides were loaded in Evotips (Evosep) following
742 manufacturer instructions prior LC-MS/MS analysis. Bulk tissue samples were prepared using
743 the same protocol utilized for single fibers, with a few modifications to sample lysis. Tissue
744 samples were first powdered using a tissue crusher over dry ice before resuspending the
745 powder in the same lysis buffer described above. Then, the samples were homogenized using
746 an IKA Turrax homogenizer for 2 minutes prior boiling and sonication. From here onwards the
747 samples underwent the same protocol described above.

748

749 **Proteomics library preparation.** Fibers from the five healthy control individuals participating
750 in the 1000 fiber study were carefully dissected and combined in order to create a pooled

751 fiber lysate. Then, 200 µg of protein corresponding to each participant-specific lysate were
752 pooled together into one final protein lysate that was processed following the same sample
753 preparation workflow just described. 20 µg of desalted peptides were fractionated using High
754 pH Reverse-Phase Chromatography (HpH-RP). Fractionation was carried out on a Kinetex 2.6
755 µm EVO C18 100 Å, 150 x 0.3 mm column manufactured by Phenomenex and using an EASY-
756 nLC 1200 System (Thermo) operating at 1.5 µL/min. Separation was accomplished using a 62
757 min step-gradient starting from 3% to 60% solvent B (which consisted of 10 mM TEAB in 80%
758 acetonitrile) and solvent A (containing 10 mM TEAB in water). The total run time was 98 min,
759 which included wash and column equilibration. Throughout the fractionation, peptides were
760 eluted and collected every 60 s, obtaining 96 single fractions without concatenation. Finally.
761 200 ng of HpH-RP fractionated peptides were loaded, concentrated and desalted on Evotips
762 (Evosep) following the instructions provided by the manufacturer.
763
764 **Liquid chromatography tandem mass spectrometry**. Proteomics measurements were
765 performed using LC-MS instrumentation consisting of an Evosep One HPLC system (Evosep)[22]
766 coupled via electrospray ionization to a timsTOF SCP mass spectrometer (Bruker). Peptides
767 were separated utilizing 8 cm, 150 µM ID columns packed with C18 beads (1.5 µm) (Evosep).
768 Chromatographic separation was achieved by the '60 samples per day' method, followed by
769 electrospray ionization through a CaptiveSpray ion source and a 10 µm emitter into the MS
770 instrument. Single muscle fiber peptides were measured in DIA-PASEF mode following a
771 previously described method[23], while library fractions were measured using DDA-PASEF. In
772 brief, the DDA-PASEF scan range encompassed 100 - 1700 m/z for both MS and MS/MS, and
773 TIMS mobility range was set to 0.6 – 1.6 (V cm^{-2}). Both TIMS ramp and accumulation times
774 were configured to 100 ms, and 10 PASEF ramps were recorded for a total cycle time of 1.17

775 s. The MS/MS target intensity and intensity threshold were defined as 20.000 and 1.000,
776 respectively. An exclusion list of 0.4 min for precursors within 0.015 m/z and 0.015 V cm^{-2}
777 width was also activated. For DIA-PASEF the scan range was established at 400-1000 (m/z),
778 the TIMS mobility range to 0.64-1.37 (V cm^{-2}), and ramp and accumulation times were both
779 set to 100 ms. A short-gradient method was used, which included 8 DIA-PASEF scans with
780 three 25 Da windows per ramp, resulting in an estimated cycle time of 0.95 sec.
781
782 **MS data processing**. Library files were processed using the MS-Fragger functionality within
783 Fragpipe v19.0 under the SpecLib workflow with default settings, including a minimum
784 peptide length of seven amino acids and maximum of two missed cleavages allowed[87]. Spectra
785 were searched against a human reviewed FASTA from Uniprot (March 2022, 20410 entries)
786 and the output library contained a total of 5350 protein groups and 84383 precursors. Sample
787 raw MS files were analyzed using DIA-NN version 1.8[88] in a library-based manner against the
788 MS library just described. Protein groups quantification was based on proteotypic peptides,
789 neural network was set to double-pass mode, quantification strategy was set to "Robust LC
790 (high accuracy)" and the match between runs options was enabled, the rest of parameters
791 remained as default, which included precursor FDR set to 1% and peptide length of 7-30 amino
792 acids.
793
794 **Data processing**. Further data analysis was performed under the R environment (R version
795 4.22). Both a metadata data frame containing sample and participant information and the
796 "PG_matrix.tsv" file from DIA-NN's output were loaded in RStudio. The 1000 fiber data frame
797 was filtered to remove samples with less than 50% valid protein intensity values, resulting in
798 a total of 974 fibers. Next, rows were filtered to remove proteins with less than 30% valid

799 values across samples, resulting in a total of 1685 proteins. Regarding the myopathy dataset,
800 after filtering samples for 50% valid values, the number of samples was 250. We included in
801 the analysis proteins that were quantified in 70% of the samples in at least one condition
802 (conditions: control, actin myopathy and troponin myopathy), resulting in a total of 1545
803 proteins. Both data frames were then log2 transformed and normalized using the
804 *normalizeBetweenArrays()* function from the limma package, with the method argument set
805 to quantile[89]. Then, batch correction through the *ComBat()* function from the sva package[90]
806 was applied to minimize the effect of the three technical batches originated during mass
807 spectrometry measurement. Finally, missing values were replaced by random numbers from
808 a Gaussian distribution with the default settings of the *tImpute()* function from the PhosR
809 package[91]. All relevant metadata for the 1000 fiber proteome and nemaline myopathy
810 datasets can be found in **Tables S32 and S33, respectively**.
811
812 **Bioinformatics analysis**
813 **Transcriptome and proteome dynamic range.** The expression/intensity for each gene/protein
814 was calculated relative to the total counts/intensity for each fiber. This value was then
815 averaged across fibers in each dataset and log10-transformed. The overlap of detected
816 features between both datasets were analyzed using the *VennDiagram* package (v 1.7.3).
817
818 **Coefficient of variation – proteomics.** For each of the 96 well plates used during the MS
819 measurement of the 1000 fiber study, one technical control sample was included in A1
820 position to monitor total ion current intensity and quality control of the runs (a total of eleven
821 technical controls). The coefficient of variation between proteins was calculated by dividing

822 the standard deviation by the mean of the LFQ intensities from each protein across technical
823 replicates and then multiplied by one hundred.
824
825 **Correlation analyses.** Mean log2 transformed transcript counts, protein intensities, and/or
826 fold change values across fibers were calculated, filtered for shared proteins/genes and
827 Pearson correlation was calculated.
828
829 **Omics-based fiber typing.** Normalized counts and raw LFQ intensities were retrieved from
830 well-described contractile proteins that have a slow (MYH7, TNNT1, TPM3, ATP2A2 and MYL3)
831 and fast (MYH2, MYH1, TNNT3, TPM1, ATP2A1 and MYL1) isoform[2]. For each isoform
832 combination, the relative expression of each was then calculated and samples were ordered
833 from high to low. The mathematical bottom knee for each curve was then determined using
834 the *barcodeRanks()* function in the DropletUtils package (v 1.18.1). This threshold was used
835 to assign fiber types as pure (type 1, type 2A or type 2X) or hybrid (hybrid 1/2A, hybrid 2A/2X
836 or hybrid 1/2X) (**Table S6**). For the features with only two isoforms, fibers were assigned as
837 'slow', 'fast' or 'hybrid'. To determine the overlap of the contractile features assigning a fiber
838 as being slow, upset plots were generated using the *upset()* function of the ComplexUpset
839 package (v 1.3.3), and then simplified to bar plots.
840
841 **Principal Component Analysis (PCA).** PCA was performed using the *RunPCA()* function of the
842 Seurat package. Scree plots were based on the *fviz_eig()* function of the factoextra package (v
843 1.0.7), which worked after PCA with *prcomp()*.
844

845 **Seurat clustering.** Uniform Manifold Approximation and Projection (UMAP) clustering was
846 performed based on the K-nearest neighbor graph with the first 6 dimensions as input for
847 both the transcriptome and proteome datasets (**Fig 1 S3D-E**). Feature plots were generated
848 using the *FeaturePlot()* function. UMAP plots were colored based on different criteria (MYH-
849 based fiber types, participant, test day) stored in the metadata.
850
851 **Enrichment analysis.** Genes and protein sets were processed to obtain lists of features that
852 were differentially expressed or, in the case of the top PCA drivers, in the top 5% drivers for
853 the positive and negative direction of the first and second principal component. Over-
854 representation analysis was then performed on these features with the *enrichGO()* and
855 *simplify()* function of the clusterProfiler package (v 4.6.2)[92] using all gene ontology terms.
856 Obtained lists of significant terms were manually curated to extract interesting and relevant
857 terms.
858
859 **Hierarchical clustering of ribosomal proteins.** Raw proteomics data was log2 transformed and
860 filtered to contain proteins enlisted in the 'cytosolic ribosome' GO term, followed by Z-scoring
861 prior heatmap visualization using the *pheatmap()* function from the Pheatmap package (v
862 1.0.12). The number of clusters was determined by visual inspection and assigning a value of
863 3 to the *cuttree*() function.
864
865 **Differential expression analysis**. To avoid artificially inflated p-values, which would arise from
866 regarding every fiber as an independent replicate, we employed a pseudobulk differential
867 expression analysis approach. We mathematically downsampled the total data points to one
868 value per MYH-based fiber type per participant by aggregating (transcriptomics) or taking the

869 median value (proteomics). Transcriptomics data were further processed using the DESeq2
870 pipeline (v 1.38.3)[93] with a '~ participant + fiber type' statistical model. 1000 fiber proteomics
871 data was processed using the limma (v 3.54.2) workflow, fitting the data to a linear model
872 defined as: '~ 0 + fiber type + participant', whereas the myopathy dataset was fitted to '~ 0 +
873 condition' for the comparisons between conditions and '~ 0 + fiber type and condition' for the
874 comparisons including fiber type. Fitted models were then subjected to gene ranking using an
875 empirical Bayes method using *eBayes*() prior extracting the results through *topTable*(), with p-
876 value adjustment set to Benjamini-Hochberg, both functions from the limma package.
877 Threshold for significantly different genes/proteins was defined as adjusted p-values smaller
878 than 0.05 and a log fold change cut-off of 1 was applied. For the nemaline myopathy dataset,
879 the Xiao significance score was applied, which combines expression fold change and statistical
880 significance[94]. Proteins with a Xiao score under 0.05 were regarded as differentially expressed
881 between conditions.
882
883 **SCENIC.** Inference of active transcription factors in slow and fast fibers was performed using
884 Single-Cell rEgulatory Network Inference and Clustering (SCENIC, pySCENIC version 0.12.1
885 with cisTarget v10 databases and annotations)[95]. To prioritize fiber-type specific transcription
886 factors, both their fiber-type specific expression at mRNA level and regulon activity were
887 combined into a final prioritization score. This prioritization score was calculated as the sum
888 of the z-score scaled differential expression score (logFC from pseudobulked data) and z-score
889 scaled regulon specificity scores (RSS).
890
891 **Non-coding RNA**. For the transcriptomics data, the biotype of each gene was determined
892 using the 'GENEBIOTYPE' column using the AnnotationDbi package (v 1.60.2) with the

893 EnsDb.Hsapiens.v86 database. Genomic location interrogation was performed using the UCSC
894 Human Genome Browser (https://genome.ucsc.edu). Tissue-specific gene expression of
895 interesting long non-coding RNAs was explored using the GTEx Portal database.
896
897 **Microprotein identification**.
898 *Construction of putative lncRNA-encoded protein database*
899 RNA sequences of the non-coding transcripts were extracted using the *getSequence() function*
900 *from the biomaRt package* (v 2.56.1)*,* with 'transcript_exon_intron' as the *seqType.* Both
901 intergenic (lincRNA) and antisense long non-coding RNA (lncRNA) transcripts were utilized for
902 database construction. A six-frame-translation was used to translate the corresponding RNA
903 sequences into the proteins, as well as ORFfinder NCBI functionality
904 (https://www.ncbi.nlm.nih.gov/orffinder/) was used to extract open reading frames (ORFs)
905 from the transcripts. Minimal ORF length was set to 75 nucleotides, genetic code was set to
906 "Standard" and "Any sense codon" was used, as a start codon, to extract maximum number
907 of open reading frames. The obtained protein fasta file contained multiple entries for each
908 gene name, ensured by various combinations of: i) transcript identifiers, ii) ORF identifiers and
909 iii) start:stop codons.
910
911 *Identification of lncRNA-encoded proteins*
912 DIA raw MS data were analyzed with Spectronaut v18 using an in-house generated sample-
913 specific fasta, comprised of the reviewed human proteome (proteome ID: UP000005640, 20
914 426 proteins, downloaded Sep 2023) and lncRNA-encoded protein sequences (125 223
915 proteins), in directDIA mode. The default settings were used unless otherwise noted. Data
916 filtering was set to "Qvalue". False discovery rate (FDR) was set to 1% at

917 peptide precursor level and 1% at protein level. Top3 peptide precursors were used for protein
918 quantification. The downstream data analysis was performed using in-house developed R
919 script.
920
921 **PCA projection**. The 1000 fiber and myopathy data sets were initially filtered to remove non-
922 overlapping proteins. Then, they were combined and normalized using the
923 *normalizeBetweenArrays()* function from the limma package. The normalization method used
924 was "quantile" to ensure that both data sets had the same distributions and were comparable.
925 Subsequently, the merged data set was divided back into the two separate data sets, namely
926 the 1000 fiber data set and the myopathy data set. For the 1000 fiber data set, PCA was
927 calculated using the *prcomp()* function. Moving on, the myopathy data set was multiplied by
928 the PC loadings obtained from the 1000 fiber dataset to generate its PCA projection. Finally,
929 the PCA projections from the myopathy samples were plotted on the top of the 1000 fiber
930 PCA visualization.
931
932 **Muscle-specific ribosomal gene signature**
933 The skeletal muscle-specific ribosomal gene signature, consisting of log2 fold change values
934 comparing the mRNA expression of ribosomal subunits in skeletal muscle compared to 52
935 other human tissues, was downloaded from Panda et al[96]. Log2 fold change values were
936 ranked to identify ribosomal proteins with the highest overexpression in human skeletal
937 muscle.
938
939 **Structural Analysis of Ribosomal Proteins**

940 The human 80S ribosome structural model (Protein Data Bank: 4V6X) was downloaded from
941 the Protein Data Bank website (RCSB PDB). Visualization and editing of the ribosomal
942 structure, and preparation of figures and movies were performed in UCSF ChimeraX[97].
943
944 **Antibody-based fiber typing**
945 Dot blot was conducted following a previously described protocol with a few modifications[24].
946 Initially, two identical PVDF membranes were activated using 96% ethanol and washed with
947 transfer buffer. Subsequently, the membranes were placed on wet filter paper with transfer
948 buffer until they dried. Next, 1 µL of fiber lysate was spotted at the same position on both
949 membranes, and the membranes were allowed to dry. Reactivation of the membranes was
950 carried out using 96% ethanol, followed by gentle washing with TBST. The membranes were
951 then blocked in TBST containing 5% skim milk for 15 minutes. After blocking, the membranes
952 were washed three times with TBST and incubated with the primary antibody solution of
953 either anti-MYH7 (A4.840) or anti-MYH2 (A4.74), both from Developmental Studies
954 Hybridoma Bank (DSHB) at a dilution of 1:200 in TBST containing 1% skim milk for one hour.
955 Subsequently, the membranes were gently washed three times with TBST and incubated with
956 the secondary antibody (anti-mouse) at a dilution of 1:20,000 in TBST containing 1% skim milk
957 for two hours. Finally, the membranes were washed three times for five minutes each with
958 TBST and visualized using Immobilon Forte (Milipore) in a ChemiDoc XRS+ (Bio-Rad) imaging
959 system.
960
961 **RNAscope**.
962 8µm sections from three different fixed-frozen human muscle biopsies were used for
963 RNAscope labelling and subsequent immunohistochemistry (IHC). For detection of RP11-

964 255P5.3 and LINC01405 commercially available RNAscope Multiplex Fluorescent Assay V2
965 (Advanced Cell Diagnostics) and probes against Lnc-ERCC5-5-C1 (# 1276851-C1), and
966 LINC01405-C2 (# 549201-C2) (Advanced Cell Diagnostics), were used according to the
967 manufacturer's protocols. To control tissue quality Positive 3-plex probe (# 320881) and
968 negative 3-plex probe (# 320871) were used. To visualize different subtypes of muscle fibers,
969 sections after RNAscope were blocked with 5% donkey serum and incubated with antibodies
970 against MYH2 (A4.74-s (1:5); DSHB) and MYH7 (A4.840 (1:5); BSHD) overnight. After washing
971 sections were incubated with Alexa Flour 488-conjugated Donkey Anti-Mouse IgG, Fcγ
972 Subclass 1 and DyLightTM405-conjugated Donkey Anti-Mouse IgM secondary antibodies
973 respectively and mounted with ProLong™ Diamond Antifade Mountant (Invitrogen). Slides
974 were imaged using Zeiss Axio Observer microscope equipped with Axiocam 702 camera.
975 Biopsies from three individuals were used for quantification, with 187 muscle fibers being
976 counted in total. As in RNAscope each dot corresponds to one RNA molecule, the number of
977 dots/mm^2 was used as a measure of RNA expression. We first determined the number of
978 dots/mm^2 within each fiber for both probes, then averaged the results by fiber type and
979 participant. The given average was then used as an input for a two sample t-test.
980
981 **Immunostaining for muscle sections**
982 Immunolabelling was performed on 10 µm cryosections, fixed in 4% PFA (10 min),
983 permeabilized in 0.1% Triton X-100 (20 min) and blocked in 10% Normal Goat Serum (50062Z,
984 Life Technologies) with 0.1% BSA (1 h). Sections were incubated o/n (4°C) with primary
985 antibodies against MYH7 (mouse monoclonal A4.951, Santa Cruz, sc-53090, diluted 1:25) or
986 MYH2 (mouse monoclonal SC71, DSHB, 1:25), each combined with primary antibody against
987 TNNT1 (rabbit polyclonal HPA058448, Sigma, diluted 1:500) in 5% goat serum with 0.1% BSA

988 and 0.1% Triton X-100. Alexa Fluor Goat anti-Mouse 647 (A21237) was used as the secondary
989 antibody for the MYHs and Alexa Fluor Donkey anti-Rabbit 488 (A11034) for the TNNT1 (Life
990 Technologies, 1:500 each in 10% Normal Goat Serum). Fluorescent images were obtained with
991 a 10x objective on a Zeiss Axio Observer 3 fluorescence microscope with a Colibri 5 led
992 detector, combined with Zeiss Axiocam 705 mono camera, using Zen software (Zeiss). For
993 visualization purposes, a selection of fibres were mounted on copper grids glued on a
994 microscopy slide, and imaged under a stereomicroscope.
995
996 **References**

997 1 Altschuler, S. J. & Wu, L. F. Cellular heterogeneity: do differences make a difference?
998 *Cell* **141**, 559-563 (2010).
999 2 Schiaffino, S. & Reggiani, C. Fiber types in mammalian skeletal muscles. *Physiol Rev*
1000 **91**, 1447-1531 (2011).
1001 3 Engel, W. K. The essentiality of histo- and cytochemical studies of skeletal muscle in
1002 the investigation of neuromuscular disease. 1962. *Neurology* **12**, 778-784 (1962).
1003 4 Brooke, M. H. & Kaiser, K. K. Three "myosin adenosine triphosphatase" systems: the
1004 nature of their pH lability and sulfhydryl dependence. *J Histochem Cytochem* **18**, 670-
1005 672 (1970).
1006 5 Biral, D., Betto, R., Danieli-Betto, D. & Salviati, G. Myosin heavy chain composition of
1007 single fibres from normal human muscle. *Biochem J* **250**, 307-308 (1988).
1008 6 Blemker, S. S., Brooks, S. V., Esser, K. A. & Saul, K. R. Fiber-type traps: revisiting
1009 common misconceptions about skeletal muscle fiber types with application to motor
1010 control, biomechanics, physiology, and biology. *J Appl Physiol (1985)* **136**, 109-121
1011 (2024).

1012 7 Johnson, M. A., Polgar, J., Weightman, D. & Appleton, D. Data on the distribution of
1013 fibre types in thirty-six human muscles. An autopsy study. *J Neurol Sci* **18**, 111-129
1014 (1973).
1015 8 Tang, F. *et al.* mRNA-Seq whole-transcriptome analysis of a single cell. *Nat Methods*
1016 **6**, 377-382 (2009).
1017 9 Islam, S. *et al.* Characterization of the single-cell transcriptional landscape by highly
1018 multiplex RNA-seq. *Genome Res* **21**, 1160-1167 (2011).
1019 10 Brunner, A.-D. *et al.* Ultra-high sensitivity mass spectrometry quantifies single-cell
1020 proteome changes upon perturbation. *Mol Syst Biol* **18**, e10798 (2022).
1021 11 Murgia, M. *et al.* Single muscle fiber proteomics reveals fiber-type-specific features
1022 of human muscle aging. *Cell Rep* **19**, 2396-2409 (2017).
1023 12 Murgia, M. *et al.* Signatures of muscle disuse in spaceflight and bed rest revealed by
1024 single muscle fiber proteomics. *PNAS Nexus* **1**, pgac086 (2022).
1025 13 Murgia, M. *et al.* Single muscle fiber proteomics reveals unexpected mitochondrial
1026 specialization. *EMBO rep* **16**, 387-395 (2015).
1027 14 Murgia, M. *et al.* Protein profile of fiber types in human skeletal muscle: a single-fiber
1028 proteomics study. *Skeletal Muscle* **11**, 24 (2021).
1029 15 Lang, F. *et al.* Single muscle fiber proteomics reveals distinct protein changes in slow
1030 and fast fibers during muscle atrophy. *J Proteome Res* **17**, 3333-3347 (2018).
1031 16 Momenzadeh, A. *et al.* A complete workflow for high throughput human single
1032 skeletal muscle fiber proteomics. *J Am Soc Mass Spectrom* (2023).
1033 17 Chemello, F. *et al.* Degenerative and regenerative pathways underlying Duchenne
1034 muscular dystrophy revealed by single-nucleus RNA sequencing. *Proc Natl Acad Sci*
1035 *USA* **117**, 29691-29701 (2020).

1036 18 Lin, H. *et al.* Decoding the transcriptome of denervated muscle at single-nucleus
1037 resolution. *J Cachexia Sarcopenia Muscle* **13**, 2102-2117 (2022).
1038 19 Sewry, C. A., Laitila, J. M. & Wallgren-Pettersson, C. Nemaline myopathies: a current
1039 view. *J Muscle Res Cell Motil* **40**, 111-126 (2019).
1040 20 Laitila, J. & Wallgren-Pettersson, C. Recent advances in nemaline myopathy.
1041 *Neuromuscul Disord* **31**, 955-967 (2021).
1042 21 Zhang, M. J., Ntranos, V. & Tse, D. Determining sequencing depth in a single-cell RNA-
1043 seq experiment. *Nat Commun* **11**, 774 (2020).
1044 22 Bache, N. *et al.* A novel LC system embeds analytes in pre-formed gradients for rapid,
1045 ultra-robust proteomics. *Mol Cell Proteomics* **17**, 2284-2296 (2018).
1046 23 Meier, F. *et al.* diaPASEF: parallel accumulation–serial fragmentation combined with
1047 data-independent acquisition. *Nat Methods* **17**, 1229-1236 (2020).
1048 24 Deshmukh, A. S. *et al.* Deep muscle-proteomic analysis of freeze-dried human muscle
1049 biopsies reveals fiber type-specific adaptations to exercise training. *Nat Commun* **12**,
1050 304 (2021).
1051 25 Pardo, J. V., Siliciano, J. D. & Craig, S. W. A vinculin-containing cortical lattice in
1052 skeletal muscle: transverse lattice elements ("costameres") mark sites of attachment
1053 between myofibrils and sarcolemma. *Proc Natl Acad Sci USA* **80**, 1008-1012 (1983).
1054 26 Xiao, Y. *et al.* Loss of mitochondrial protein CHCHD10 in skeletal muscle causes
1055 neuromuscular junction impairment. *Hum Mol Genet* **29**, 1784-1796 (2020).
1056 27 Cho, H. J. *et al.* SLIT3 promotes myogenic differentiation as a novel therapeutic factor
1057 against muscle loss. *J Cachexia Sarcopenia Muscle* **12**, 1724-1740 (2021).

1058 28 Han, S. *et al.* Nuclear envelope phosphatase 1-regulatory subunit 1 (formerly
1059 TMEM188) is the metazoan Spo7p ortholog and functions in the lipin activation
1060 pathway. *J Biol Chem* **287**, 3123-3137 (2012).
1061 29 Hengel, H. *et al.* Loss-of-function mutations in UDP-Glucose 6-Dehydrogenase cause
1062 recessive developmental epileptic encephalopathy. *Nat Commun* **11**, 595 (2020).
1063 30 Farhang-Fallah, J. *et al.* The pleckstrin homology (PH) domain-interacting protein
1064 couples the insulin receptor substrate 1 PH domain to insulin signaling pathways
1065 leading to mitogenesis and GLUT4 translocation. *Mol Cell Biol* **22**, 7325-7336 (2002).
1066 31 Genuth, N. R. & Barna, M. The discovery of ribosome heterogeneity and its
1067 implications for gene regulation and organismal life. *Mol Cell* **71**, 364-374 (2018).
1068 32 Parks, M. M. *et al.* Variant ribosomal RNA alleles are conserved and exhibit tissue-
1069 specific expression. *Sci Adv* **4**, eaao0665 (2018).
1070 33 Slavov, N., Semrau, S., Airoldi, E., Budnik, B. & van Oudenaarden, A. Differential
1071 stoichiometry among core ribosomal proteins. *Cell Rep* **13**, 865-873 (2015).
1072 34 Shi, Z. *et al.* Heterogeneous ribosomes preferentially translate distinct subpools of
1073 mRNAs genome-wide. *Mol Cell* **67**, 71-83.e77 (2017).
1074 35 Kondrashov, N. *et al.* Ribosome-mediated specificity in Hox mRNA translation and
1075 vertebrate tissue patterning. *Cell* **145**, 383-397 (2011).
1076 36 Genuth, N. R. *et al.* A stem cell roadmap of ribosome heterogeneity reveals a
1077 function for RPL10A in mesoderm production. *Nat Commun* **13**, 5491 (2022).
1078 37 Landry, D. M., Hertz, M. I. & Thompson, S. R. RPS25 is essential for translation
1079 initiation by the Dicistroviridae and hepatitis C viral IRESs. *Genes Dev* **23**, 2753-2764
1080 (2009).

1081 38 Horos, R. *et al.* Ribosomal deficiencies in Diamond-Blackfan anemia impair
1082 translation of transcripts essential for differentiation of murine and human
1083 erythroblasts. *Blood* **119**, 262-272 (2012).
1084 39 Anger, A. M. *et al.* Structures of the human and Drosophila 80S ribosome. *Nature*
1085 **497**, 80-85 (2013).
1086 40 Spahn, C. M. *et al.* Cryo-EM visualization of a viral internal ribosome entry site bound
1087 to human ribosomes: the IRES functions as an RNA-based translation factor. *Cell* **118**,
1088 465-475 (2004).
1089 41 Boehringer, D., Thermann, R., Ostareck-Lederer, A., Lewis, J. D. & Stark, H. Structure
1090 of the hepatitis C virus IRES bound to the human 80S ribosome: Remodeling of the
1091 HCV IRES. *Structure* **13**, 1695-1706 (2005).
1092 42 Kannan, K., Vázquez-Laslop, N. & Mankin, A. S. Selective protein synthesis by
1093 ribosomes with a drug-obstructed exit tunnel. *Cell* **151**, 508-520 (2012).
1094 43 Armstrong, E. *et al.* Comparison of transcriptomic landscapes of different lamb
1095 muscles using RNA-Seq. *PLoS One* **13**, e0200732 (2018).
1096 44 Nelson, B. R. *et al.* A peptide encoded by a transcript annotated as long noncoding
1097 RNA enhances SERCA activity in muscle. *Science* **351**, 271-275 (2016).
1098 45 Leberer, E. & Pette, D. Lactate dehydrogenase isozymes in type I, IIA and IIB fibres of
1099 rabbit skeletal muscles. *Histochemistry* **80**, 295-298 (1984).
1100 46 Rubenstein, A. B. *et al.* Single-cell transcriptional profiles in human skeletal muscle.
1101 *Sci Rep* **10**, 229 (2020).
1102 47 Lerín, C. *et al.* Regulation and function of the muscle glycogen-targeting subunit of
1103 protein phosphatase 1 (GM) in human muscle cells depends on the COOH-terminal
1104 region and glycogen content. *Diabetes* **52**, 2221-2226 (2003).

1105 48 Luo, Y., Na, Z. & Slavoff, S. A. P-bodies: Composition, properties, and functions.
1106 *Biochemistry* **57**, 2424-2431 (2018).
1107 49 Aibar, S. *et al.* SCENIC: single-cell regulatory network inference and clustering. *Nat*
1108 *Methods* **14**, 1083-1086 (2017).
1109 50 Sadaki, S. *et al.* Large Maf transcription factor family is a major regulator of fast type
1110 IIb myofiber determination. *Cell Rep* **42**, 112289 (2023).
1111 51 Statello, L., Guo, C.-J., Chen, L.-L. & Huarte, M. Gene regulation by long non-coding
1112 RNAs and its biological functions. *Nat Rev Mol Cell Biol* **22**, 96-118 (2021).
1113 52 Lorenzi, L. *et al.* The RNA Atlas expands the catalog of human non-coding RNAs. *Nat*
1114 *Biotech* **39**, 1453-1465 (2021).
1115 53 Wang, W. *et al.* Identification of miRNA, lncRNA and mRNA-associated ceRNA
1116 networks and potential biomarker for MELAS with mitochondrial DNA A3243G
1117 mutation. *Sci Rep* **7**, 41639 (2017).
1118 54 Volders, P.-J. *et al.* LNCipedia 5: towards a reference set of human long non-coding
1119 RNAs. *Nucleic Acids Res* **47**, D135-D139 (2019).
1120 55 Matsumoto, A. *et al.* mTORC1 and muscle regeneration are regulated by the
1121 LINC00961-encoded SPAR polypeptide. *Nature* **541**, 228-232 (2017).
1122 56 Jeong, O. S. *et al.* Long noncoding RNA linc00598 regulates CCND2 transcription and
1123 modulates the G1 checkpoint. *Sci Rep* **6**, 32172 (2016).
1124 57 Bittel, D. C. *et al.* Annexin A2 mediates dysferlin accumulation and muscle cell
1125 membrane repair. *Cells* **9** (2020).
1126 58 Carmeille, R. *et al.* Membrane repair of human skeletal muscle cells requires
1127 Annexin-A5. *Biochim Biophys Acta* **1863**, 2267-2279 (2016).

1128 59 Jaiswal, J. K. *et al.* S100A11 is required for efficient plasma membrane repair and
1129 survival of invasive cancer cells. *Nat Commun* **5**, 3795 (2014).
1130 60 Cagliani, R. *et al.* Mutation finding in patients with dysferlin deficiency and role of the
1131 dysferlin interacting proteins annexin A1 and A2 in muscular dystrophies. *Hum Mutat*
1132 **26**, 283 (2005).
1133 61 Leikina, E. *et al.* Extracellular annexins and dynamin are important for sequential
1134 steps in myoblast fusion. *J Cell Biol* **200**, 109-123 (2012).
1135 62 Zhu, B. *et al.* Monoubiquitination of human histone H2B: the factors involved and
1136 their roles in HOX gene regulation. *Mol Cell* **20**, 601-611 (2005).
1137 63 Needham, D. M. Red and white muscle. *Physiol Revs* **6**, 1-27 (1926).
1138 64 Petrany, M. J. *et al.* Single-nucleus RNA-seq identifies transcriptional heterogeneity in
1139 multinucleated skeletal myofibers. *Nat Commun* **11**, 6374 (2020).
1140 65 Reisman, E. G. *et al.* Fibre-specific mitochondrial protein abundance is linked to
1141 resting and post-training mitochondrial content in the muscle of men. *Nat Commun*
1142 **15**, 7677 (2024).
1143 66 Murach, K. A. *et al.* Fiber typing human skeletal muscle with fluorescent
1144 immunohistochemistry. *Journal of Applied Physiology* **127**, 1632-1639 (2019).
1145 67 Perrin, L. *et al.* Transcriptomic analyses reveal rhythmic and CLOCK-driven pathways
1146 in human skeletal muscle. *Elife* **7** (2018).
1147 68 Soule, T. G. *et al.* A protocol for single nucleus RNA-seq from frozen skeletal muscle.
1148 *Life Sci Alliance* **6** (2023).
1149 69 Kedlian, V. R. *et al.* Human skeletal muscle aging atlas. *Nature Aging* **4**, 727-744
1150 (2024).

1151 70 Pass, C. G. *et al.* Single-Nuclei RNA-Sequencing of the Gastrocnemius Muscle in
1152 Peripheral Artery Disease. *Circulation Research* **133**, 791-809 (2023).
1153 71 Karlsen, A. *et al.* Distinct myofibre domains of the human myotendinous junction
1154 revealed by single-nucleus RNA sequencing. *J Cell Sci* **136** (2023).
1155 72 Robinson, M. M. *et al.* Enhanced protein translation underlies improved metabolic
1156 and physical adaptations to different exercise training modes in young and old
1157 humans. *Cell Metab* **25**, 581-592 (2017).
1158 73 D'Ercole, C. *et al.* Spatially resolved transcriptomics reveals innervation-responsive
1159 functional clusters in skeletal muscle. *Cell Rep* **41**, 111861 (2022).
1160 74 Fitzgerald, G. *et al.* MME+ fibro-adipogenic progenitors are the dominant adipogenic
1161 population during fatty infiltration in human skeletal muscle. *Commun Biol* **6**, 111
1162 (2023).
1163 75 Babaeijandaghi, F. *et al.* Metabolic reprogramming of skeletal muscle by resident
1164 macrophages points to CSF1R inhibitors as muscular dystrophy therapeutics. *Sci*
1165 *Trans Med* **14**, eabg7504 (2022).
1166 76 Chaillou, T., Zhang, X. & McCarthy, J. J. Expression of Muscle-Specific Ribosomal
1167 Protein L3-Like Impairs Myotube Growth. *J Cell Physiol* **231**, 1894-1902 (2016).
1168 77 Cui, M. *et al.* The rRNA epitranscriptome and myonuclear SNORD landscape in
1169 skeletal muscle fibers contributes to ribosome heterogeneity and is altered by a
1170 hypertrophic stimulus. *American Journal of Physiology-Cell Physiology* **327**, C516-
1171 C524 (2024).
1172 78 Seaborne, R. A. E. & Ochala, J. The dawn of the functional genomics era in muscle
1173 physiology. *J Physiol* **601**, 1343-1352 (2023).

1174 79 Trappe, S. *et al.* Skeletal muscle signature of a champion sprint runner. *J Appl Physiol*
1175 *(1985)* **118**, 1460-1466 (2015).
1176 80 Andersen, J. L., Mohr, T., Biering-Sørensen, F., Galbo, H. & Kjaer, M. Myosin heavy
1177 chain isoform transformation in single fibres from m. vastus lateralis in spinal cord
1178 injured individuals: effects of long-term functional electrical stimulation (FES).
1179 *Pflugers Arch* **431**, 513-518 (1996).
1180 81 Van der Stede, T. *et al.* Histamine H(1) and H(2) receptors are essential transducers of
1181 the integrative exercise training response in humans. *Sci Adv* **7** (2021).
1182 82 Bergström, J. Percutaneous needle biopsy of skeletal muscle in physiological and
1183 clinical research. *Scand J Clin Lab Invest* **35**, 609-616 (1975).
1184 83 Hao, Y. *et al.* Integrated analysis of multimodal single-cell data. *Cell* **184**, 3573-
1185 3587.e3529 (2021).
1186 84 Choudhary, S. & Satija, R. Comparison and evaluation of statistical error models for
1187 scRNA-seq. *Genome Biol* **23**, 27 (2022).
1188 85 Sahl, R. E. *et al.* Variation in mitochondrial respiratory capacity and myosin heavy
1189 chain composition in repeated muscle biopsies. *Anal Biochem* **556**, 119-124 (2018).
1190 86 Ranu, N. *et al.* NEB mutations disrupt the super-relaxed state of myosin and remodel
1191 the muscle metabolic proteome in nemaline myopathy. *Acta Neuropathol Commun*
1192 **10**, 185 (2022).
1193 87 Demichev, V. *et al.* dia-PASEF data analysis using FragPipe and DIA-NN for deep
1194 proteomics of low sample amounts. *Nat Commun* **13**, 3944 (2022).
1195 88 Demichev, V., Messner, C. B., Vernardis, S. I., Lilley, K. S. & Ralser, M. DIA-NN: neural
1196 networks and interference correction enable deep proteome coverage in high
1197 throughput. *Nat Methods* **17**, 41-44 (2020).

1198 89 Ritchie, M. E. *et al.* LIMMA powers differential expression analyses for RNA-
1199 sequencing and microarray studies. *Nucleic Acids Res* **43**, e47 (2015).
1200 90 Müller, C. *et al.* Removing batch effects from longitudinal gene expression - Quantile
1201 normalization plus ComBat as best approach for microarray transcriptome data. *PLoS*
1202 *One* **11**, e0156594 (2016).
1203 91 Kim, H. J. *et al.* PhosR enables processing and functional analysis of
1204 phosphoproteomic data. *Cell Rep* **34**, 108771 (2021).
1205 92 Wu, T. *et al.* clusterProfiler 4.0: A universal enrichment tool for interpreting omics
1206 data. *Innovation (Camb)* **2**, 100141 (2021).
1207 93 Love, M. I., Huber, W. & Anders, S. Moderated estimation of fold change and
1208 dispersion for RNA-seq data with DESeq2. *Genome Biol* **15**, 550 (2014).
1209 94 Xiao, Y. *et al.* A novel significance score for gene selection and ranking. *Bioinformatics*
1210 **30**, 801-807 (2014).
1211 95 Van de Sande, B. *et al.* A scalable SCENIC workflow for single-cell gene regulatory
1212 network analysis. *Nat Protoc* **15**, 2247-2276 (2020).
1213 96 Panda, A. *et al.* Tissue- and development-stage–specific mRNA and heterogeneous
1214 CNV signatures of human ribosomal proteins in normal and cancer samples. *Nucleic*
1215 *Acids Res* **48**, 7079-7098 (2020).
1216 97 Pettersen, E. F. *et al.* UCSF ChimeraX: Structure visualization for researchers,
1217 educators, and developers. *Protein Sci* **30**, 70-82 (2021).
1218

1219 **Data availability**

1220 RNA-seq data has been deposited at the European Genome-phenome Archive (EGA), which is
1221 hosted by the EBI and the CRG, under study ID EGAS50000000418. Raw mass spectrometry

files and search engine results have been deposited at the ProteomeXchange Consortium through the PRIDE partner repository (identifier PXD046863).

Code availability

All code used for this manuscript is available upon request.

Acknowledgments

This work is supported by an unconditional donation from the Novo Nordisk Foundation (NNF) to NNF Center for Basic Metabolic Research (Grant numbers NNF18CC0034900 and NNF23SA0084103). Mass spectrometry analyses were performed by the Proteomics Research Infrastructure (PRI) at the University of Copenhagen (UCPH), supported by the Novo Nordisk Foundation (NNF) (grant agreement number NNF19SA0059305). This work was generously funded by grants from the Novo Nordisk Foundation (NNF-0070539; to JO), the Foundation Building Strength for Nemaline Myopathy (to JO) and the Research Foundation Flanders (G080321N, 11B4220N and 1268023N; to WD, TVdS and EL, respectively). Several plots were made with BioRender.com. The authors would like to thank Alberto Santos, Leonidas Lundell, and Lars Roed Ingerslev for their input on data analysis and visualization.

Author contributions

Conceptualization: RMJ, TVdS, BS, EL, PM, JV, JO, MH, WD, ASD

Methodology: RMJ, TVdS, BS, JL, RAS, DS, OD, AVdL, EL, LMA, KVV, LM, MW, PM, JV, MH, WD, ASD

Software: RMJ, TVdS, BS, DS, LMA, RB, JA

Validation: RMJ, TVdS, BS, JL, LM, PM, JV, WD, ASD

Formal Analysis: RMJ, TVdS, BS, JL, DS, LMA

Investigation: RMJ, TVdS, BS, JL, RAS, DS, AVdL, EL, LMA, KVV, LM, NY, AW, RVT, RES, EZ, MWL

Resources: RES, EZ, MWL, MW, PM, JV, JO, MH, WD, ASD

Data curation: RMJ, TVdS, BS, JL, DS, LMA, JA

Writing – Original Draft: RMJ, TVdS, BS, WD, ASD

Writing – Review and Editing: RMJ, TVdS, BS, JL, RAS, DS, OD, AVdL, EL, LMA, RB, KVV, LM, NY, JA, AW, RVT, RES, EZ, MWL, MW, PM, JV, JO, MH, WD, ASD

Visualization: RMJ, TVdS, BS, JL, LMA, OD

Supervision: BS, PM, JV, JO, MH, WD, ASD

Project Administration: RMJ, TVdS, BS, WD, ASD

Funding Acquisition: TVdS, EL, PM, JV, JO, MH, WD, ASD

Competing interests

The authors declare no competing interests.

1260 **Figure legends**

1261

1262 **Figure 1. Transcriptomic- and proteomic-based clustering reveals only two distinct fiber**
1263 **types. (A)** Transcriptomic and proteomic workflow. **(B-D)** Dynamic range curves for MYH7,
1264 MYH2, and MYH1, with calculated assignment thresholds for fiber typing. **(E-F)** Distribution of
1265 fibers by expression of MYHs in transcriptomics and proteomics datasets. **(G-H)** Uniform
1266 manifold approximation and projection (UMAP) plots for transcriptomics and proteomics,
1267 colored by MYH-based fiber type. **(I-J)** Feature plots displaying the expression of MYH7, MYH2,
1268 and MYH1 in transcriptomics and proteomics.

1269

1270 **Figure 2. Skeletal muscle fiber heterogeneity beyond MYHs. (A)** Principal component analysis
1271 (PCA) plots of transcriptomics and proteomics datasets colored by MYH-based fiber type. **(B)**
1272 Enrichment analysis of transcript and protein drivers of PC2 and PC1. **(C-D)** PCA plot colored
1273 by cell-cell adhesion gene ontology (GO) term in the transcriptome, and by costamere GO
1274 term in the proteome. Arrows represent transcript and protein drivers and their direction. **(E-**
1275 **F)** Uniform manifold approximation and projection (UMAP) feature plots of clinically relevant
1276 features displaying a slow/fast fiber type-independent gradient of expression. **(G-H)**
1277 Correlation between drivers of PC2 and PC1 between the transcriptome and proteome.

1278

1279 **Figure 3. Ribosomal heterogeneity drives fiber type-independent heterogeneity. (A)**
1280 Principal component analysis (PCA) plot colored by cytosolic ribosome gene ontology (GO)
1281 term in the proteome. Arrows indicate the direction towards which the proteins are driving
1282 the variance in the PCA plot. The length of the lines represents the principal component score
1283 for a given protein. **(B-C)** PCA feature plots of RPS13 and RPL38. **(D)** Unsupervised hierarchical

1284 clustering analysis of proteins constituting the cytosolic ribosome. **(E)** Structural model of the
1285 80S ribosome (PDB: 4V6X) highlighting ribosomal proteins displaying variable abundance
1286 across skeletal muscle fibers. **(F)** Ribosomal proteins with variable stoichiometry located close
1287 to the mRNA exit tunnel.
1288
1289 **Figure 4. Fast and slow skeletal muscle fiber signatures. (A-B)** Volcano plots comparing the
1290 slow and fast clusters identified from the uniform manifold approximation and projection
1291 (UMAP) plots in Fig 1G-H. Coloured dots represent significantly different transcripts or
1292 proteins at an FDR < 0.05, darker dots represent significantly different transcripts or proteins
1293 with a log fold change > 1. (**C**) Feature plots of selected differentially expressed genes or
1294 proteins between slow and fast fibers. **(D)** Enrichment analysis of significantly different
1295 transcript and proteins. Overlap – enriched in both datasets, Transcriptome – enriched only in
1296 transcriptome, Proteome – enriched only in proteome. **(E)** Fiber type specific transcription
1297 factors as identified by SCENIC, based on SCENIC-derived regulon specificity score and
1298 differential mRNA expression between fiber types. (**F**) Feature plots of selected differentially
1299 expressed transcription factors between slow and fast fibers.
1300
1301 **Figure 5. Non-coding RNA and associated microproteins in human skeletal muscle fibers. (A)**
1302 Significantly regulated non-coding RNA transcripts in slow and fast fibers. **(B)** Representative
1303 RNAscope images displaying the slow/fast fiber-type specificity of LINC01405 and RP11-
1304 255P5.3, respectively. Scaling bar = 50 µm. **(C)** Quantification of RNAscope data for fiber type
1305 specific non-coding RNA expression. **(D)** De novo microprotein identification workflow. **(E)** The
1306 microprotein LINC01405_ORF408:17441:17358 is specific to slow skeletal muscle fibers.
1307

1308 **Figure 6. Nemaline myopathies induce a shift towards faster, less oxidative skeletal muscle**
1309 **fibers. (A)** Microscopy images displaying fiber atrophy or hypotrophy and divergent MYH-
1310 based fiber type predominance in *ACTA1*- and *TNNT1*-nemaline myopathies (NM). Scaling bar
1311 = 100 µm. **(B)** MYH-based fiber type proportions by participant. **(C)** Principal component
1312 analysis (PCA) plot of skeletal muscle fibers from nemaline myopathy patients and controls.
1313 **(D)** Skeletal muscle fibers from nemaline myopathy patients and controls projected onto PCA
1314 plot determined from the 1000 fibers analyzed in Fig 2. **(E-G)** Volcano plots comparing the
1315 *ACTA1*- and *TNNT1*-nemaline myopathies with control participants and between *ACTA1*- and
1316 *TNNT1*-nemaline myopathies. Colored circles represent significantly different proteins at $\pi <$
1317 0.05, darker dots represent significantly different proteins at FDR < 0.05. **(H)** Enrichment
1318 analysis of significantly different proteins in the whole proteome and within type 1 and type
1319 2A fibers. **(I-J)** Principal component analysis (PCA) plot colored by extracellular matrix and
1320 mitochondria gene ontology (GO) terms.
1321
1322 **Supplemental Figure Legends**
1323
1324 **Figure 1 S1**. **Quality control of novel transcriptomic and proteomic workflows.** (**A**) Detailed
1325 schematic of developed workflows. (**B-C**) Number of quantified genes/proteins by participant
1326 and sample in 1000 fiber transcriptomics and proteomics. (**D**) Coefficient of variation by
1327 protein in 1000 fiber proteomics. (**E-F**) Dynamic range of genes in 1000 fiber transcriptomics
1328 and of proteins in 1000 fiber proteomics. (**G**) Overlapping features within 1000 fiber
1329 transcriptomics and proteomics. (**H**) Correlation between features within 1000 fiber
1330 transcriptomics and proteomics.
1331

1332 **Figure 1 S2. Higher sensitivity with proteomics compared to standard dot blotting.** (**A**) MYH-
1333 based fiber type proportions by participant. (**B**) Comparison between dot blot- and
1334 proteomics-based fiber typing. The pie chart indicates the abundance for each MYH isoform
1335 in the single-fiber proteomics data.
1336
1337 **Figure 1 S3. Clustering of transcriptomic and proteomic data.** (**A-B**) Scree plots of
1338 transcriptomics and proteomics. Colored box indicates the number of principal components
1339 used for clustering. (**C-D**) 1000 fiber transcriptomics and proteomics UMAP colored by
1340 participant. (**E**) 1000 fiber transcriptomics UMAP colored by trial day.
1341
1342 **Figure 1 S4. Type 2X is not a distinct fiber type.** (**A-B**) Feature plots for ACTN3 and MYLK2
1343 expression/abundance in transcriptomics and proteomics data. (**C-H**) U-plots demonstrating
1344 correlation of transcripts/proteins with the different MYH isoforms. X-axis depicts Pearson's r
1345 coefficient, y-axis depicts -log10 of the p-value. (**I-J**) UMAP plots for transcriptomics and
1346 proteomics showing blended expression of MYH7 (blue), MYH2 (green) and MYH1 (red).
1347
1348 **Figure 2 S1. Heterogeneity of fibers with well-known fiber type specific features.** (**A-B**) Fiber
1349 type curves of established slow fiber type genes/proteins in 1000 fiber transcriptomics and
1350 proteomics. (**C-D**) Proportion of fibers determined to be slow via different numerical
1351 combinations of genes/proteins (from A-B) in 1000 fiber transcriptomics and proteomics.
1352
1353 **Figure 2 S2. Additional data of Principal Component Analysis (PCA).** (**A-B**) 1000 fiber
1354 transcriptomics PCA plot colored by participant or trial day. (**C**) 1000 fiber proteomics PCA plot
1355 colored by participant. (**D-E**) Top gene and protein drivers of PC1 and PC2**.**

1356

1357 **Figure 3 S1. Ribosomal heterogeneity of skeletal muscle fibers.** (**A**) mRNA expression of
1358 ribosomal proteins in skeletal muscle compared to the whole body. Data derived from Panda
1359 et al[67]. (**B**) PCA plot colored by cytosolic ribosome gene ontology (GO) term in the
1360 transcriptome. Arrows indicate the direction towards which the proteins are driving the
1361 variance in the PCA plot. The length of the lines represents the principal component score for
1362 a given protein. (**C**) Differences in protein abundance of ribosomal proteins in single muscle
1363 fibers compared to the median abundance. (**C**) Proportions of ribosomal proteins in each
1364 cluster by small (40S) and large (60S) subunits.

1365

1366 **Figure 4 S1. Gene and protein signatures of fast and slow fibers.** (**A**) Feature plots of LDH
1367 protein isoforms between slow and fast fibers. (**B**) Overlap of significantly different
1368 genes/proteins between slow and fast skeletal muscle fibers in 1000 fiber transcriptomics and
1369 proteomics. (**C**) Correlation between the $\log_2$ fold change difference between slow and fast
1370 skeletal muscle fibers within 1000 fiber transcriptomics and proteomics. (**D-K**) Expression
1371 profiles of top drivers of selected enrichment terms within slow or fast fibers with indication
1372 of adjusted p-values.

1373

1374 **Figure 5 S1. Specific expression of non-coding RNA and microproteins in skeletal muscle.** (**A-**
1375 **B**) Expression profile of *LINC01405* and *RP11-255P5.3* in different tissues. (**C**) Volcano plots
1376 comparing microprotein abundance between the slow and fast clusters identified from the
1377 uniform manifold approximation and projection (UMAP) plots in Fig 1G-H. Colored dots
1378 represent significantly different microproteins at an FDR < 0.05. **(D)** Slow/fast fiber-type

1379 comparison of LINC01405_ORF52 14515:14294 and LINC01405_ORF503 18862:18770
1380 microproteins.
1381
1382 **Figure 6 S1. Quality control and fiber typing of nemaline myopathy dataset.** (**A**) Number of
1383 quantified proteins by participant and sample in nemaline myopathy proteomics. (**B**) Dynamic
1384 range of proteins in nemaline myopathy proteomics. (**C**) Correlation between features within
1385 1000 fiber proteomics and healthy controls of nemaline myopathy proteomics. (**D**) Dynamic
1386 range curves for MYH7, MYH2, and MYH1, with calculated assignment thresholds for fiber
1387 typing. (**E**) Distribution of fibers by expression of MYHs in nemaline myopathy proteomics.
1388
1389 **Figure 6 S2. Fiber type-independent remodelling in nemaline myopathy.** (**A**) Correlation
1390 between the $\log_2$ fold change difference between *ACTA1*- and *TNNT1*-nemaline myopathies
1391 with control participants. (**B**) PCA of nemaline myopathy patients (pseudobulked protein
1392 profile form single fibers). (**C**) Upset plot of significantly regulated proteins *ACTA1*- and *TNNT1*-
1393 nemaline myopathies. (**D-I**) Volcano plots comparing the *ACTA1*- and *TNNT1*-nemaline
1394 myopathies with control participants and between *ACTA1*- and *TNNT1*-nemaline myopathies
1395 by MYH-based fiber type. Colored circles represent significantly different proteins at $\pi < 0.05$,
1396 darker dots represent significantly different proteins at FDR < 0.05.
1397
1398 **Figure 6 S3. Effects of nemaline myopathy on microproteins and the sarcolemma repair**
1399 **machinery. (A)** Protein abundance of identified microproteins within ACTA1-, TNNT1- and
1400 control participants. Significantly different comparisons between groups are highlighted. **(B)**
1401 Abundance of annexin proteins in *ACTA1*- and *TNNT1*-nemaline myopathy. (**C**) Schematic of
1402 changes within the sarcolemma repair machinery in nemaline myopathy.

1403

1404 **Figure 6 S4. Bulk muscle proteomics recapitulates single-fiber analysis of nemaline**
1405 **myopathy samples.** (**A**) Workflow of bulk muscle proteomics for control participants and
1406 *TNNT1*-nemaline myopathy patients. (**B**) Principal component analysis (PCA) plot of bulk
1407 skeletal muscle from *TNNT1*-nemaline myopathy patients and controls. **(C)** Volcano plot
1408 comparing the *TNNT1*-nemaline myopathy with control participants. Colored circles represent
1409 significantly different proteins at $\pi < 0.05$, darker dots represent significantly different proteins
1410 at FDR < 0.05. **(D)** Enrichment analysis of significantly different proteins in the bulk muscle
1411 proteome between *TNNT1*-nemaline myopathy patients and control participants.

1412

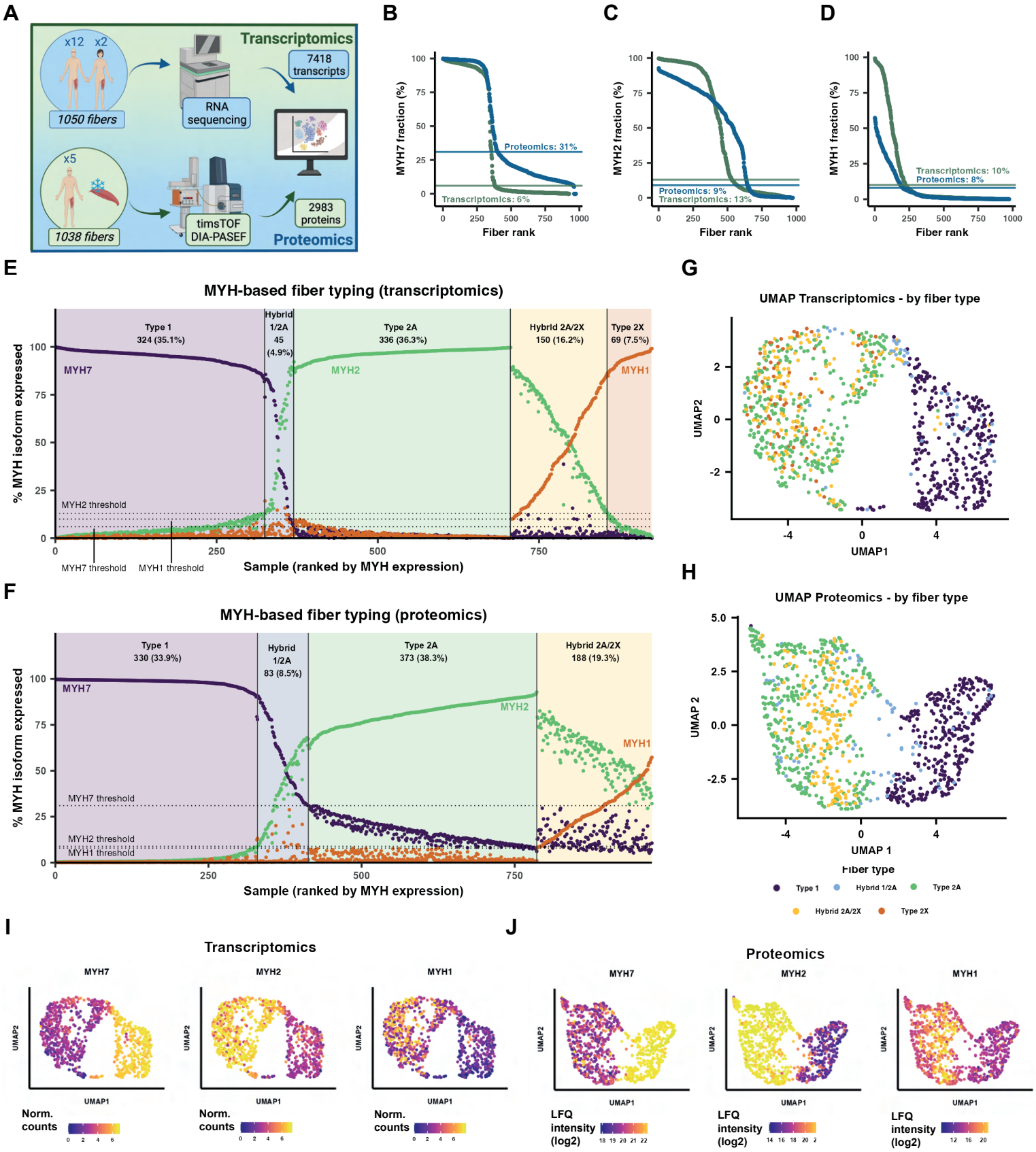
A
Transcriptomics
x12
x2
1050 fibers
RNA sequencing
7418 transcripts
x5
1038 fibers
timsTOF DIA-PASEF
2983 proteins
Proteomics
B
MYH7 fraction (%)
Proteomics: 31%
Transcriptomics: 6%
Fiber rank
C
MYH2 fraction (%)
Proteomics: 9%
Transcriptomics: 13%
Fiber rank
D
MYH1 fraction (%)
Transcriptomics: 10%
Proteomics: 8%
Fiber rank
E
MYH-based fiber typing (transcriptomics)
Type 1 324 (35.1%)
Hybrid 1/2A 45 (4.9%)
Type 2A 336 (36.3%)
Hybrid 2A/2X 150 (16.2%)
Type 2X 69 (7.5%)
MYH7
MYH2
MYH1
MYH2 threshold
MYH7 threshold
MYH1 threshold
% MYH isoform expressed
Sample (ranked by MYH expression)
F
MYH-based fiber typing (proteomics)
Type 1 330 (33.9%)
Hybrid 1/2A 83 (8.5%)
Type 2A 373 (38.3%)
Hybrid 2A/2X 188 (19.3%)
MYH7
MYH2
MYH1
MYH7 threshold
MYH2 threshold
MYH1 threshold
% MYH isoform expressed
Sample (ranked by MYH expression)
G
UMAP Transcriptomics - by fiber type
UMAP2
UMAP1
H
UMAP Proteomics - by fiber type
UMAP 2
UMAP 1
Fiber type
Type 1
Hybrid 1/2A
Type 2A
Hybrid 2A/2X
Type 2X
I
Transcriptomics
MYH7
MYH2
MYH1
UMAP2
UMAP1
Norm. counts
J
Proteomics
MYH7
MYH2
MYH1
LFQ intensity (log2)

Figure 1

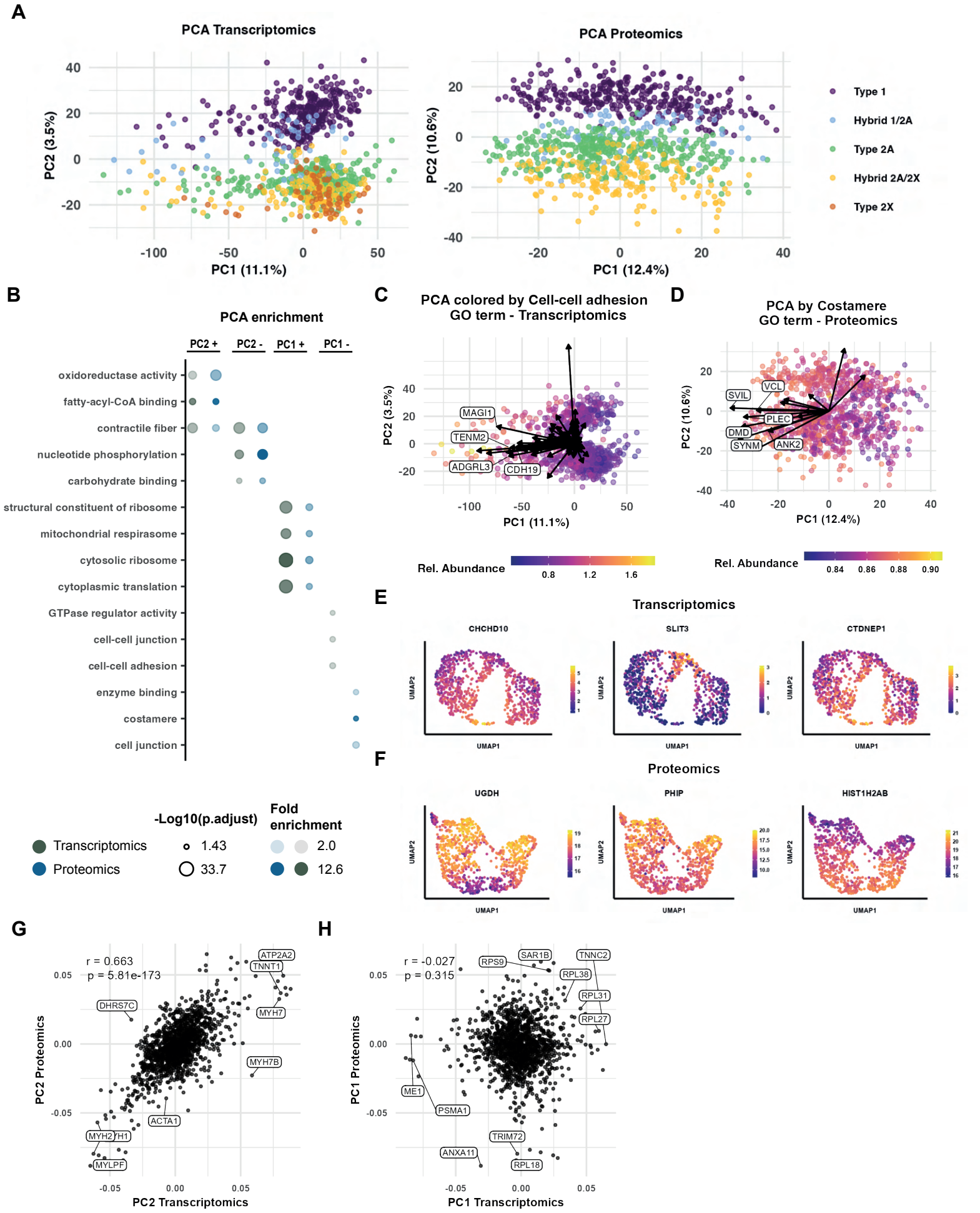
A
PCA Transcriptomics
PC2 (3.5%)
PC1 (11.1%)
PCA Proteomics
PC2 (10.6%)
PC1 (12.4%)
Type 1
Hybrid 1/2A
Type 2A
Hybrid 2A/2X
Type 2X
B
PCA enrichment
PC2 +
PC2 -
PC1 +
PC1 -
oxidoreductase activity
fatty-acyl-CoA binding
contractile fiber
nucleotide phosphorylation
carbohydrate binding
structural constituent of ribosome
mitochondrial respirasome
cytosolic ribosome
cytoplasmic translation
GTPase regulator activity
cell-cell junction
cell-cell adhesion
enzyme binding
costamere
cell junction
Transcriptomics
Proteomics
-Log10(p.adjust)
1.43
33.7
Fold enrichment
2.0
12.6
C
PCA colored by Cell-cell adhesion GO term - Transcriptomics
MAGI1
TENM2
ADGRL3
CDH19
Rel. Abundance
0.8
1.2
1.6
D
PCA by Costamere GO term - Proteomics
SVIL
VCL
PLEC
DMD
SYNM
ANK2
Rel. Abundance
0.84
0.86
0.88
0.90
E
Transcriptomics
CHCHD10
SLIT3
CTDNEP1
UMAP1
UMAP2
F
Proteomics
UGDH
PHIP
HIST1H2AB
G
r = 0.663
p = 5.81e-173
ATP2A2
TNNT1
DHRS7C
MYH7
MYH7B
ACTA1
MYH2
MYH1
MYLPF
PC2 Proteomics
PC2 Transcriptomics
H
r = -0.027
p = 0.315
RPS9
SAR1B
TNNC2
RPL38
RPL31
RPL27
ME1
PSMA1
TRIM72
ANXA11
RPL18
PC1 Proteomics
PC1 Transcriptomics

Figure 2

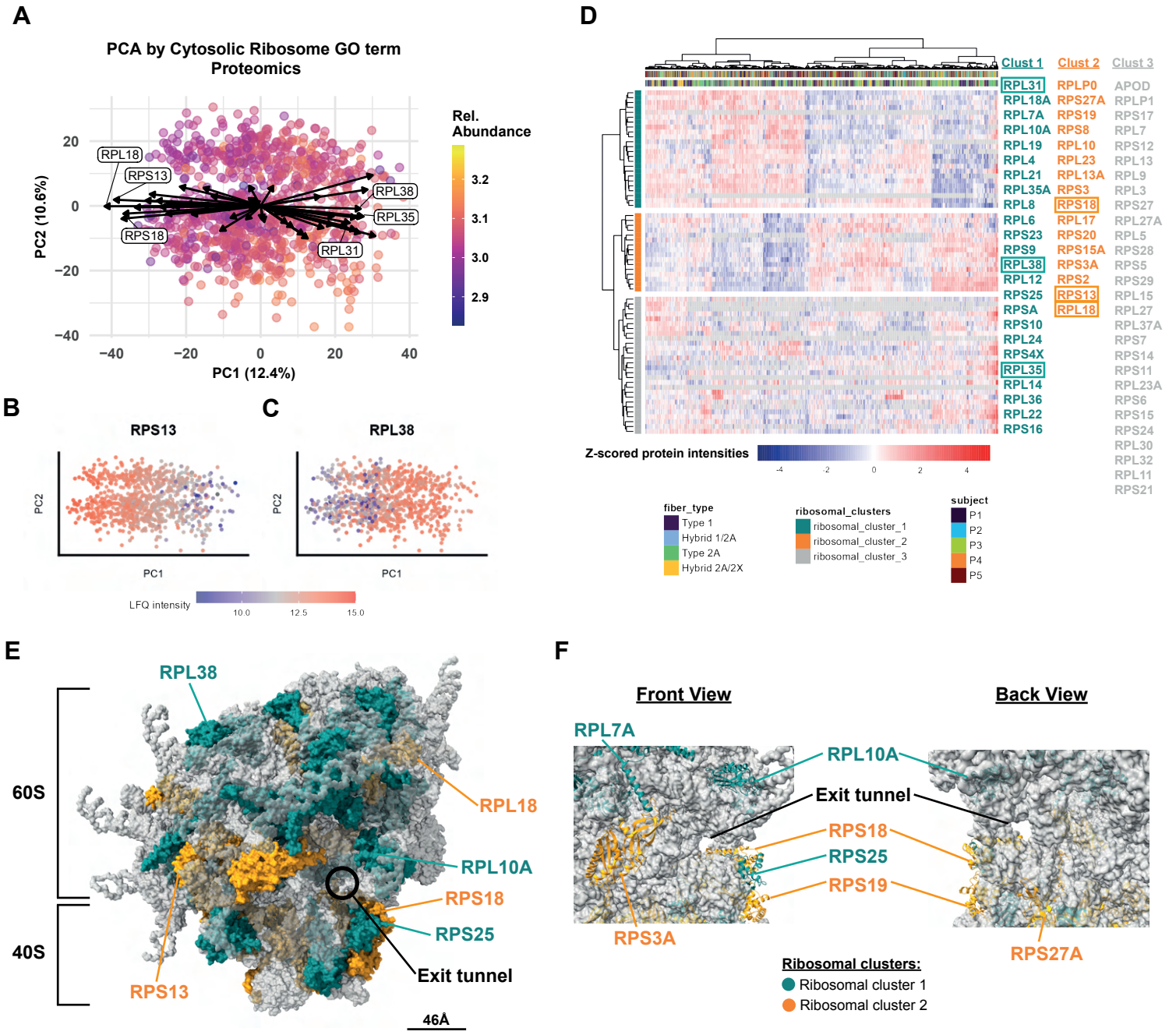
A
PCA by Cytosolic Ribosome GO term Proteomics
Rel. Abundance
3.2
3.1
3.0
2.9
RPL18
RPS13
RPS18
RPL38
RPL35
RPL31
PC2 (10.6%)
PC1 (12.4%)
20
0
−20
−40
−40
−20
0
20
40
B
RPS13
C
RPL38
PC2
PC1
LFQ intensity
10.0
12.5
15.0
D
Clust 1
Clust 2
Clust 3
RPL31
RPL18A
RPL7A
RPL10A
RPL19
RPL4
RPL21
RPL35A
RPL8
RPL6
RPS23
RPS9
RPL38
RPL12
RPS25
RPSA
RPS10
RPL24
RPS4X
RPL35
RPL14
RPL36
RPL22
RPS16
RPLP0
RPS27A
RPS19
RPS8
RPL10
RPL23
RPL13A
RPS3
RPS18
RPL17
RPS20
RPS15A
RPS3A
RPS2
RPS13
RPL18
APOD
RPLP1
RPS17
RPL7
RPS12
RPL13
RPL9
RPL3
RPS27
RPL27A
RPL5
RPS28
RPS5
RPS29
RPL15
RPL27
RPL37A
RPS7
RPS14
RPS11
RPL23A
RPS6
RPS15
RPS24
RPL30
RPL32
RPL11
RPS21
Z-scored protein intensities
-4
-2
0
2
4
fiber_type
Type 1
Hybrid 1/2A
Type 2A
Hybrid 2A/2X
ribosomal_clusters
ribosomal_cluster_1
ribosomal_cluster_2
ribosomal_cluster_3
subject
P1
P2
P3
P4
P5
E
RPL38
60S
RPL18
RPL10A
RPS18
RPS25
40S
RPS13
Exit tunnel
46Å
F
Front View
Back View
RPL7A
RPL10A
Exit tunnel
RPS18
RPS25
RPS19
RPS3A
RPS27A
Ribosomal clusters:
Ribosomal cluster 1
Ribosomal cluster 2

Figure 3

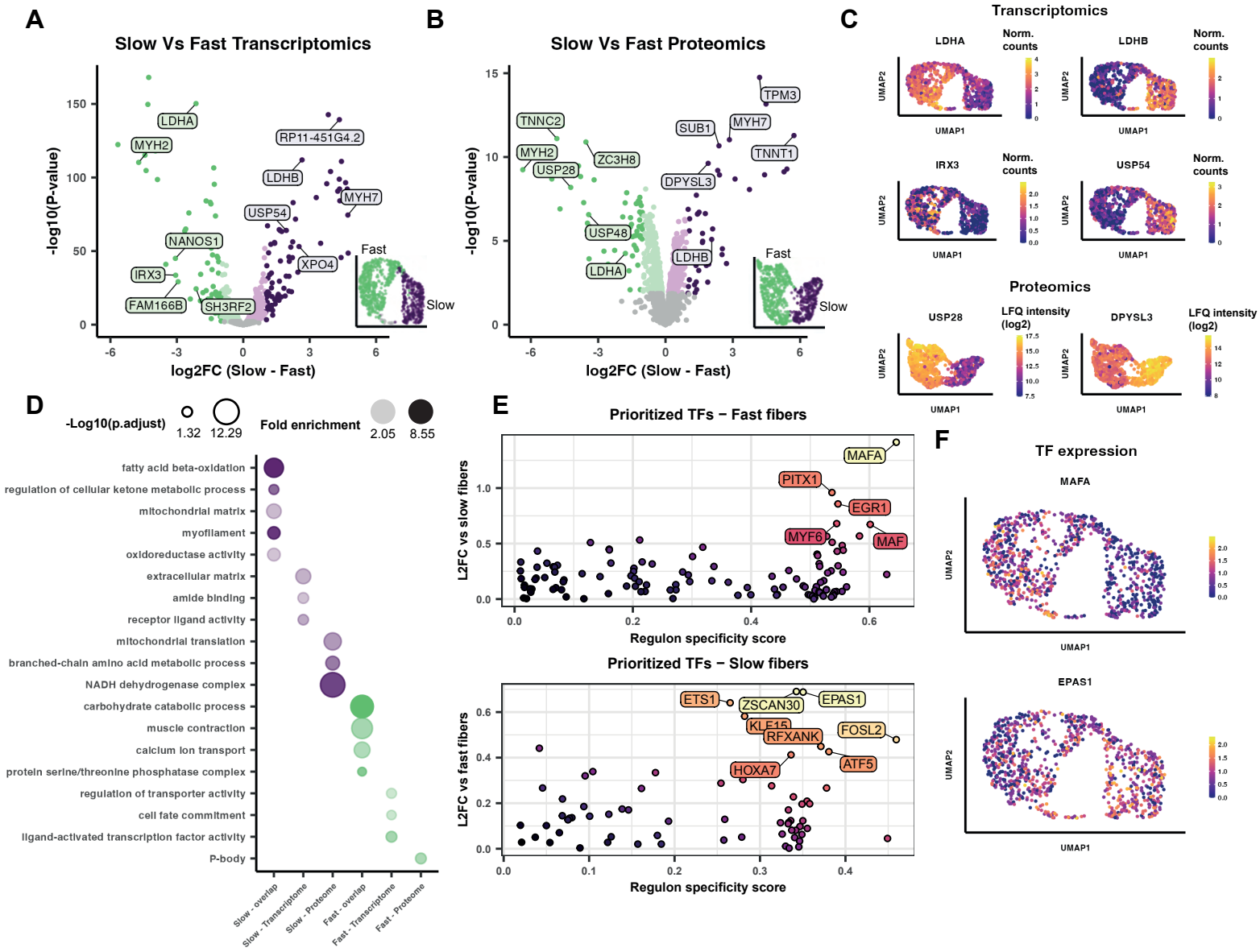
A
Slow Vs Fast Transcriptomics
-log10(P-value)
log2FC (Slow - Fast)
LDHA
MYH2
RP11-451G4.2
LDHB
MYH7
USP54
NANOS1
XPO4
IRX3
FAM166B
SH3RF2
Fast
Slow
B
Slow Vs Fast Proteomics
-log10(P-value)
log2FC (Slow - Fast)
TPM3
TNNC2
SUB1
MYH7
MYH2
ZC3H8
TNNT1
USP28
DPYSL3
USP48
LDHB
LDHA
Fast
Slow
C
Transcriptomics
LDHA
LDHB
IRX3
USP54
Norm. counts
UMAP1
UMAP2
Proteomics
USP28
DPYSL3
LFQ intensity (log2)
D
-Log10(p.adjust)
1.32
12.29
Fold enrichment
2.05
8.55
fatty acid beta-oxidation
regulation of cellular ketone metabolic process
mitochondrial matrix
myofilament
oxidoreductase activity
extracellular matrix
amide binding
receptor ligand activity
mitochondrial translation
branched-chain amino acid metabolic process
NADH dehydrogenase complex
carbohydrate catabolic process
muscle contraction
calcium ion transport
protein serine/threonine phosphatase complex
regulation of transporter activity
cell fate commitment
ligand-activated transcription factor activity
P-body
Slow - overlap
Slow - Transcriptome
Slow - Proteome
Fast - overlap
Fast - Transcriptome
Fast - Proteome
E
Prioritized TFs – Fast fibers
L2FC vs slow fibers
Regulon specificity score
MAFA
PITX1
EGR1
MYF6
MAF
Prioritized TFs – Slow fibers
L2FC vs fast fibers
Regulon specificity score
ETS1
ZSCAN30
EPAS1
KLF15
RFXANK
FOSL2
HOXA7
ATF5
F
TF expression
MAFA
EPAS1
UMAP1
UMAP2

Figure 4

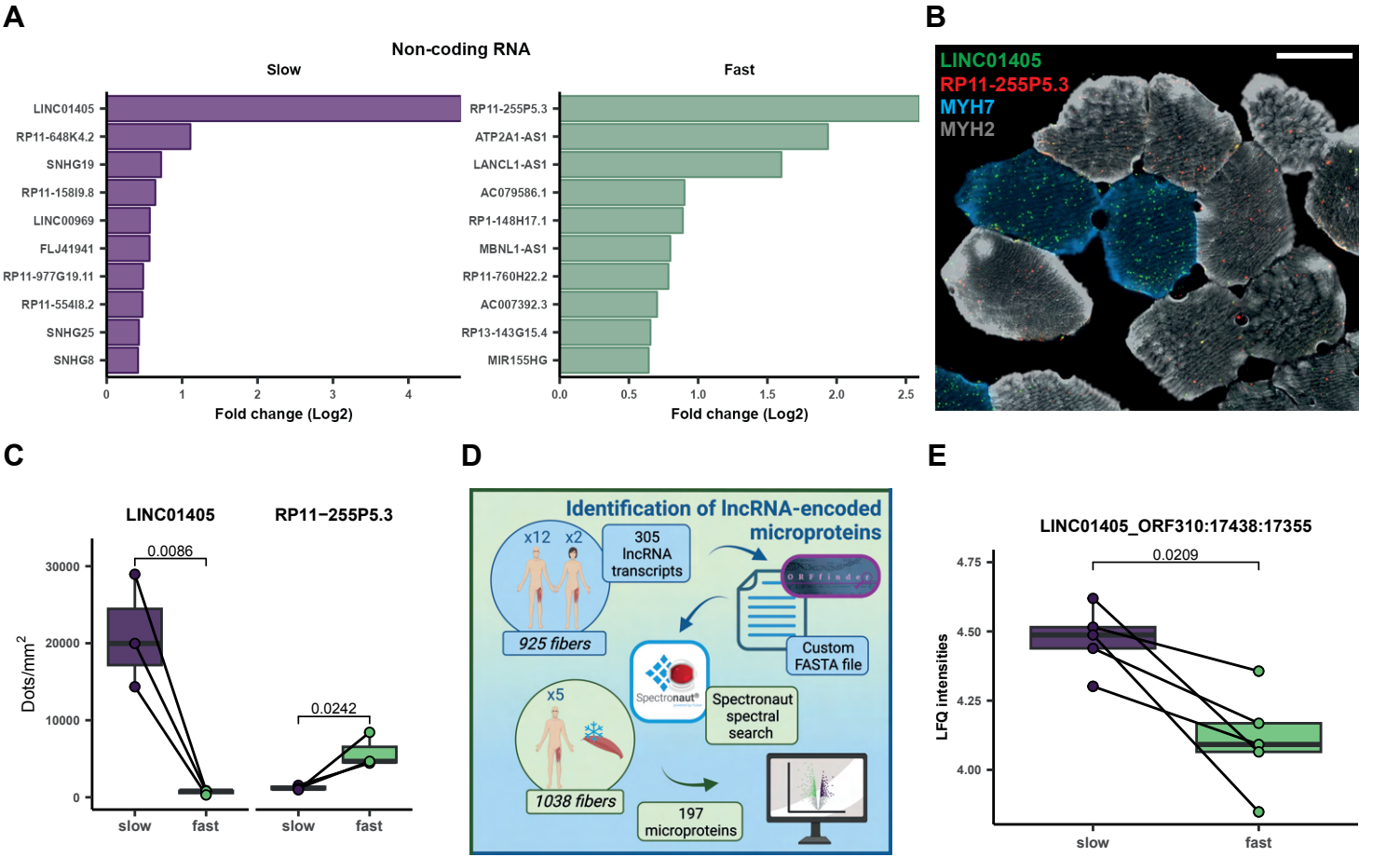
A
Non-coding RNA
Slow
LINC01405
RP11-648K4.2
SNHG19
RP11-158I9.8
LINC00969
FLJ41941
RP11-977G19.11
RP11-554I8.2
SNHG25
SNHG8
0
1
2
3
4
Fold change (Log2)
Fast
RP11-255P5.3
ATP2A1-AS1
LANCL1-AS1
AC079586.1
RP1-148H17.1
MBNL1-AS1
RP11-760H22.2
AC007392.3
RP13-143G15.4
MIR155HG
0.0
0.5
1.0
1.5
2.0
2.5
Fold change (Log2)
B
LINC01405
RP11-255P5.3
MYH7
MYH2
C
LINC01405
RP11−255P5.3
0.0086
0.0242
Dots/mm2
30000
20000
10000
0
slow
fast
slow
fast
D
Identification of lncRNA-encoded microproteins
x12
x2
305 lncRNA transcripts
925 fibers
ORFfinder
Custom FASTA file
Spectronaut
Spectronaut spectral search
x5
1038 fibers
197 microproteins
E
LINC01405_ORF310:17438:17355
0.0209
LFQ intensities
4.75
4.50
4.25
4.00
slow
fast

Figure 5

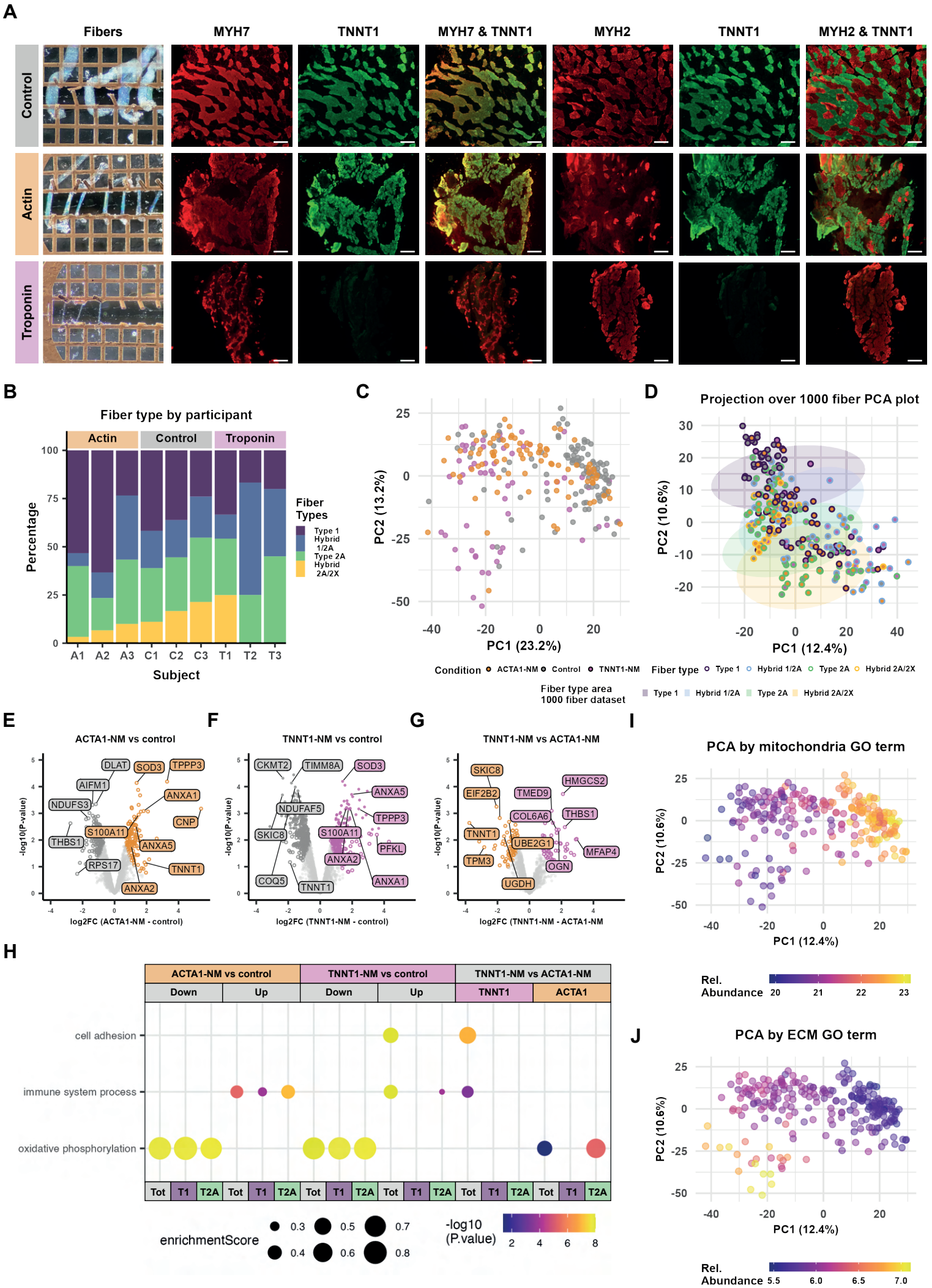
A
Fibers
MYH7
TNNT1
MYH7 & TNNT1
MYH2
TNNT1
MYH2 & TNNT1
Control
Actin
Troponin
B
Fiber type by participant
Actin
Control
Troponin
Percentage
Subject
A1 A2 A3 C1 C2 C3 T1 T2 T3
Fiber Types
Type 1
Hybrid 1/2A
Type 2A
Hybrid 2A/2X
C
PC2 (13.2%)
PC1 (23.2%)
Condition
ACTA1-NM
Control
TNNT1-NM
D
Projection over 1000 fiber PCA plot
PC2 (10.6%)
PC1 (12.4%)
Fiber type
Type 1
Hybrid 1/2A
Type 2A
Hybrid 2A/2X
Fiber type area
1000 fiber dataset
E
ACTA1-NM vs control
DLAT
SOD3
TPPP3
AIFM1
ANXA1
NDUFS3
CNP
S100A11
THBS1
ANXA5
RPS17
TNNT1
ANXA2
-log10(P-value)
log2FC (ACTA1-NM - control)
F
TNNT1-NM vs control
CKMT2
TIMM8A
SOD3
ANXA5
NDUFAF5
TPPP3
SKIC8
S100A11
PFKL
ANXA2
COQ5
TNNT1
ANXA1
log2FC (TNNT1-NM - control)
G
TNNT1-NM vs ACTA1-NM
SKIC8
HMGCS2
EIF2B2
TMED9
COL6A6
THBS1
TNNT1
UBE2G1
MFAP4
TPM3
OGN
UGDH
log2FC (TNNT1-NM - ACTA1-NM)
I
PCA by mitochondria GO term
PC2 (10.6%)
PC1 (12.4%)
Rel. Abundance
20 21 22 23
H
ACTA1-NM vs control
TNNT1-NM vs control
TNNT1-NM vs ACTA1-NM
Down
Up
Down
Up
TNNT1
ACTA1
cell adhesion
immune system process
oxidative phosphorylation
Tot T1 T2A Tot T1 T2A Tot T1 T2A Tot T1 T2A Tot T1 T2A Tot T1 T2A
enrichmentScore
0.3 0.4 0.5 0.6 0.7 0.8
-log10 (P.value)
2 4 6 8
J
PCA by ECM GO term
PC2 (10.6%)
PC1 (12.4%)
Rel. Abundance
5.5 6.0 6.5 7.0

Figure 6

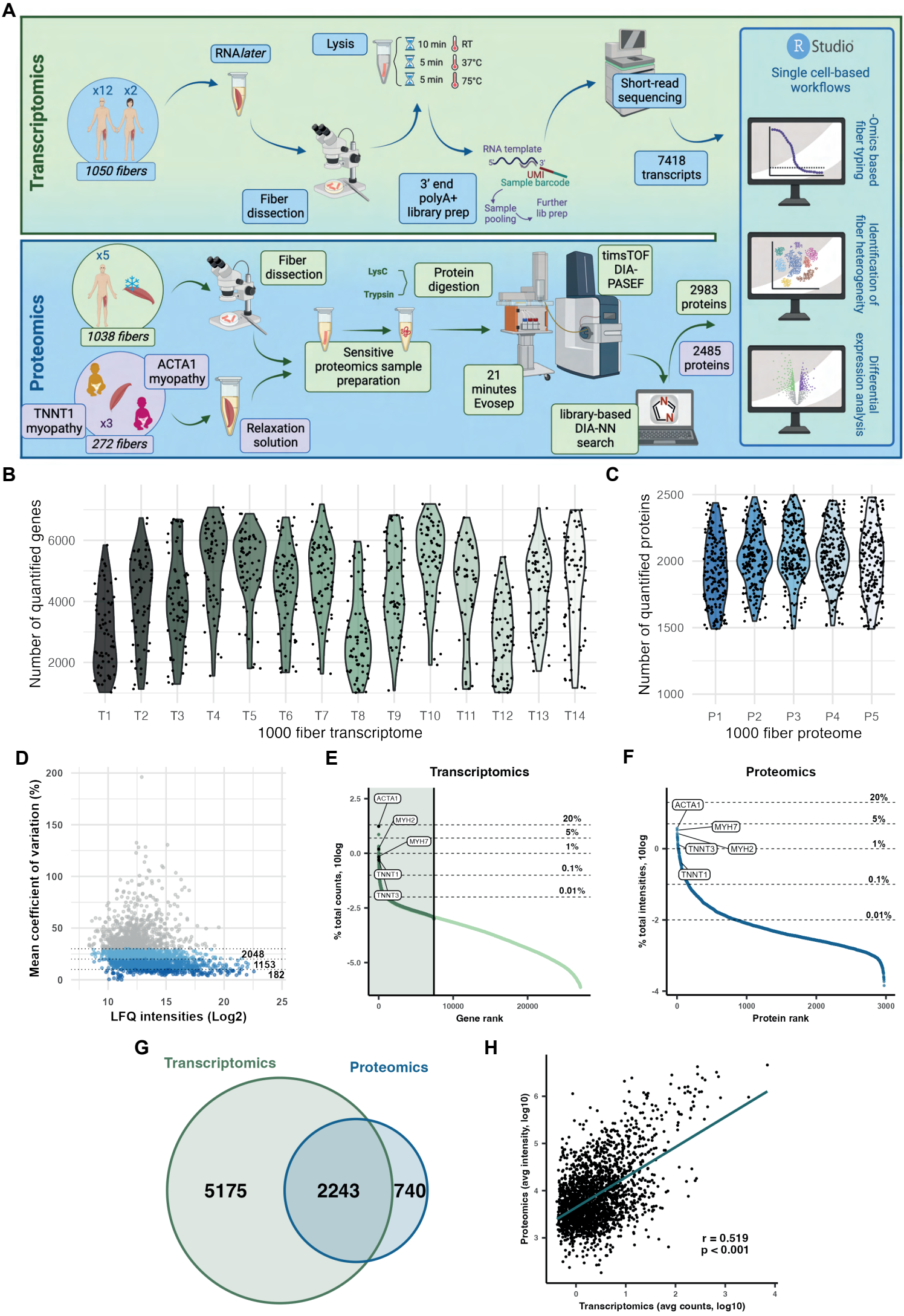
A
Transcriptomics
x12
x2
1050 fibers
RNA*later*
Lysis
10 min
5 min
5 min
RT
37°C
75°C
Fiber dissection
3' end polyA+ library prep
RNA template
UMI
Sample barcode
Sample pooling
Further lib prep
Short-read sequencing
7418 transcripts
Studio
Single cell-based workflows
-Omics based fiber typing
Identification of fiber heterogeneity
Differential expression analysis
Proteomics
x5
1038 fibers
ACTA1 myopathy
TNNT1 myopathy
x3
272 fibers
Fiber dissection
Relaxation solution
LysC
Trypsin
Protein digestion
Sensitive proteomics sample preparation
21 minutes Evosep
timsTOF DIA-PASEF
2983 proteins
2485 proteins
library-based DIA-NN search
B
Number of quantified genes
6000
4000
2000
T1
T2
T3
T4
T5
T6
T7
T8
T9
T10
T11
T12
T13
T14
1000 fiber transcriptome
C
Number of quantified proteins
2500
2000
1500
1000
P1
P2
P3
P4
P5
1000 fiber proteome
D
Mean coefficient of variation (%)
200
150
100
50
0
2048
1153
182
10
15
20
25
LFQ intensities (Log2)
E
Transcriptomics
% total counts, 10log
2.5
0.0
-2.5
-5.0
ACTA1
MYH2
MYH7
TNNT1
TNNT3
20%
5%
1%
0.1%
0.01%
0
10000
20000
Gene rank
F
Proteomics
% total intensities, 10log
0
-2
-4
ACTA1
MYH7
TNNT3
MYH2
TNNT1
20%
5%
1%
0.1%
0.01%
0
1000
2000
3000
Protein rank
G
Transcriptomics
Proteomics
5175
2243
740
H
Proteomics (avg intensity, log10)
6
5
4
3
r = 0.519
p < 0.001
0
1
2
3
4
Transcriptomics (avg counts, log10)

Figure 1 S1

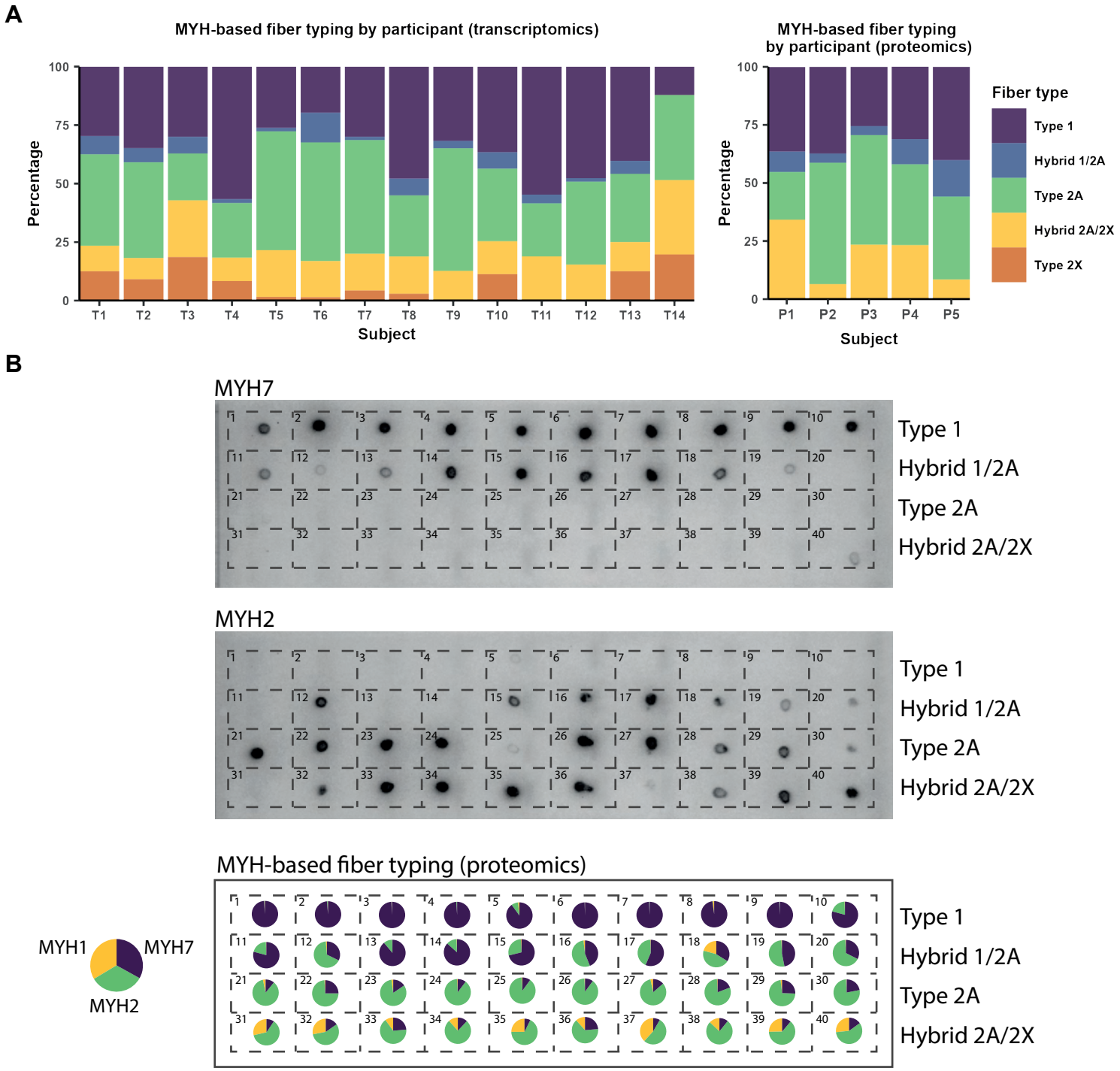
A
MYH-based fiber typing by participant (transcriptomics)
Percentage
100
75
50
25
0
T1
T2
T3
T4
T5
T6
T7
T8
T9
T10
T11
T12
T13
T14
Subject
MYH-based fiber typing
by participant (proteomics)
P1
P2
P3
P4
P5
Fiber type
Type 1
Hybrid 1/2A
Type 2A
Hybrid 2A/2X
Type 2X
B
MYH7
MYH2
MYH-based fiber typing (proteomics)
MYH1
MYH7
MYH2

Figure 1 S2

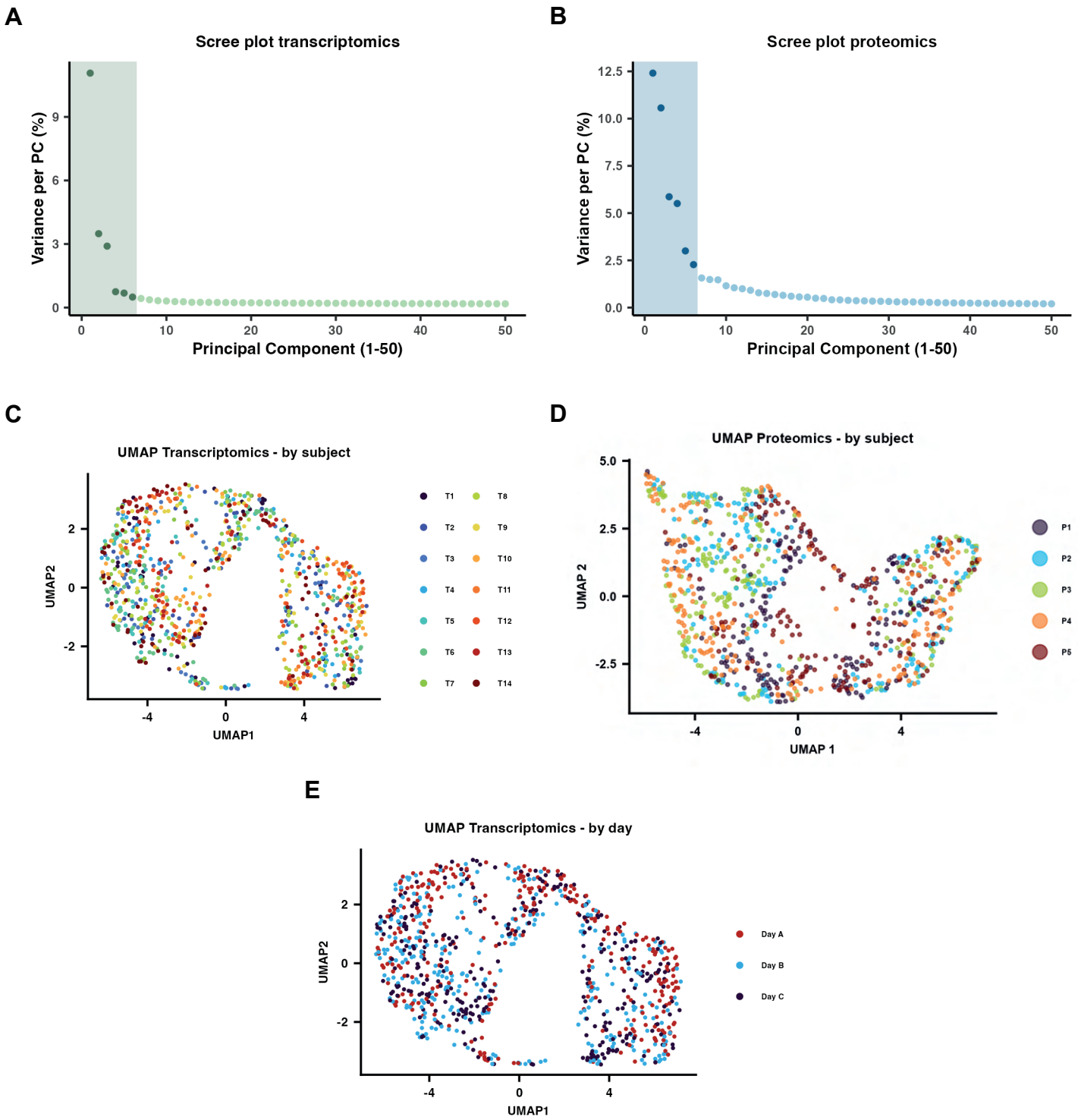
A
Scree plot transcriptomics
Variance per PC (%)
Principal Component (1-50)
B
Scree plot proteomics
Variance per PC (%)
Principal Component (1-50)
C
UMAP Transcriptomics - by subject
UMAP2
UMAP1
T1
T2
T3
T4
T5
T6
T7
T8
T9
T10
T11
T12
T13
T14
D
UMAP Proteomics - by subject
UMAP 2
UMAP 1
P1
P2
P3
P4
P5
E
UMAP Transcriptomics - by day
UMAP2
UMAP1
Day A
Day B
Day C

Figure 1 S3

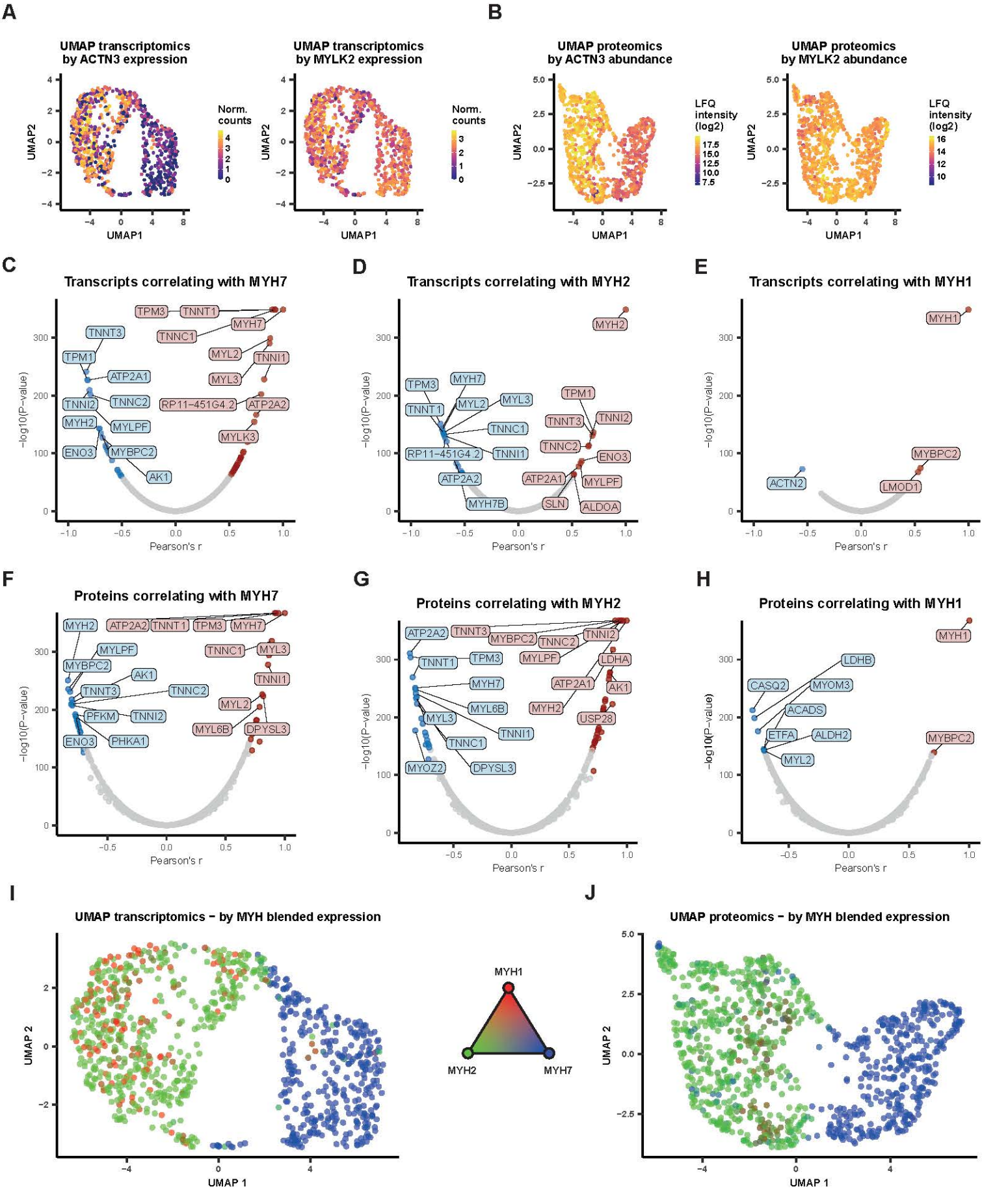
A
UMAP transcriptomics by ACTN3 expression
UMAP transcriptomics by MYLK2 expression
Norm. counts
UMAP1
UMAP2
B
UMAP proteomics by ACTN3 abundance
UMAP proteomics by MYLK2 abundance
LFQ intensity (log2)
C
Transcripts correlating with MYH7
D
Transcripts correlating with MYH2
E
Transcripts correlating with MYH1
F
Proteins correlating with MYH7
G
Proteins correlating with MYH2
H
Proteins correlating with MYH1
−log10(P−value)
Pearson's r
I
UMAP transcriptomics − by MYH blended expression
MYH1
MYH2
MYH7
J
UMAP proteomics − by MYH blended expression
UMAP 1
UMAP 2

Figure 1 S4

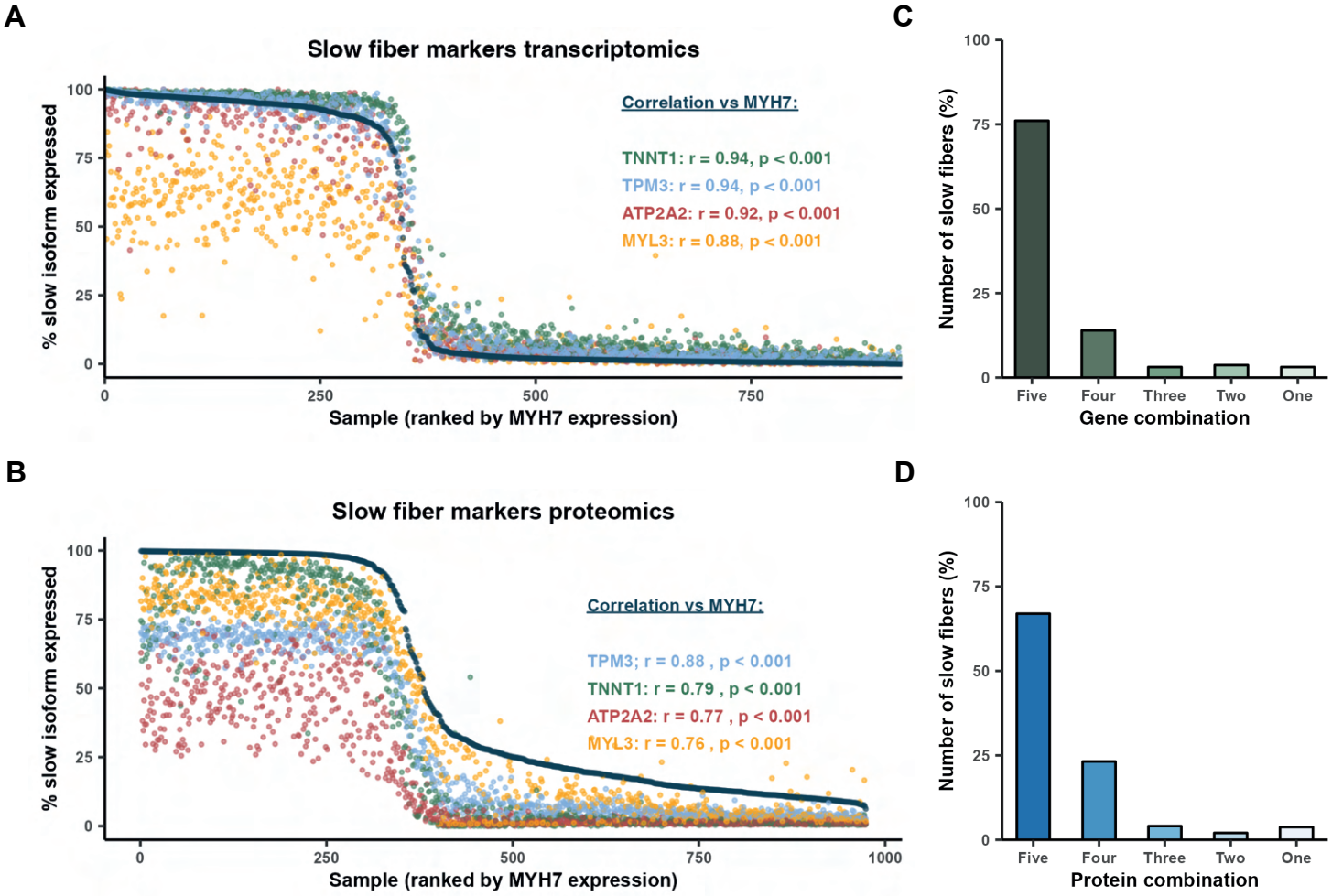
A
Slow fiber markers transcriptomics
Correlation vs MYH7:
TNNT1: r = 0.94, p < 0.001
TPM3: r = 0.94, p < 0.001
ATP2A2: r = 0.92, p < 0.001
MYL3: r = 0.88, p < 0.001
% slow isoform expressed
Sample (ranked by MYH7 expression)
C
Number of slow fibers (%)
Five
Four
Three
Two
One
Gene combination
B
Slow fiber markers proteomics
Correlation vs MYH7:
TPM3; r = 0.88 , p < 0.001
TNNT1: r = 0.79 , p < 0.001
ATP2A2: r = 0.77 , p < 0.001
MYL3: r = 0.76 , p < 0.001
% slow isoform expressed
Sample (ranked by MYH7 expression)
D
Number of slow fibers (%)
Five
Four
Three
Two
One
Protein combination

Figure 2 S1

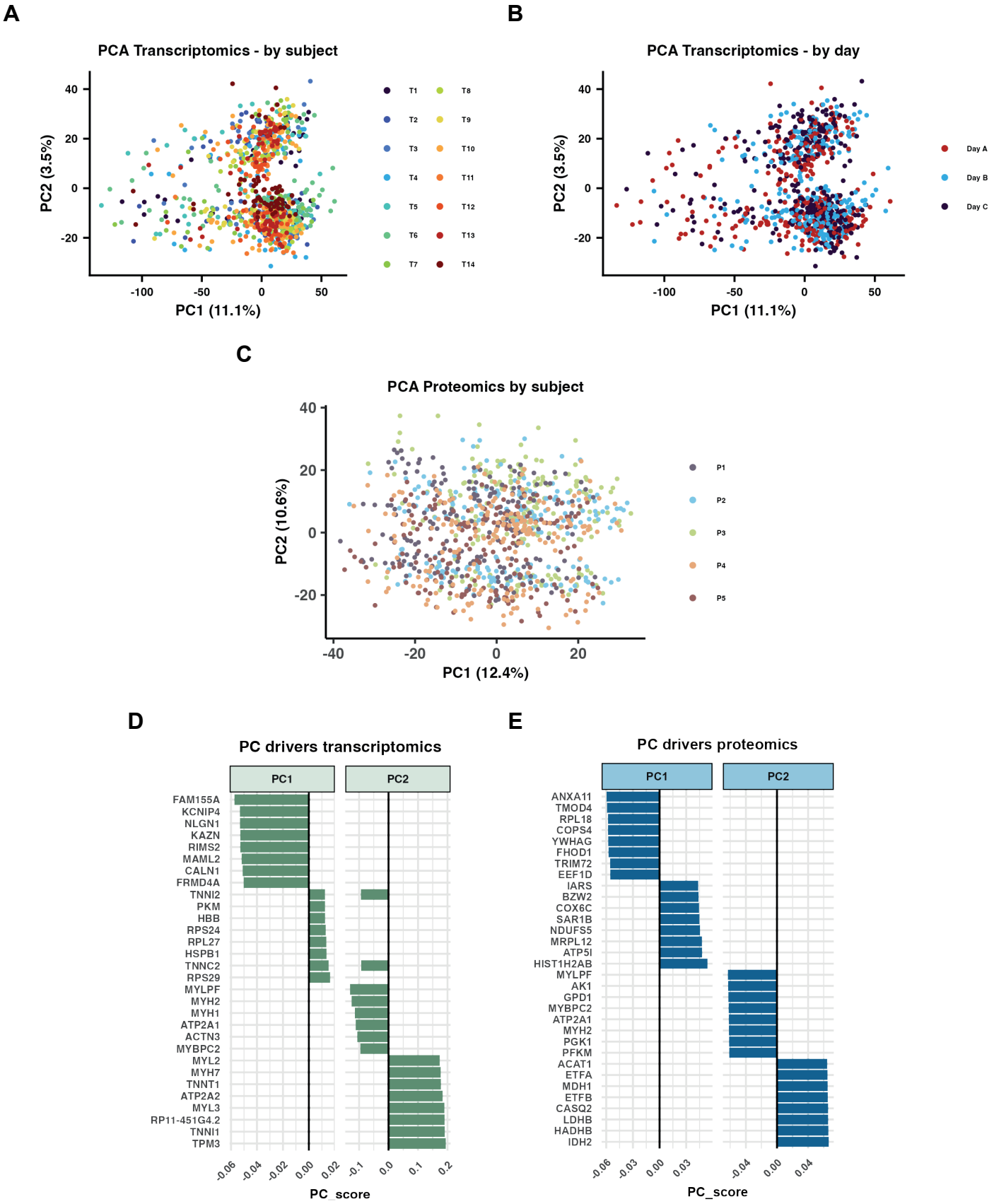
A
PCA Transcriptomics - by subject
PC2 (3.5%)
PC1 (11.1%)
T1
T2
T3
T4
T5
T6
T7
T8
T9
T10
T11
T12
T13
T14
B
PCA Transcriptomics - by day
PC2 (3.5%)
PC1 (11.1%)
Day A
Day B
Day C
C
PCA Proteomics by subject
PC2 (10.6%)
PC1 (12.4%)
P1
P2
P3
P4
P5
D
PC drivers transcriptomics
PC1
PC2
FAM155A
KCNIP4
NLGN1
KAZN
RIMS2
MAML2
CALN1
FRMD4A
TNNI2
PKM
HBB
RPS24
RPL27
HSPB1
TNNC2
RPS29
MYLPF
MYH2
MYH1
ATP2A1
ACTN3
MYBPC2
MYL2
MYH7
TNNT1
ATP2A2
MYL3
RP11-451G4.2
TNNI1
TPM3
PC_score
E
PC drivers proteomics
PC1
PC2
ANXA11
TMOD4
RPL18
COPS4
YWHAG
FHOD1
TRIM72
EEF1D
IARS
BZW2
COX6C
SAR1B
NDUFS5
MRPL12
ATP5I
HIST1H2AB
MYLPF
AK1
GPD1
MYBPC2
ATP2A1
MYH2
PGK1
PFKM
ACAT1
ETFA
MDH1
ETFB
CASQ2
LDHB
HADHB
IDH2
PC_score

Figure 2 S2

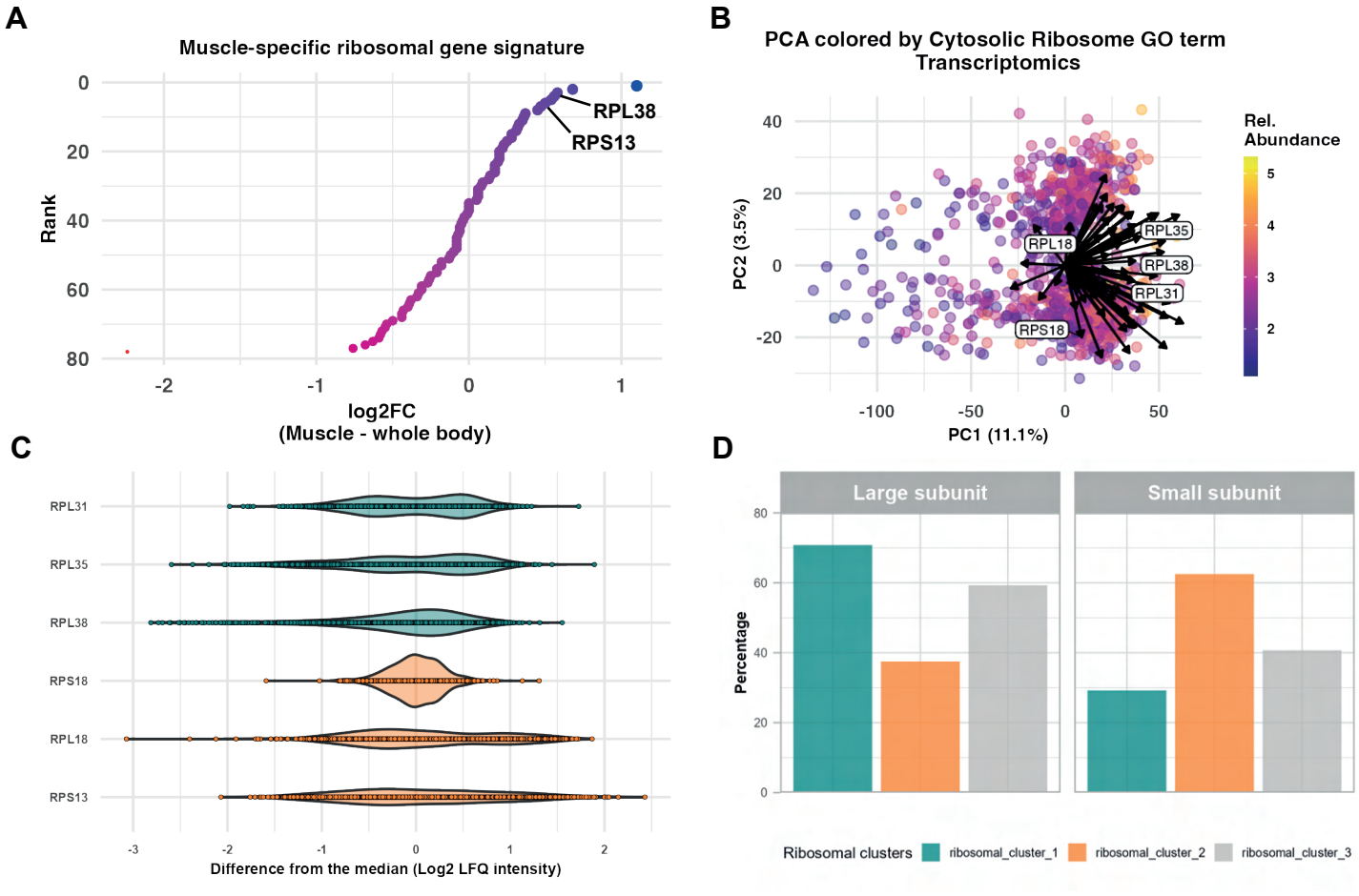
A
Muscle-specific ribosomal gene signature
Rank
log2FC
(Muscle - whole body)
RPL38
RPS13
B
PCA colored by Cytosolic Ribosome GO term
Transcriptomics
PC2 (3.5%)
PC1 (11.1%)
Rel.
Abundance
RPL18
RPL35
RPL38
RPL31
RPS18
C
RPL31
RPL35
RPL38
RPS18
RPL18
RPS13
Difference from the median (Log2 LFQ intensity)
D
Large subunit
Small subunit
Percentage
Ribosomal clusters
ribosomal_cluster_1
ribosomal_cluster_2
ribosomal_cluster_3

Figure 3 S1

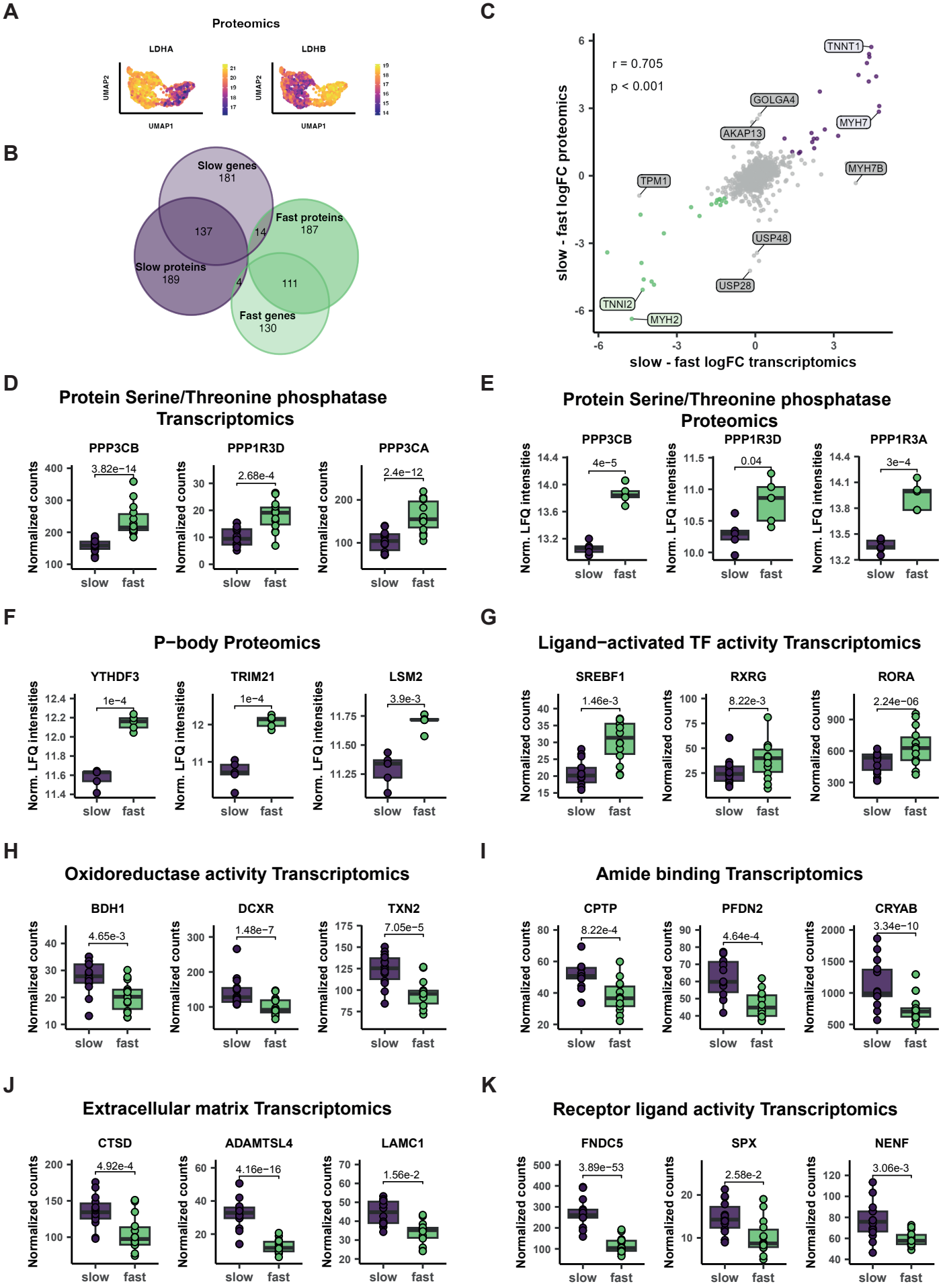
A
Proteomics
LDHA
LDHB
UMAP2
UMAP1
B
Slow genes
181
Fast proteins
187
Slow proteins
189
Fast genes
130
137
14
4
111
C
r = 0.705
p < 0.001
TNNT1
GOLGA4
MYH7
AKAP13
MYH7B
TPM1
USP48
USP28
TNNI2
MYH2
slow - fast logFC proteomics
slow - fast logFC transcriptomics
D
Protein Serine/Threonine phosphatase
Transcriptomics
PPP3CB
PPP1R3D
PPP3CA
3.82e−14
2.68e-4
2.4e−12
Normalized counts
slow
fast
E
Protein Serine/Threonine phosphatase
Proteomics
PPP3CB
PPP1R3D
PPP1R3A
4e−5
0.04
3e−4
Norm. LFQ intensities
F
P−body Proteomics
YTHDF3
TRIM21
LSM2
1e−4
1e−4
3.9e-3
G
Ligand−activated TF activity Transcriptomics
SREBF1
RXRG
RORA
1.46e-3
8.22e-3
2.24e−06
H
Oxidoreductase activity Transcriptomics
BDH1
DCXR
TXN2
4.65e-3
1.48e−7
7.05e−5
I
Amide binding Transcriptomics
CPTP
PFDN2
CRYAB
8.22e-4
4.64e-4
3.34e−10
J
Extracellular matrix Transcriptomics
CTSD
ADAMTSL4
LAMC1
4.92e-4
4.16e−16
1.56e-2
K
Receptor ligand activity Transcriptomics
FNDC5
SPX
NENF
3.89e−53
2.58e-2
3.06e-3

Figure 4 S1

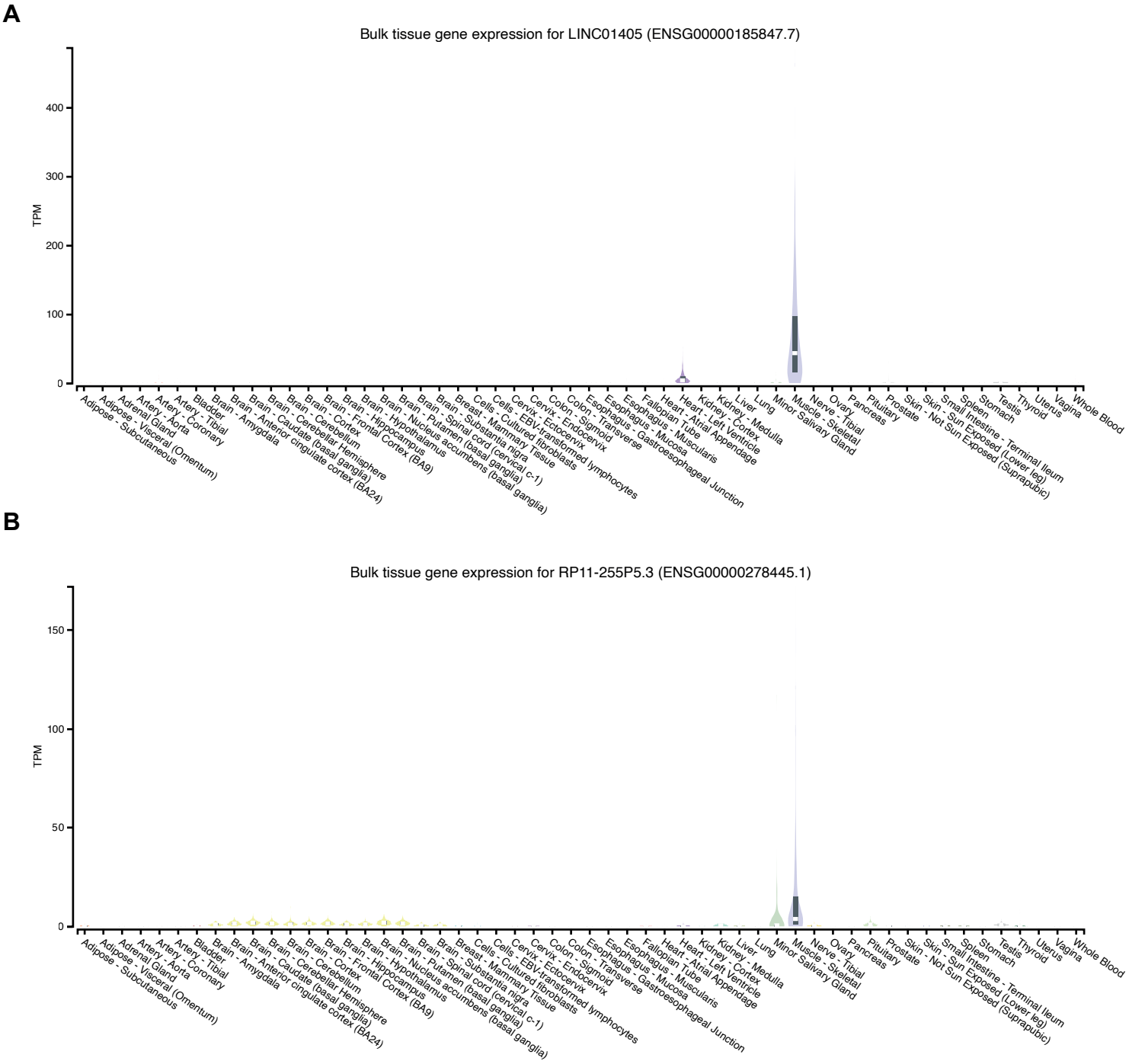
A
Bulk tissue gene expression for LINC01405 (ENSG00000185847.7)
TPM
0
100
200
300
400
Adipose - Subcutaneous
Adipose - Visceral (Omentum)
Adrenal Gland
Artery - Aorta
Artery - Coronary
Artery - Tibial
Bladder
Brain - Amygdala
Brain - Anterior cingulate cortex (BA24)
Brain - Caudate (basal ganglia)
Brain - Cerebellar Hemisphere
Brain - Cerebellum
Brain - Cortex
Brain - Frontal Cortex (BA9)
Brain - Hippocampus
Brain - Hypothalamus
Brain - Nucleus accumbens (basal ganglia)
Brain - Putamen (basal ganglia)
Brain - Spinal cord (cervical c-1)
Brain - Substantia nigra
Breast - Mammary Tissue
Cells - Cultured fibroblasts
Cells - EBV-transformed lymphocytes
Cervix - Ectocervix
Cervix - Endocervix
Colon - Sigmoid
Colon - Transverse
Esophagus - Gastroesophageal Junction
Esophagus - Mucosa
Esophagus - Muscularis
Fallopian Tube
Heart - Atrial Appendage
Heart - Left Ventricle
Kidney - Cortex
Kidney - Medulla
Liver
Lung
Minor Salivary Gland
Muscle - Skeletal
Nerve - Tibial
Ovary
Pancreas
Pituitary
Prostate
Skin - Not Sun Exposed (Suprapubic)
Skin - Sun Exposed (Lower leg)
Small Intestine - Terminal Ileum
Spleen
Stomach
Testis
Thyroid
Uterus
Vagina
Whole Blood
B
Bulk tissue gene expression for RP11-255P5.3 (ENSG00000278445.1)
TPM
0
50
100
150
C
Slow Vs Fast microproteins
RP11−296E23.1_ORF467
RP13−143G15.4_ORF796
LINC00598_ORF399
LINC01405_ORF310
−log10(P−value)
0.0
2.5
5.0
7.5
10.0
−2.5
0.0
2.5
log2FC (Slow − Fast)
D
LINC01405_ORF420:14512:14291
0.5882
LINC01405_ORF403:18859:18767
0.9774
LFQ intensities
4.3
4.4
4.5
4.6
4.7
4.8
4.9
3.7
3.8
3.9
4.0
slow
fast

Figure 5 S1

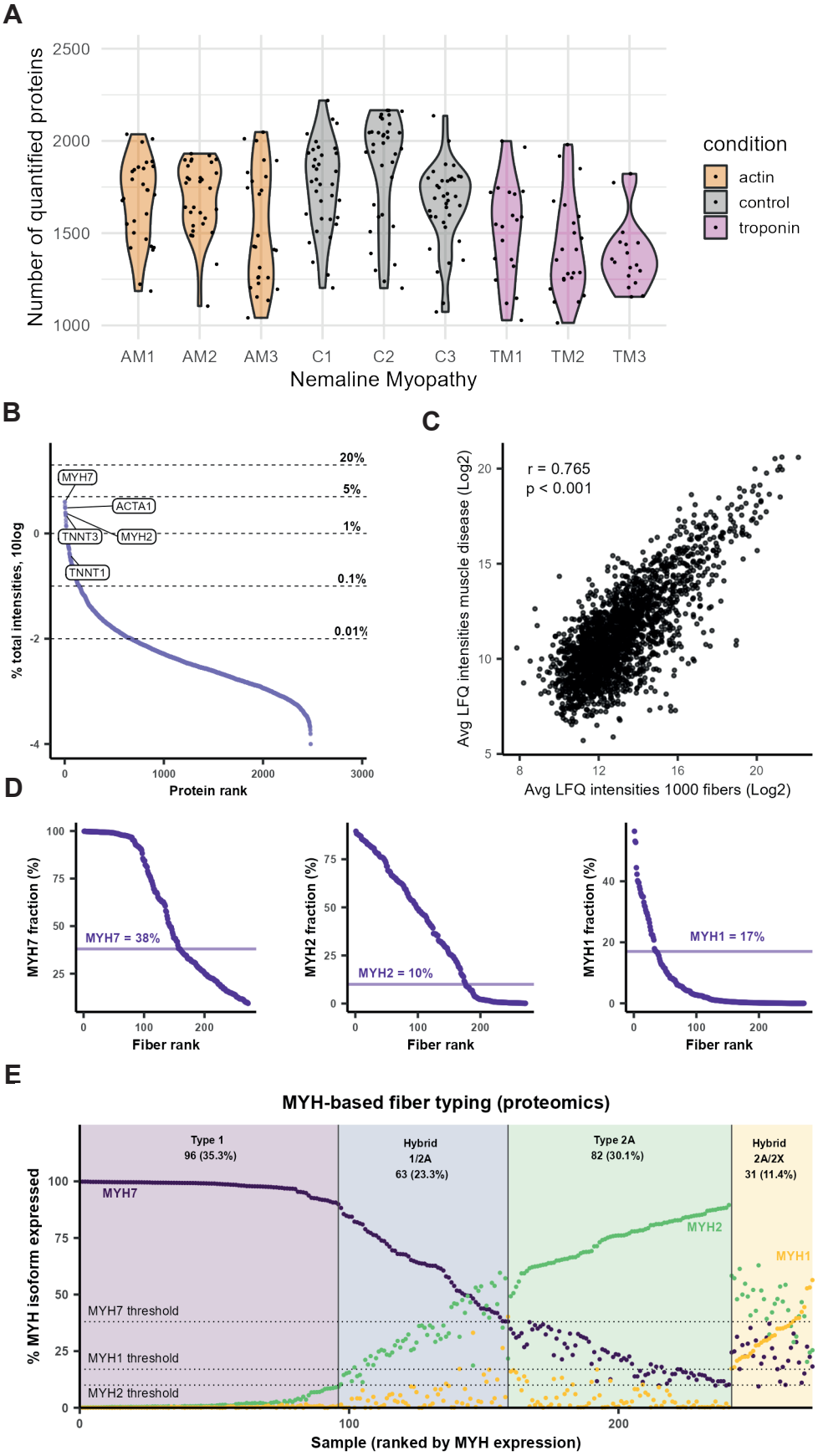
A
Number of quantified proteins
2500
2000
1500
1000
AM1
AM2
AM3
C1
C2
C3
TM1
TM2
TM3
Nemaline Myopathy
condition
actin
control
troponin
B
% total intensities, 10log
Protein rank
MYH7
ACTA1
TNNT3
MYH2
TNNT1
20%
5%
1%
0.1%
0.01%
C
Avg LFQ intensities muscle disease (Log2)
Avg LFQ intensities 1000 fibers (Log2)
r = 0.765
p < 0.001
D
MYH7 fraction (%)
MYH7 = 38%
MYH2 fraction (%)
MYH2 = 10%
MYH1 fraction (%)
MYH1 = 17%
Fiber rank
E
MYH-based fiber typing (proteomics)
% MYH isoform expressed
Type 1
96 (35.3%)
Hybrid
1/2A
63 (23.3%)
Type 2A
82 (30.1%)
Hybrid
2A/2X
31 (11.4%)
MYH7
MYH2
MYH1
MYH7 threshold
MYH1 threshold
MYH2 threshold
Sample (ranked by MYH expression)

Figure 6 S1

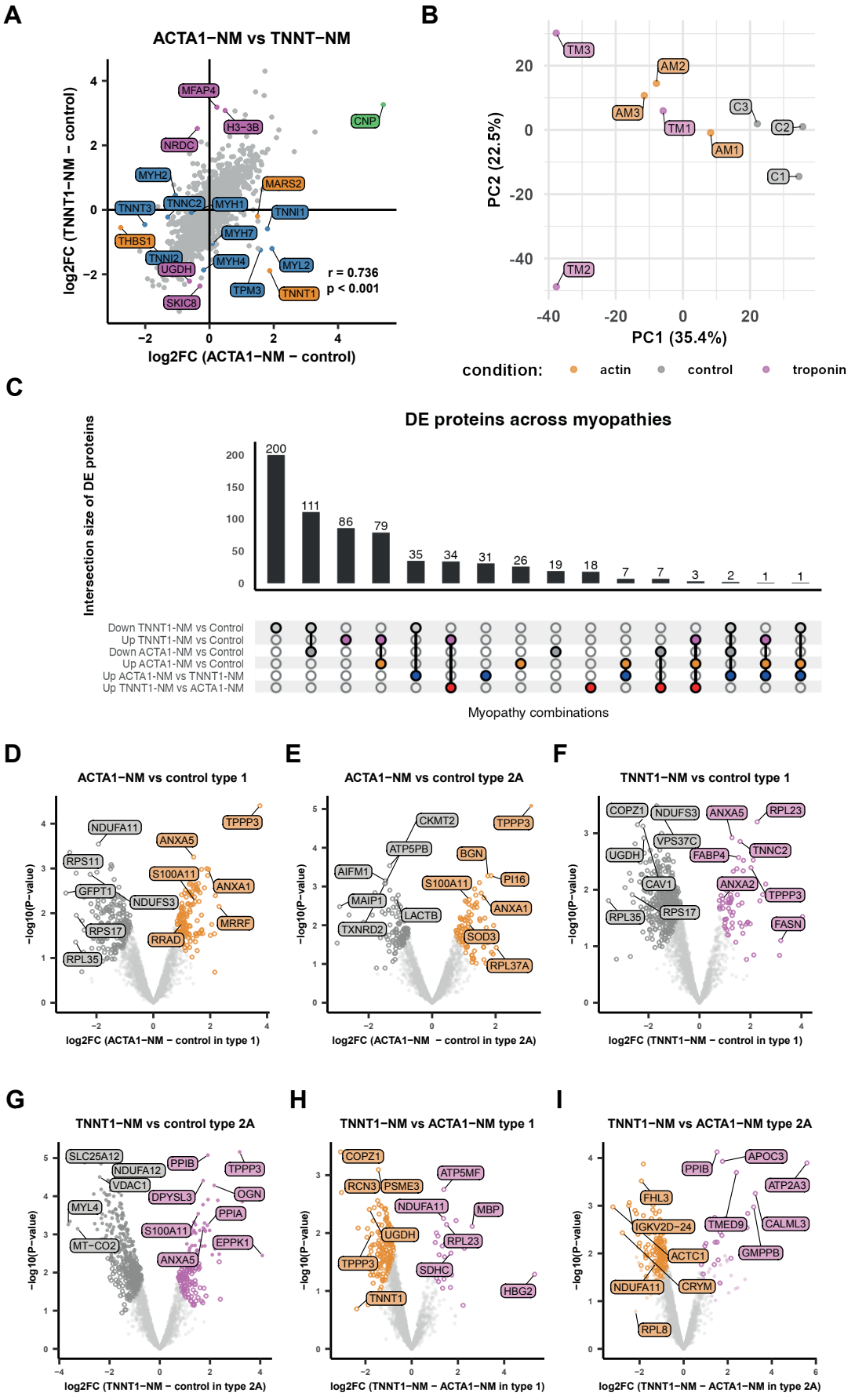
A
ACTA1−NM vs TNNT−NM
log2FC (TNNT1−NM − control)
log2FC (ACTA1−NM − control)
MFAP4
H3−3B
CNP
NRDC
MYH2
MARS2
TNNT3
TNNC2
MYH1
TNNI1
MYH7
THBS1
TNNI2
UGDH
MYH4
MYL2
TPM3
TNNT1
SKIC8
r = 0.736
p < 0.001
B
PC2 (22.5%)
PC1 (35.4%)
TM3
AM2
AM3
TM1
C3
C2
AM1
C1
TM2
condition:
actin
control
troponin
C
DE proteins across myopathies
Intersection size of DE proteins
200
111
86
79
35
34
31
26
19
18
7
7
3
2
1
1
Down TNNT1-NM vs Control
Up TNNT1-NM vs Control
Down ACTA1-NM vs Control
Up ACTA1-NM vs Control
Up ACTA1-NM vs TNNT1-NM
Up TNNT1-NM vs ACTA1-NM
Myopathy combinations
D
ACTA1−NM vs control type 1
−log10(P−value)
log2FC (ACTA1−NM − control in type 1)
NDUFA11
TPPP3
ANXA5
RPS11
S100A11
ANXA1
GFPT1
NDUFS3
MRRF
RPS17
RRAD
RPL35
E
ACTA1−NM vs control type 2A
log2FC (ACTA1−NM − control in type 2A)
CKMT2
TPPP3
ATP5PB
BGN
AIFM1
S100A11
PI16
MAIP1
ANXA1
LACTB
TXNRD2
SOD3
RPL37A
F
TNNT1−NM vs control type 1
log2FC (TNNT1−NM − control in type 1)
COPZ1
NDUFS3
ANXA5
RPL23
VPS37C
UGDH
FABP4
TNNC2
CAV1
ANXA2
TPPP3
RPL35
RPS17
FASN
G
TNNT1−NM vs control type 2A
log2FC (TNNT1−NM − control in type 2A)
SLC25A12
PPIB
NDUFA12
TPPP3
VDAC1
OGN
DPYSL3
MYL4
PPIA
S100A11
MT−CO2
EPPK1
ANXA5
H
TNNT1−NM vs ACTA1−NM type 1
log2FC (TNNT1−NM − ACTA1−NM in type 1)
COPZ1
ATP5MF
RCN3
PSME3
NDUFA11
MBP
UGDH
RPL23
TPPP3
SDHC
HBG2
TNNT1
I
TNNT1−NM vs ACTA1−NM type 2A
log2FC (TNNT1−NM − ACTA1−NM in type 2A)
APOC3
PPIB
ATP2A3
FHL3
IGKV2D−24
TMED9
CALML3
ACTC1
GMPPB
NDUFA11
CRYM
RPL8

Figure 6 S2

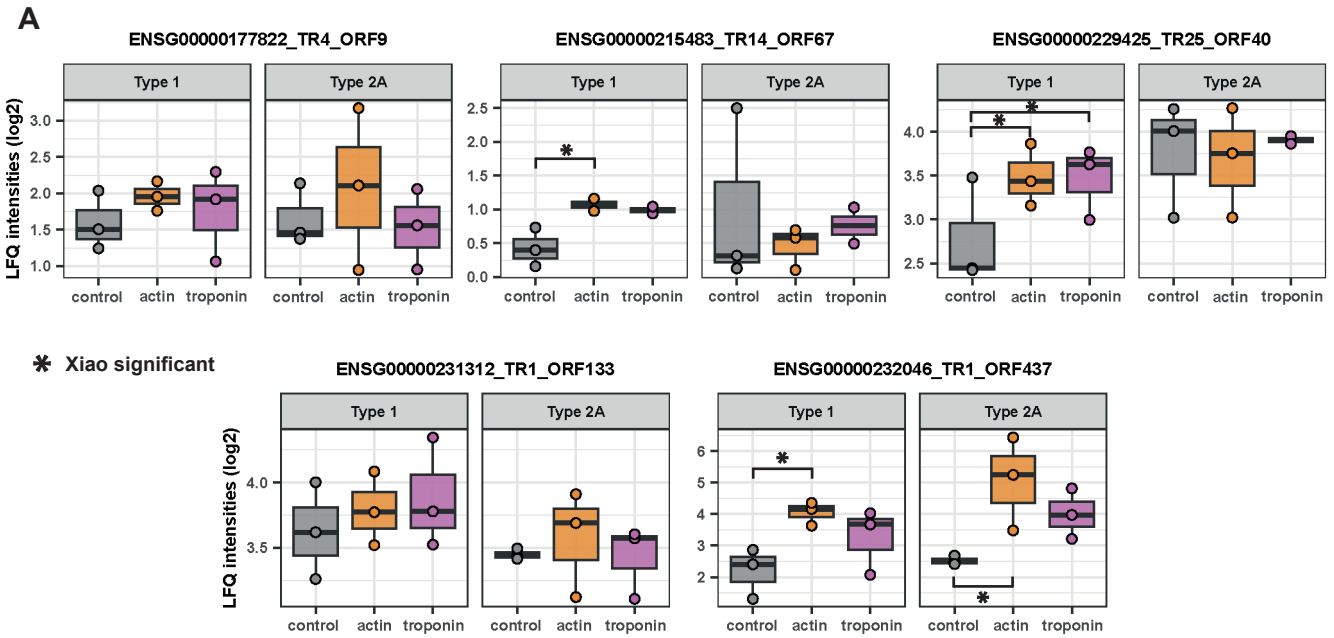
A
ENSG00000177822_TR4_ORF9
ENSG00000215483_TR14_ORF67
ENSG00000229425_TR25_ORF40
Type 1
Type 2A
LFQ intensities (log2)
control
actin
troponin
✱ Xiao significant
ENSG00000231312_TR1_ORF133
ENSG00000232046_TR1_ORF437

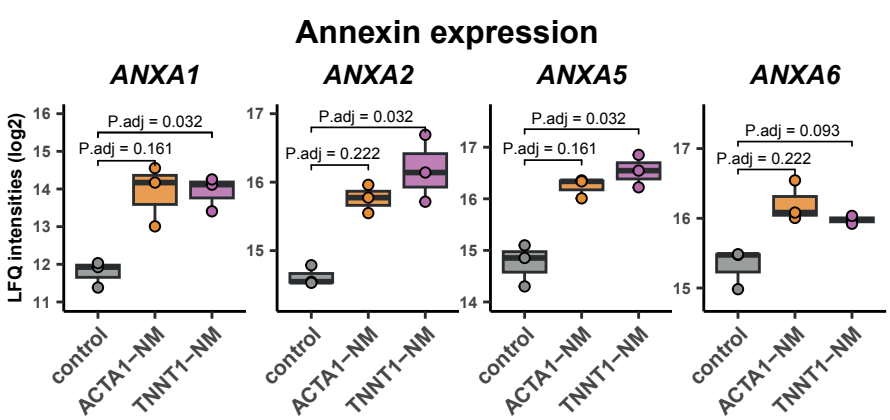
B
Annexin expression
ANXA1
ANXA2
ANXA5
ANXA6
LFQ intensities (log2)
P.adj = 0.032
P.adj = 0.161
P.adj = 0.032
P.adj = 0.222
P.adj = 0.032
P.adj = 0.161
P.adj = 0.093
P.adj = 0.222
control
ACTA1-NM
TNNT1-NM

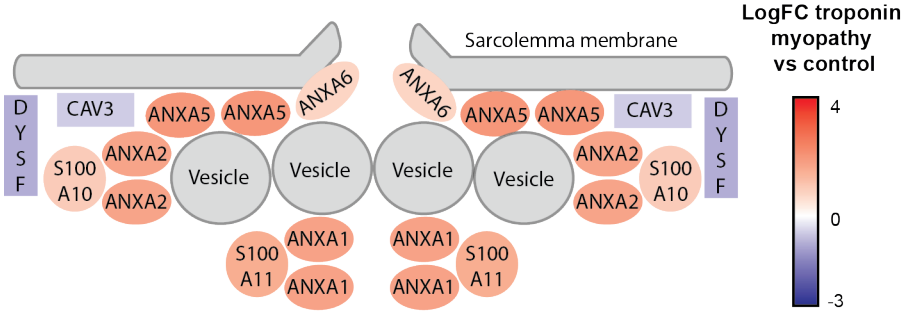
C
Sarcolemma repair machinery
Sarcolemma membrane
LogFC troponin myopathy vs control
DYSF
CAV3
ANXA5
ANXA6
ANXA2
S100 A10
Vesicle
ANXA1
S100 A11
4
0
-3

Figure 6 S3

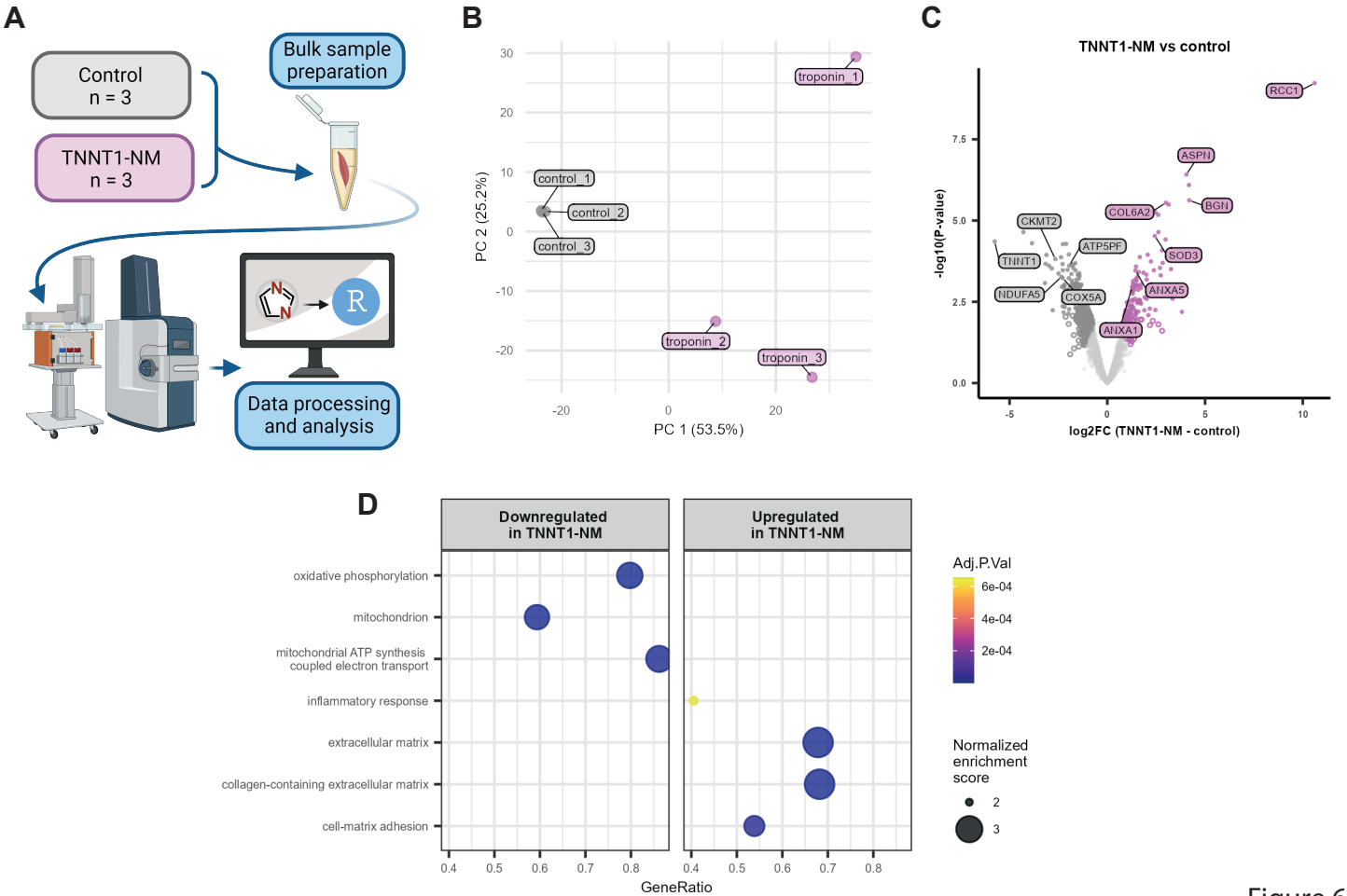
A
Control
n = 3
TNNT1-NM
n = 3
Bulk sample
preparation
Data processing
and analysis
B
troponin_1
control_1
control_2
control_3
troponin_2
troponin_3
PC 2 (25.2%)
PC 1 (53.5%)
C
TNNT1-NM vs control
RCC1
ASPN
BGN
COL6A2
CKMT2
ATP5PF
SOD3
TNNT1
NDUFA5
COX5A
ANXA5
ANXA1
-log10(P-value)
log2FC (TNNT1-NM - control)
D
Downregulated
in TNNT1-NM
Upregulated
in TNNT1-NM
oxidative phosphorylation
mitochondrion
mitochondrial ATP synthesis
coupled electron transport
inflammatory response
extracellular matrix
collagen-containing extracellular matrix
cell-matrix adhesion
GeneRatio
Adj.P.Val
6e-04
4e-04
2e-04
Normalized
enrichment
score
2
3

Figure 6 S4